

ENGINEERED LIVING MATERIAL BASED ON PROTEIN-MEDIATED
BACTERIAL ASSEMBLY

Thesis by

Hanwei Liu

In Partial Fulfillment of the Requirements for
the Degree of
Doctor of Philosophy

The logo for the California Institute of Technology (Caltech), featuring the word "Caltech" in a bold, orange, sans-serif font.

CALIFORNIA INSTITUTE OF TECHNOLOGY

Pasadena, California

2024

(Defended Aug 25th, 2023)

©2024

Hanwei Liu

ORCID: 0000-0002-4667-1673

All Rights Reserved

ACKNOWLEDGEMENTS

First, I would like to thank my advisor, Dr. David Tirrell, for kindly introducing me into the research group, offering advice, and guiding me to accomplish a project that I originally considered almost impossible to do. His leadership, scientific rigor, and senses of humor inspired me to become both a better scientist and a person. I would also like to thank my thesis committee, Dr. Mark Davis, Dr. Julia Kornfield, and Dr. Maxwell Robb for pointing out my weaknesses and helping me to improve my skills in scientific thinking, presentation, and writing.

I would like to thank my chief collaborator, Dr. Priya Chittur, for developing fantastic material characterization devices and methods. Without her help, the mechanical properties of bacterial films presented in this thesis could not be achieved.

I would like to thank my chief collaborator, Dr. Chenxi Qian, for introducing the stimulated Raman scatter techniques. I still remember the thrill of seeing *in situ* visualization of biomineralization. Congratulations on becoming a father.

I would also like to thank principal investigators, Dr. Lu Wei, Dr. Mikhail Shapiro, Dr. Rustem Ismagilov, and Dr. G. Ravichandran, for offering collaboration opportunities and instruments for data acquisition.

Staff members of multiple Caltech facilities, including BIF, BILRC, CCE mass spectrometry facility, GPS Analytical facility, KNI and MMRC trained me and helped me acquire valuable data. I am truly grateful to them.

I would like to thank all current members and alumni of Tirrell research group for teaching me new techniques and giving me advice and suggestions. I would also like to thank Irina for helping us organizing meetings and keep our group running efficiently.

I acknowledge the whole Caltech community's effort to build an open and inclusive

environment that promotes collaborative research on campus.

I am grateful to my family for raising me up and supporting me to pursue bachelor and doctorate degrees abroad. I am especially thankful to my mother for encouraging me to observe natural phenomena and my cousin for revealing the joy of reading to me. I am also grateful to all the great teachers I have encountered since childhood for initiating my interest in science and encouraging me to do research myself. I also built a solid background in chemistry thanks to my undergraduate institution, UC Berkeley.

I am also honored to have Caltech Graduate Council (GSC) choose two of my photographs to be displayed at the Caltech dining hall and Red Door Café. One of the photographs was of two dolphins jumping out of the ocean. Thanks to the well-established whale-watching tour business in the LA area, I've already sighted three kinds of dolphins and six kinds of baleen whales. Though I did not have chance to see my favorite giant pandas during graduate school, I was lucky enough to observe these cute and intelligent sea creatures. I wish to expand my whale-watching list in the future. I would like to thank Caltech library's Tech-hub for providing 3D-printing workshops and offering free 3D-printing services. The facemask holders I printed using the library's 3D-printers did save my ears and prevent me from COVID infection during the pandemic. I wish everyone safety and health in the coming years.

In the end, I would like to thank two great philosophers who wrote books that supported me throughout this Ph.D. journey, Zhuang Zhou and Mao Zedong.

ABSTRACT

Engineered Living Materials(ELMs) is a newly emerging field of biotechnology at the interface of synthetic biology and traditional material science. Over the past few years, several kinds of novel ELMs were developed. These materials, derived from organisms including bacteria, fungi and plants, have potential applications in therapeutics, electronics, constructions and environmental remediation. We invented an novel method that enables bacteria to form cohesive thin films through cell surface display of associative proteins. In this thesis, we will first demonstrate that we can genetically encode the mechanical properties of living bacterial films by controlling amino acid sequences of artificial proteins displayed at cell surface. Later, we will show that we can generate bacterial-matrix composite by displaying enzymes and peptides at the cell surface.

In Chapter 1, we review the development of ELMs and existing examples of ELMs. The fundamental definition of ELMs and trends in ELMs development will be presented. Bacterial based ELMs, created either by encapsulating bacteria of interests into a synthetic polymeric matrix or by boosting the natural biosynthetic pathways of biopolymers and mineralization in bacteria will be the major part of discussion. The goal of this chapter is to provide context and background of ELMs research.

In Chapter 2, we discuss the design and preparation method of our own ELM. The process of how we come up with growing bacterial films on perforated polycarbonate membranes and development of suction coating method will be presented. By using model SpyTag-SpyCatcher bacterial assembly system, we unraveled the principles behind making cohesive bacterial films from a single bacterial colony.

In Chapter 3, we discuss controlling bacterial films' mechanical properties through genetic manipulation. Engineered bacteria displaying artificial unstructured Elastin-like-peptides (ELPs) at cell surface can form cohesive, soft and yielding films with tens of kPa value of Young's moduli. By merely adding a cysteine at the N-terminal part of the ELP, the engineered bacteria can form relative tough, non-yielding films with 3 times higher Young's moduli due to formation of intercellular covalent disulfide bond. Apart from having enhanced mechanical strength, such films containing covalent intercellular interactions have abilities to self-heal within 24 hours after being cut into halves.

In chapter 4, we discuss a strategy based on stimulated Raman scattering microscopy to monitor phosphatase-catalyzed mineralization of engineered living bacterial films *in situ*. Real-time label-free imaging elucidates the mineralization process, quantifies both the organic and inorganic components of the material as functions of time, and reveals spatial heterogeneity at multiple scales. In addition, we correlate the mechanical performance of films with the extent of mineralization.

In chapter 5, we discuss the ability of bacterial protein surface display system to catalyze artificial extracellular matrix formation. We demonstrated that heme-containing peroxidase Apex2 can be fused with autotransporter protein previous described in Chapter 2, 3 and 4, successfully displayed at cell surface and remain functional at catalyzing formation of polymer polyaniline (PANI) in the presence of hydrogen peroxide and aniline monomers at physiological pH. Similarly, by displaying multiple kinds peptide known to mediate silica deposition, we can coat bacteria with silica of different morphologies without reducing the viabilities of bacteria.

In Chapter 6, we discuss the future directions of engineered living materials developed in previous chapters. We propose methods to further improve the mechanical strength of bacterial films, to find “sweet-spot” of biomineralization, and to develop artificial hydrophobin.

PUBLISHED CONTENTS AND CONTRIBUTIONS

Chapter 3 is derived from a manuscript in preparation:

H. Liu*, P. K. Chittur*, J. A. Kornfield and D. A. Tirrell, Cohesive Living Bacterial Films with Tunable Mechanical Properties from Cell Surface Protein Display. In preparation.

*Co-first authors

Chapter 4 is derived from a manuscript already submitted to a journal:

C. Qian*, H. Liu*, P. K. Chittur, R. S. Chadha, Y. Yao, J. A. Kornfield, L. Wei and D. A. Tirrell, Quantitative Real-Time Analysis of Living Materials by Stimulated Raman Scattering Microscopy. Submitted.

*Co-first authors

TABLE OF CONTENTS

Acknowledgements.....	iii
Abstract.....	v
Published Contents and Contributions.....	viii
Table of Contents	ix
List of Figures and Tables.....	xiii
Chapter 1: Introduction to Engineered Living Materials.....	1
Abstract.....	1
Introduction.....	2
Engineered living material: the real treasure bowl.....	2
Synthetic polymer & microorganism composite	4
Secreted biopolymer & microorganism composite	6
Biomaterial & microorganism composite.....	8
Living particle assemblies	9
Conclusion.....	10
Reference	11
Chapter 2: Growing Cohesive Bacterial films on Perforated Scaffolds	17
Abstract.....	17
Introduction.....	19
Results and Discussions	20
Finding suitable materials and methods for growing living bacterial films.....	20
Suction coating to form cohesive bacterial films using SpyTag-SpyCatcher chemistry....	23
Surface-display of elastin-like-peptide contributes to bacterial film cohesiveness.....	27

Using a double plasmid system to generate cohesive films with SpyTag-SpyCatcher	
covalent crosslinks.....	30
Conclusion	32
Materials and Methods	33
Acknowledgements and Contributions.....	35
Supporting Information	35
Reference	44

Chapter 3: Cohesive Living Bacterial Films with Tunable Mechanical Properties from Cell Surface Protein Display.....	47
Abstract.....	47
Introduction.....	48
Results and Discussions.....	50
Design of surface displayed protein and growing of bacterial films	50
Measuring mechanical properties of bacterial films using ramp bulge tests.....	54
Disulfide bonds play an essential role in enhancing the moduli of CE6-AT films	56
Viscoelastic behavior of bacterial films revealed by oscillatory bulge test.....	60
CE6-AT films can heal within a day	62
Conclusion	67
Materials and Methods	68
Acknowledgements and Contributions.....	76
Supporting Information	77
Reference	96

Chapter 4: Quantitative Real-Time Analysis of Living Materials by Stimulated Raman Scattering Microscopy	102
Abstract.....	102
Introduction.....	103
Results and Discussions.....	105
Analysis of alkaline phosphatase (PhoA)-catalyzed calcium phosphate formation by in situ SRS imaging.....	105
Raman characterization and SRS imaging of E. coli mineralization.....	107
Real-time SRS imaging of mineralization in bacterial films.....	110
Morphology of mineralized biofilms.....	112
Correlating biofilm mechanical properties with phosphate levels quantified by SRS.....	116
Conclusion.....	119
Materials and Methods.....	120
Acknowledgements.....	126
Supporting Information.....	127
Reference.....	144
Chapter 5: Matrix Production by Bacterial Enzymes and Peptide Surface Display	149
Abstract.....	149
Introduction.....	150
Results and Discussions.....	152
Surface displayed Apex2 enzyme can catalyze oxidative formation of polyaniline.....	152
Surface displayed peptide can control morphology of deposited silica and silica deposition does not affect viability of the film.....	154
Conclusion.....	156
Materials and Methods.....	157

	xii
Acknowledgements	157
Supporting Information	158
Reference	165
Chapter 6: Future Directions.....	170
Abstract	170
Future Directions	171
Improving mechanical properties of bacterial films	171
Finding the “sweet-spot” for bacterial mineralization.....	177
Developing artificial hydrophobin	179
Reference	182

LIST OF FIGURES AND TABLES

Figure 1.1.....	4
Figure 1.2.....	4
Figure 1.3.....	6
Figure 1.4.....	8
Figure 1.5.....	9
Figure 2.1.....	20
Figure 2.2.....	22
Figure 2.3.....	22
Figure 2.5.....	27
Figure 2.6.....	30
Figure 2.7.....	32
Table S2.1.....	37
Table S2.2.....	39
Figure S2.1.....	42
Figure S2.2.....	43
Figure S2.3.....	43
Figure 3.1.....	53
Figure 3.2.....	56
Figure 3.3.....	59
Figure 3.4.....	62
Figure 3.5.....	66
Table S3.1.....	79
Table S3.2.....	80
Figure S3.1.....	80

Figure S3.2.....	81
Figure S3.3.....	81
Figure S3.4.....	82
Figure S3.5.....	82
Figure S3.6.....	83
Figure S3.7.....	83
Figure S3.8.....	84
Figure S3.9.....	85
Figure S3.10.....	85
Figure S3.11.....	85
Figure S3.12.....	86
Figure S3.13.....	88
Figure S3.14.....	89
Figure S3.15.....	89
Figure S3.16.....	90
Figure S3.17.....	90
Figure S3.18.....	91
Figure S3.19.....	91
Figure S3.20.....	92
Table S3.3.....	92
Figure S3.21.....	93
Figure S3.22.....	93
Figure S3.23.....	94
Figure S3.24.....	94
Figure S3.25.....	95
Figure 4.1.....	107

Figure 4.2.....	110
Figure 4.3.....	112
Figure 4.4.....	115
Figure 4.5.....	118
Table S4.1	129
Table S4.2.....	130
Figure S4.1.....	131
Figure S4.2.....	132
Figure S4.3.....	133
Figure S4.4.....	134
Figure S4.5.....	135
Figure S4.6.....	136
Figure S4.7.....	137
Figure S4.8.....	138
Table S4.3.....	139
Figure S4.9.....	140
Figure S4.10.....	143
Figure 5.1.....	150
Figure 5.2.....	154
Figure 5.3.....	156
Table S5.1	160
Table S5.2.....	161
Figure S5.1.....	163
Table S5.3.....	163
Figure S5.2.....	164
Table S5.4.....	164

Figure 6.1..... 172

Figure 6.2..... 175

Figure 6.3..... 179

Chapter 1

Introduction to Engineered Living Materials

1. Abstract

Engineered living materials is an emerging field that sits at the border of synthetic biology and materials science and engineering. These materials, which contain living components, possess attributes of living systems including autonomous behavior, environmental adaptiveness, self-healing capability and genetic programmability. In the past decade, several kinds of engineered living materials made from genetically modified microorganisms were reported and multiple manufacturing strategies of engineered living materials were proposed. In this chapter, I will provide a brief overview of existing systems of engineered living materials. I will divide them into four major kinds.

- (1) Synthetic polymer & microorganism composites
- (2) Secreted biopolymer & microorganism composites
- (3) Biomineral & microorganism composites
- (4) Living particle assemblies

I will also discuss how these strategies of building living materials are related to our protein-mediated bacterial assembly-based engineered living materials.

2. Introduction

2.1 Engineered living material: the real treasure bowl

Growing up in Nanjing, China, the ancient capital city with the longest (22 miles) city wall in the whole world, I've heard many mysterious stories about this 600 year old city wall since childhood. The most fascinating story I can still remember was called the "treasure bowl". According to this folklore, the city wall of Nanjing was made resilient to earthquakes, typhoons and even wars not because of ingenious designs by architects, nor the hard labor done by the workers, but a "treasure bowl" that was buried at the very bottom of the largest city gate "Treasure Gate" (now called "China Gate"). At the time when the Ming Empire was founded at Nanjing, the emperor Hongwu encountered a problem that he didn't have enough labor and money to build the city wall. He heard that the richest people in China had a "treasure bowl" that can copy anything thrown into it and produce an extra copy. The emperor forced the rich merchant to give him the "treasure bowl" and buried it underneath the city gate and the city wall built itself overnight and can self-repair whenever destruction happens.

For sure, this folklore only reflects part of real history and that rich merchant was truly banished by the emperor in the end. If you do believe this folklore, then the city wall is no longer just a dull historic relic but a living structure made of materials that have infinite healing capacity. The very first kind of "Engineered Living Materials".

Since the beginning of civilization, people started to use materials derived from living systems. For example, wood is derived from living trees. Wood will deteriorate over the time. For a tree, however, as long as it is alive, new branches made of new wood will grow and scars caused by weather or animals can be healed. Due to the lack of

understanding about principles that govern life, for a long time human civilization has been limited to manufacturing materials with physical and chemical methods or using materials derived from living systems without the capability to engineer desired properties at the biological level.

Since last century, the discovery of the central dogma¹ of molecular biology and inventions of multiple gene editing tools²⁻⁵ made engineering and programming properties of biological materials at the genetic level plausible. Genetic engineering of biofilms^{6,7} is especially alluring because bacteria are easier to engineer and raise less ethical issues⁸ compared to complex multicellular eukaryotic systems. Biofilms⁹ are composed of living bacterial cells and extracellular polymeric matrix (EPS).^{10,11} In such composites, bacterial cells can sense environmental stress¹² and turn on different metabolic pathways¹³⁻¹⁵ to survive. The bacterial biofilm can automatically form and dissociate when environmental conditions change.^{16,17} The EPS can act as a protective layer¹⁸, help bacteria to anchor to surfaces¹⁹ and even assist bacterial communication.²⁰ If a defect is created in a biofilm, the bacterial film can self-heal either through reproduction or through matrix secretion to fill the defect with cells or polymeric matrix. The autonomous, adaptive and self-healing attributes of biofilms are listed in **Fig 1.1**.

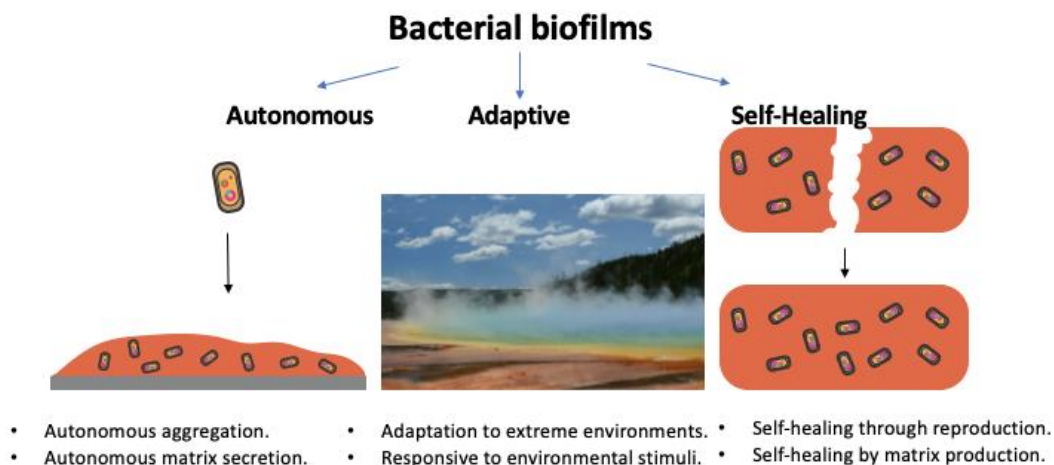


Figure 1.1 Autonomous, adaptive and self-healing properties of biofilms.

It is worthwhile to note at the end of this section that most human architecture will be gone over the time, but bacteria will always generate new biofilms. It seems that these biofilms are the real “treasure bowl” as they can regenerate forever. I believe through engineering biofilms into controllable living materials, we will get our own “treasure bowl” sometime in the future.

2.2 Synthetic polymer & microorganism composite

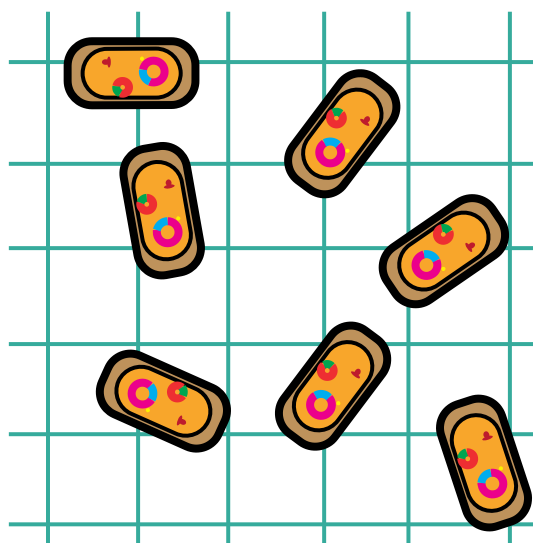


Figure 1.2 Schematic of bacteria encapsulated in synthetic polymer matrix.

In this approach, the bacteria act as the living component of the material and the synthetic polymer acts as the matrix that protects bacteria from environmental stress but allows nutrition and moisture to have access to the bacterium. One concern about this method is that the synthetic polymer used might not be from sustainable resources. To become more sustainable, polymers that are biocompatible, coming from renewable resources and recyclable are receiving attention.²¹ Another concern is that the synthetic polymeric matrix will deteriorate over the time and bacteria encapsulated are unable to heal it. One approach to address this concern is that the material is originally cast using synthetic polymer or biologically derived polymers, later, the bacteria can secrete their own polymer matrix such that the old scaffold is replaced by bacterial polymers.²² This approach is especially useful in the case of probiotic delivery,^{21,23,23} as probiotics are sensitive and require function at specific locations. Encapsulation of resilient *B subtilis* spores was also reported.^{24,25} *B subtilis* spores can survive extreme environments and rejuvenate when environmental conditions improve²⁶. By trapping engineered *B subtilis* spores in a matrix, *B subtilis* can convert to functional (vegetative) cell form when needed, carrying out useful catalytic functions for several cycles without danger of leaking genetically modified bacteria into the environment.

2.3 Secreted biopolymer & microorganism composite

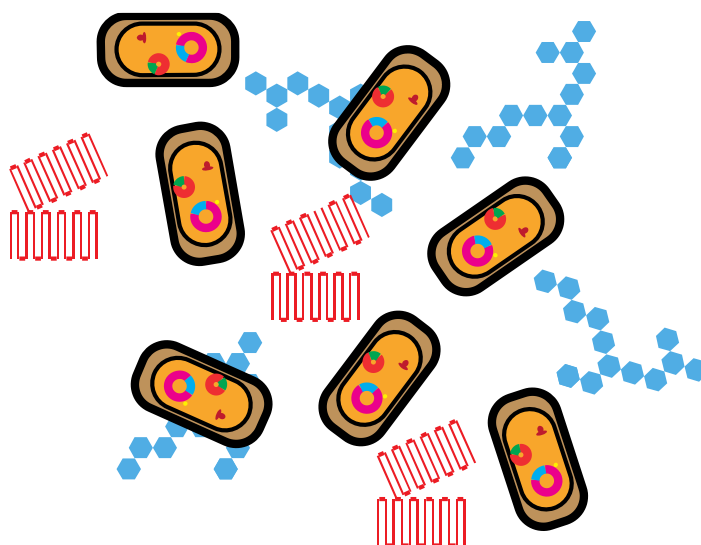


Figure 1.3 Schematic of bacteria with secreted polymeric matrix surrounding them.

In this approach, the bacterium is encapsulated by polymers it secretes and material properties are determined mainly by these secreted polymers. Since biopolymers are genetically encoded and regulated, genetic programmability of these secreted biopolymers is possible.

Two classes of secreted biopolymers have been investigated extensively as model engineered living materials. One is curli fibril, which is an amyloid like protein fiber.²⁷ Another is bacterial cellulose, which is a polysaccharide fiber.²⁸ Curli fibril proteins can be engineered directly through genetic manipulation and several curli fibril based materials were demonstrated to have potential applications in bioelectronics²⁹, environmental remediation³⁰ and therapeutics.^{31,32} Other than *E. coli*, *B. subtilis*³³ and many other bacterial species have the capability to synthesize curli fibrils.

Compared to curli fibril, bacterial cellulose as a polysaccharide can't be directly genetically modified and gene manipulation at the level of metabolic pathways is

required. On the other hand, bacterial cellulose has better mechanical properties^{28,34} compared to plant cellulose, making it a good candidate for fabrics³⁵. Bacterial cellulose can be produced at a massive scale. For example, nata de coco is bacterial cellulose pellicles from fermented coconut juice. In Vietnam, annual production of nata de coco is estimated to be around 15,000 tons per year,³⁶ a value curli fibrils cannot reach so far. Furthermore, bacterial cellulose expressing bacteria are commonly used in the food industry³⁶⁻³⁸ and generally considered safe. For example, pellicles in Kombucha are made of bacterial cellulose pellicles produced acetobacter.³⁹

2.4 Biomineral & microorganism composite

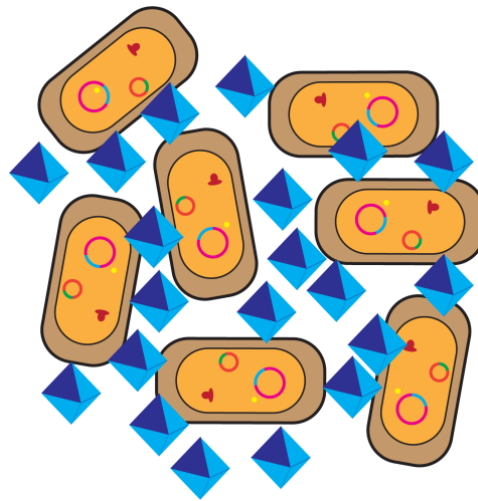


Figure 1.4 Schematic of biomineral microorganism composite.

Biomineralization⁴⁰ is a commonly used strategy to enhance mechanical strength of soft biological materials. In the case of bacterial based living materials, three major strategies can be achieved efficient biomineralization.

First, some bacteria are known to have biomineralization capability. Cyanobacteria, apart from capable of doing photosynthesis, can increase carbonate concentration in the environment forcing calcium carbonate precipitation.⁴¹ Researchers at Colorado State University successfully utilized cyanobacteria's biomineralization ability to produce engineered living building materials.⁴²

Secondly, model organisms like *E. coli* can be engineered to express recombinant enzymes that can catalyze biomineralization. Two commonly used enzymes are urease^{43,44} and carbonic anhydrase^{45,46}. Urease converts urea into ammonia and carbon dioxide, effectively increases the carbonate concentration, and causes calcium carbonate precipitation. Carbonic anhydrase can capture and convert carbon dioxide in

the environment into bicarbonate, causing calcium carbonate precipitation. Enzyme catalyzed mineralization is fast, and can be completed within a few hours.⁴⁴

The last strategy uses proteins that are known to mediate nucleation of minerals. A paper published by Wang et al.⁴⁷ serves as an example. The authors grew a living material based on engineered curli fibrils. By fusing a peptide that can mediate nucleation of calcium phosphate to curli fibrils, the curli fibrils can mediate hydroxyapatite biomineralization. The drawback of this approach is that it takes several days to achieve full mineralization.

2.5 Living particle assemblies

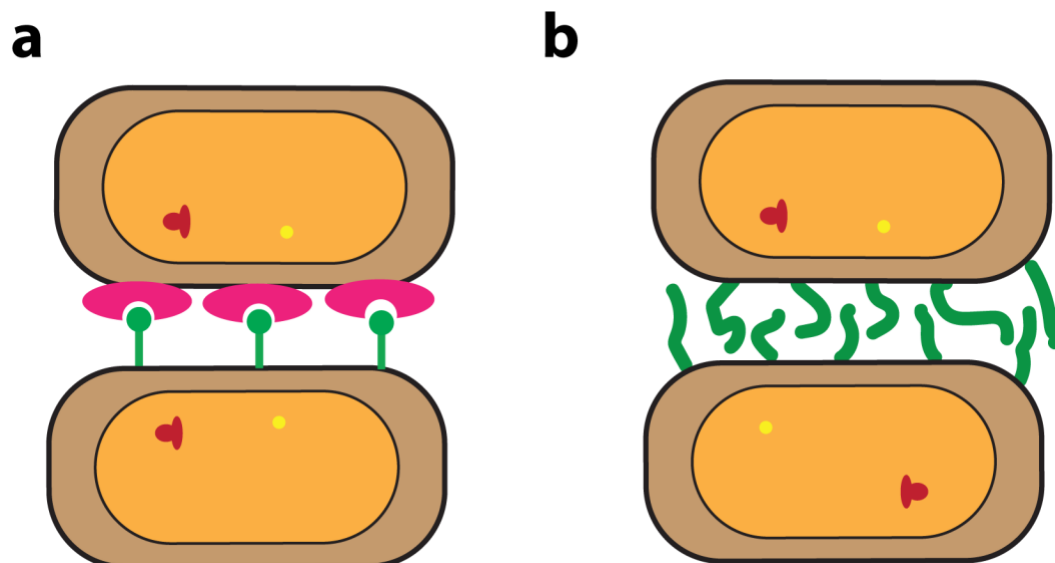


Figure 1.5 Schematic of strategies for living particle assembly. **a.** Antigen-nanobody interaction. Antibodies in magenta color are displayed on the surface of cell on the top while antigens in green are displayed on the surface of cell at bottom. **b.** High density expression of unstructured proteins. Unstructured peptide in green color are displayed on the cell surface and causing adhesion between cells.

In some natural biofilms, instead of secreting matrix, bacteria aggregate by expressing adhesins^{48,49} at the cell surface. Adhesins are proteins displayed at cell surface, facilitating bacteria adhesion to surface and other cells, playing important roles in biofilm formation⁵⁰ and infection⁵¹. These surface-display systems⁵² have been studied

extensively and engineered to express recombinant proteins at cell surfaces, including enzymes⁵³ and epitopes for vaccines.⁵⁴ Some groups were able to display antigen and antibody pairs at the cell surface to achieve cell specific aggregation.⁵⁵ Using these antigen-nanobody pairs, a class of matrix-free living materials⁵⁶ that can be 3D printed was created, in which antigen-displaying *E. coli* and nanobody-expressing *E. coli* cells were harvested from liquid culture and then mixed together. Another approach used *C. crescentus*,⁵⁷ in which unstructured elastin-like-peptides were displayed at a high density of 14,000 proteins per μm^2 .⁵⁸ This high density of surface display caused cell aggregation and material of cm length scale was generated in liquid culture. Bacterial aggregates in planktonic culture was collected and packed into a syringe and later extruded out of the syringe and casted into different shapes. Rheological measurement showed that these *C. crescentus* aggregates are soft material with storage moduli at orders of magnitude around 10 kPa.

3. Conclusion

In this chapter, the notion of “Engineered Living Materials” (ELMs) was introduced and existing examples of ELMs and their manufacture methods were discussed briefly. From these examples we found that current ELMs still has several drawbacks, including usage of synthetic polymers, limitations of secretion systems, relative long growth time and consumption of large amount of liquid media. These disadvantages encouraged us to develop a novel living material based on protein-mediated bacterial assembly that is autonomously formed without help of synthetic polymers and has its properties and functions encoded genetically. Details about this kind of living materials will be discussed in the following chapters.

4.Reference

1. Nirenberg: Glossary.
<https://web.archive.org/web/20150317004800/http://history.nih.gov/exhibits/nirenberg/glossary.htm> (2015).
2. Khan, S. *et al.* Role of Recombinant DNA Technology to Improve Life. *Int. J. Genomics* **2016**, 2405954 (2016).
3. Recombinant DNA Technology - an overview | ScienceDirect Topics.
<https://www.sciencedirect.com/topics/biochemistry-genetics-and-molecular-biology/recombinant-dna-technology>.
4. Becker, S. & Boch, J. TALE and TALEN genome editing technologies. *Gene Genome Ed.* **2**, 100007 (2021).
5. Jinek, M. *et al.* A programmable dual-RNA-guided DNA endonuclease in adaptive bacterial immunity. *Science* **337**, 816–821 (2012).
6. Omer, R. *et al.* Engineered Bacteria-Based Living Materials for Biotherapeutic Applications. *Front. Bioeng. Biotechnol.* **10**, 870675 (2022).
7. Gilbert, C. & Ellis, T. Biological Engineered Living Materials: Growing Functional Materials with Genetically Programmable Properties. *ACS Synth. Biol.* **8**, 1–15 (2019).
8. Ormandy, E. H., Dale, J. & Griffin, G. Genetic engineering of animals: Ethical issues, including welfare concerns. *Can. Vet. J.* **52**, 544–550 (2011).
9. Flemming, H.-C. *et al.* Biofilms: an emergent form of bacterial life. *Nat. Rev. Microbiol.* **14**, 563–575 (2016).
10. Flemming, H.-C., Neu, T. R. & Wozniak, D. J. The EPS Matrix: The “House of Biofilm Cells”. *J. Bacteriol.* **189**, 7945–7947 (2007).

11. Flemming, H.-C. & Wingender, J. The biofilm matrix. *Nat. Rev. Microbiol.* **8**, 623–633 (2010).
12. Gambino, M. & Cappitelli, F. Mini-review: Biofilm responses to oxidative stress. *Biofouling* **32**, 167–178 (2016).
13. Wan, N. *et al.* Bacterial Metabolism During Biofilm Growth Investigated by ¹³C Tracing. *Front. Microbiol.* **9**, (2018).
14. Yeor-Davidi, E., Zverzhinetsky, M., Krivitsky, V. & Patolsky, F. Real-time monitoring of bacterial biofilms metabolic activity by a redox-reactive nanosensors array. *J. Nanobiotechnology* **18**, 81 (2020).
15. Solokhina, A., Brückner, D., Bonkat, G. & Braissant, O. Metabolic activity of mature biofilms of *Mycobacterium tuberculosis* and other non-tuberculous mycobacteria. *Sci. Rep.* **7**, 9225 (2017).
16. Crouzet, M. *et al.* Exploring early steps in biofilm formation: set-up of an experimental system for molecular studies. *BMC Microbiol.* **14**, 253 (2014).
17. Maier, B. How Physical Interactions Shape Bacterial Biofilms. *Annu. Rev. Biophys.* **50**, 401–417 (2021).
18. Kovács, A. T., van Gestel, J. & Kuipers, O. P. The protective layer of biofilm: a repellent function for a new class of amphiphilic proteins. *Mol. Microbiol.* **85**, 8–11 (2012).
19. Beech, I. B. & Sunner, J. Biocorrosion: towards understanding interactions between biofilms and metals. *Curr. Opin. Biotechnol.* **15**, 181–186 (2004).
20. Gorby, Y. A. *et al.* Electrically conductive bacterial nanowires produced by *Shewanella oneidensis* strain MR-1 and other microorganisms. *Proc. Natl. Acad. Sci.* **103**, 11358–11363 (2006).

21. Gopinathan, J. & Noh, I. Recent trends in bioinks for 3D printing. *Biomater. Res.* **22**, 11 (2018).
22. Schaffner, M., Rühs, P. A., Coulter, F., Kilcher, S. & Studart, A. R. 3D printing of bacteria into functional complex materials. *Sci. Adv.* **3**, eaao6804 (2017).
23. Centurion, F. *et al.* Nanoencapsulation for Probiotic Delivery. *ACS Nano* **15**, 18653–18660 (2021).
24. González, L. M., Mukhitov, N. & Voigt, C. A. Resilient living materials built by printing bacterial spores. *Nat. Chem. Biol.* **16**, 126–133 (2020).
25. Jo, H. & Sim, S. Programmable Living Materials Constructed with the Dynamic Covalent Interface between Synthetic Polymers and Engineered *B. subtilis*. *ACS Appl. Mater. Interfaces* **14**, 20729–20738 (2022).
26. McKenney, P. T., Driks, A. & Eichenberger, P. The *Bacillus subtilis* endospore: assembly and functions of the multilayered coat. *Nat. Rev. Microbiol.* **11**, 33–44 (2013).
27. Perov, S. *et al.* Structural Insights into Curli CsgA Cross- β Fibril Architecture Inspire Repurposing of Anti-amyloid Compounds as Anti-biofilm Agents. *PLoS Pathog.* **15**, e1007978 (2019).
28. Mishra, S. *et al.* Biochemistry, Synthesis, and Applications of Bacterial Cellulose: A Review. *Front. Bioeng. Biotechnol.* **10**, (2022).
29. Chen, A. Y. *et al.* Synthesis and patterning of tunable multiscale materials with engineered cells. *Nat. Mater.* **13**, 515–523 (2014).
30. Tay, P. K. R., Nguyen, P. Q. & Joshi, N. S. A Synthetic Circuit for Mercury Bioremediation Using Self-Assembling Functional Amyloids. *ACS Synth. Biol.* **6**, 1841–1850 (2017).

31. Duraj-Thatte, A. M. *et al.* Modulating bacterial and gut mucosal interactions with engineered biofilm matrix proteins. *Sci. Rep.* **8**, 3475 (2018).
32. Duraj-Thatte, A. M. *et al.* Genetically Programmable Self-Regenerating Bacterial Hydrogels. *Adv. Mater.* **31**, 1901826 (2019).
33. Huang, J. *et al.* Programmable and printable *Bacillus subtilis* biofilms as engineered living materials. *Nat. Chem. Biol.* **15**, 34–41 (2019).
34. Lahiri, D. *et al.* Bacterial Cellulose: Production, Characterization, and Application as Antimicrobial Agent. *Int. J. Mol. Sci.* **22**, 12984 (2021).
35. Melton, L. Cellulose shoes made by bacteria. *Nat. Biotechnol.* **40**, 1163–1163 (2022).
36. Phisalaphong, M. *et al.* Chapter 14 - Nata de coco Industry in Vietnam, Thailand, and IndonesiaaaaMuenduen Phisalaphong, Tien-Khai Tran, Son Chu-Ky, and Fernando Dourado have contributed equally to this work. in *Bacterial Nanocellulose* (eds. Gama, M., Dourado, F. & Bielecki, S.) 231–236 (Elsevier, 2016). doi:10.1016/B978-0-444-63458-0.00014-7.
37. Caro-Astorga, J., Walker, K. T., Herrera, N., Lee, K.-Y. & Ellis, T. Bacterial cellulose spheroids as building blocks for 3D and patterned living materials and for regeneration. *Nat. Commun.* **12**, 5027 (2021).
38. Gilbert, C. *et al.* Living materials with programmable functionalities grown from engineered microbial co-cultures. *Nat. Mater.* **20**, 691–700 (2021).
39. Ramírez Tapias, Y. A., Di Monte, M. V., Peltzer, M. A. & Salvay, A. G. Bacterial cellulose films production by Kombucha symbiotic community cultured on different herbal infusions. *Food Chem.* **372**, 131346 (2022).
40. Biom mineralization - an overview | ScienceDirect Topics.
<https://www.sciencedirect.com/topics/materials-science/biom mineralization>.

41. Kamennaya, N. A., Ajo-Franklin, C. M., Northen, T. & Jansson, C. Cyanobacteria as Biocatalysts for Carbonate Mineralization. *Minerals* **2**, 338–364 (2012).
42. Heveran, C. M. *et al.* Biomineralization and Successive Regeneration of Engineered Living Building Materials. *Matter* **2**, 481–494 (2020).
43. Krajewska, B. Urease-aided calcium carbonate mineralization for engineering applications: A review. *J. Adv. Res.* **13**, 59–67 (2017).
44. Birnbaum, D. P., Manjula-Basavanna, A., Kan, A., Tardy, B. L. & Joshi, N. S. Hybrid Living Capsules Autonomously Produced by Engineered Bacteria. *Adv. Sci. Weinh. Baden-Wurt. Ger.* **8**, 2004699 (2021).
45. Rodriguez-Navarro, C. *et al.* The multiple roles of carbonic anhydrase in calcium carbonate mineralization. *CrystEngComm* **21**, 7407–7423 (2019).
46. Kim, I. G. *et al.* Biomineralization-based conversion of carbon dioxide to calcium carbonate using recombinant carbonic anhydrase. *Chemosphere* **87**, 1091–1096 (2012).
47. Wang, Y. *et al.* Living materials fabricated via gradient mineralization of light-inducible biofilms. *Nat. Chem. Biol.* **17**, 351–359 (2021).
48. Klemm, P. & Schembri, M. A. Bacterial adhesins: function and structure. *Int. J. Med. Microbiol. IJMM* **290**, 27–35 (2000).
49. Soto, G. E. & Hultgren, S. J. Bacterial Adhesins: Common Themes and Variations in Architecture and Assembly. *J. Bacteriol.* **181**, 1059–1071 (1999).
50. Paharik, A. E. & Horswill, A. R. The Staphylococcal Biofilm: Adhesins, regulation, and host response. *Microbiol. Spectr.* **4**, 10.1128/microbiolspec.VMBF-0022–2015 (2016).
51. Coutte, L. *et al.* Role of Adhesin Release for Mucosal Colonization by a Bacterial Pathogen. *J. Exp. Med.* **197**, 735–742 (2003).

52. Wells, T. J. *et al.* EhaA is a novel autotransporter protein of enterohemorrhagic *Escherichia coli* O157:H7 that contributes to adhesion and biofilm formation. *Environ. Microbiol.* **10**, 589–604 (2008).
53. Schüürmann, J., Quehl, P., Festel, G. & Jose, J. Bacterial whole-cell biocatalysts by surface display of enzymes: toward industrial application. *Appl. Microbiol. Biotechnol.* **98**, 8031–8046 (2014).
54. Ruano-Gallego, D., Fraile, S., Gutierrez, C. & Fernández, L. Á. Screening and purification of nanobodies from *E. coli* culture supernatants using the hemolysin secretion system. *Microb. Cell Factories* **18**, 47 (2019).
55. Glass, D. S. & Riedel-Kruse, I. H. A Synthetic Bacterial Cell-Cell Adhesion Toolbox for Programming Multicellular Morphologies and Patterns. *Cell* **174**, 649–658.e16 (2018).
56. Chen, B. *et al.* Programmable living assembly of materials by bacterial adhesion. *Nat. Chem. Biol.* **18**, 289–294 (2022).
57. Molinari, S. *et al.* A de novo matrix for macroscopic living materials from bacteria. *Nat. Commun.* **13**, 5544 (2022).
58. Ford, M. J., Nomellini, J. F. & Smit, J. S-Layer Anchoring and Localization of an S-Layer-Associated Protease in *Caulobacter crescentus*. *J. Bacteriol.* **189**, 2226–2237 (2007).

Chapter 2

Growing Cohesive Bacterial Films on Perforated Scaffolds

1. Abstract

In this chapter, I describe a suction-coating method that allows one to grow bacterial films on perforated scaffolds. Polycarbonate membrane filters with 0.2 μm pore size were found to be ideal perforated scaffolds for growing bacterial films on agar plates. Using an *E. coli* strain that displays SpyTag-SpyCatcher chemistry on the cell surface, we explored the factors that affect cohesiveness of bacterial films. Separation between SpyTag and SpyCatcher expressing cells were observed in films made of mixed cells and flow cytometry data confirmed that surface display proteins were constitutively expressed in these films. To determine whether the displayed protein was crucial for making bacterial films cohesive, erosion tests were performed for films containing only SpyTag and SpyCatcher expressing cells. Erosion test results revealed that SpyTag expressing cells alone can form cohesive bacterial films while SpyCatcher expressing cells cannot. These results encouraged us to develop a double-plasmid strain that constitutively expresses SpyTag and expresses SpyCatcher only under L-arabinose induction. Films grown from this strain were cohesive and contained SpyTag-SpyCatcher covalent interactions. Knowing the SpyTag peptide was tethered to an elastin-like-peptide (ELP) linker when surface-displayed, we engineered an *E. coli* strain that displays only the unstructured ELP at the cell surface and discovered that films formed by this strain remained cohesive against erosion. To test the hypothesis that unstructured peptide surface display is the major contributor to bacterial film cohesion, we devised a construct that expresses another unstructured peptide called Xten. Erosion test results showed that Xten expressing films are also cohesive against

erosion. In the end, we concluded that unstructured peptides displayed at the cell surface play an essential role in intercellular adhesion; films formed by cells overexpressing these unstructured peptides are cohesive and remain stable against erosion. These results prompted us to develop a single-plasmid system that enables constitutive expression of unstructured peptides at the cell surface and can form covalent intercellular interactions as described in Chapter 3.

2. Introduction

In the last decade, the field of engineered living materials has emerged at the interface between synthetic biology and materials science. Engineered living materials are genetically programmable materials with attributes of living systems.¹⁻³ Inspired by natural biofilms,^{4,5} several research groups have published work on either engineering bacterial matrix secretion systems⁶⁻⁸ or bacterial aggregation systems^{9,10} to generate living materials with multiple functions. The materials have been collected mostly under liquid culture conditions and must be harvested from liquid media before analysis. Other approaches use synthetic polymer matrices to encapsulate bacteria of interest.^{11,12} In such systems, the material is not self-assembled by living organisms and requires the introduction of synthetic polymers to provide material cohesion and integrity.

In this report, we envisioned a material that is autonomously assembled from a single living bacterium. Such engineered bacteria display associative proteins at the cell surface so that a single bacterium can proliferate and then aggregate into a bulk material without secreted or synthetic polymeric matrices. We also aimed to use solid state culture methods in which the material can be grown on a perforated solid support, exposed directly to the air. Such perforated scaffolds allow nutrients and water to support growth of the living material while preventing cells to pass through. By controlling the number of bacteria coated on the perforated scaffold, we can prepare cm-scale materials without the need for separate collection and casting steps.

3. Results and Discussion

3.1 Finding suitable materials and methods for growing living bacterial films

Traditionally, researchers grow bacteria directly on agar plates. For our purposes, however, agar plates are not sufficient. We must replenish the nutrition and moisture to our bacterial films, and be able to detach them for analysis as materials. To address these requirements, we envisioned a 3-layer structure (**Fig 2.1a**) for bacterial film growth. The top layer is a living bacterial film, separated from a bottom nutrition layer (agar plate) by a perforated middle layer. Ideally, this perforated layer would allow moisture and nutrition to pass through and feed the bacteria on top while preventing bacteria from passing through and contaminating the bottom layer. For this purpose, we modified the “colony biofilm” culture method,¹³ which met our requirements (**Fig 2.1b**). In this method, the biofilm is separated from agar medium by a polycarbonate filter. Biofilms grown on polycarbonate filters can be transferred to multiple agar plates containing different antibiotics and different levels of nutrition. This method allows extended growth of biofilms on the solid support with replenished media and controlled induction of protein expression by transferring the bacterial film to a plate containing a chemical inducer.

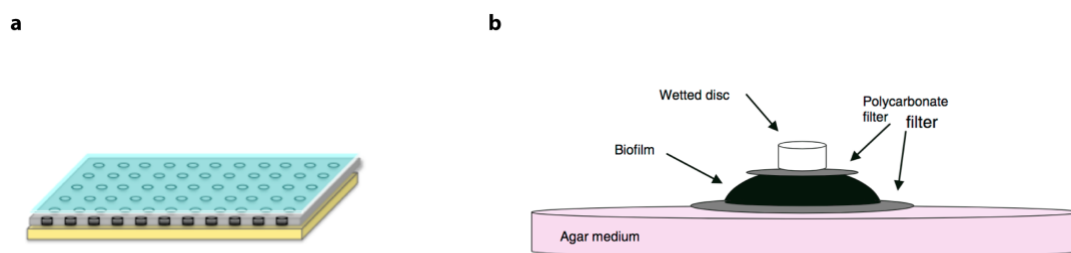


Figure 2.1. Schematic of growing bacterial film on perforated scaffolds. a, Schematics of a 3-layer living material. **b,** Colony biofilm culture method.

The first task was to select polycarbonate filters with pore size that would prevent bacteria from contaminating the agar medium. Polycarbonate filters (nuclepore,

Whatman) with pore size ranging from 0.1 μm to 0.8 μm were placed on LB¹⁴ agar plates. Aliquots (5 μl) of overnight cultures of MG1655 *E. coli* cells in LB media (diluted to $\text{OD}_{600} < 0.05$) were dropped onto the polycarbonate filters. The bacterial colonies were left in a 37 °C incubator for 2 days and examined for bacterial contamination on the agar. We found that bacteria can pass through filters with pore sizes of 0.6 μm and 0.8 μm (**Fig 2.2a**). Similar experiments were performed with polycarbonate filters with pore sizes of 0.1, 0.2 and 0.4 μm . After 2 days of incubation, the polycarbonate filters with bacteria grown on top were removed and the agar plates beneath were left in the 37 °C incubator for another day. As shown in **Fig 2.2b**, plates in contact with 0.1 and 0.2 μm pore-sized polycarbonate filters had no colony formation while 0.4 μm did. This result suggests that only polycarbonate filters with pore size \leq 0.2 μm can effectively block bacteria from accessing the underlying agar plate. As shown in **Fig 2.3**, the pores of 0.2 μm polycarbonate filters are much smaller than MG1655 *E. coli* cells. To ensure the flow of nutrient and water is sufficient to the bacterial film growth, we used 0.2 μm pore-sized polycarbonate membrane filters for all future experiments. I think you can cite prior papers that use 0.2 micron filters.

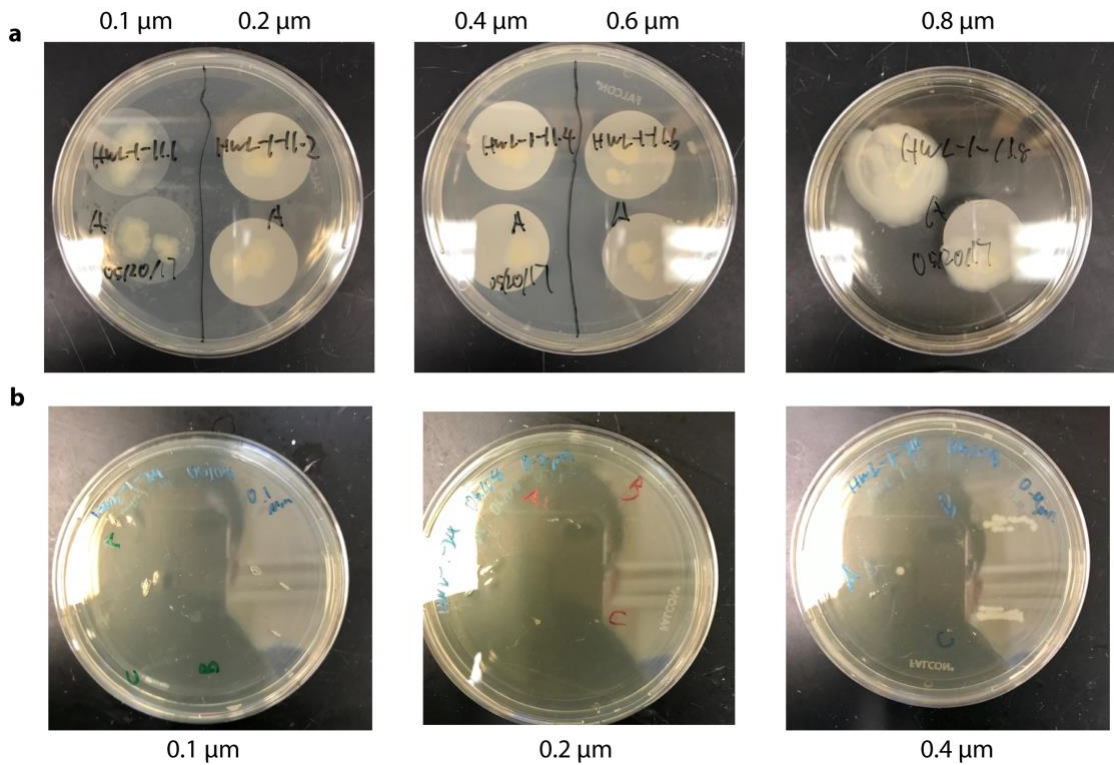


Figure 2.2. Polycarbonate filters with pore size $\leq 0.2 \mu\text{m}$ can effectively block bacterium from contaminating the agar. a, Images of 2 days old bacterial colonies grown on polycarbonate filters. The diameter of each filter is 2.5 cm. The pore size of each kind of polycarbonate filter is shown above the image. **b,** Plates left in 37 °C incubator for 1 day after polycarbonate filter with bacterial colonies growing on top was removed. The pore size of membrane filters were shown below. I wouldn't show these images. They are hard to see, and if I'm understanding things correctly, your reflection shows in part b. I believe we talked about the quality of images of this kind when you first acquired them. I also think it has been established previously that 0.2 micron filters are needed to retain bacteria, so this doesn't require extended discussion.

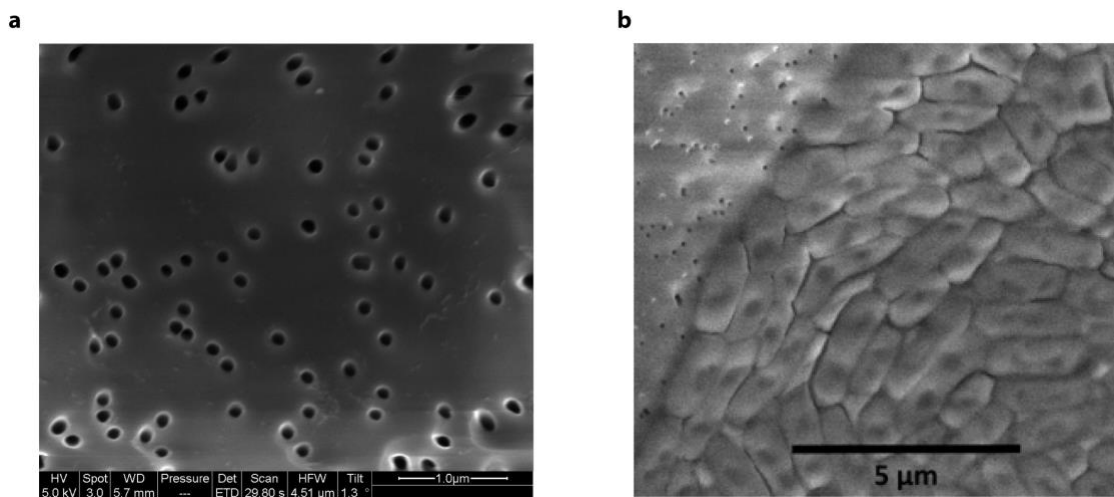


Figure 2.3. ESEM image of 0.2 μm pore-sized polycarbonate filter and bacterial cells grow on top a, Environmental scanning electron microscopy (ESEM) image of polycarbonate filter claimed to have pore size around 0.2 μm . Scale bar, 1 μm . **b,** ESEM image of MG1655 *E. coli* grown on top of 0.2 μm pore-sized polycarbonate filter.

2.2 Suction coating to form cohesive bacterial films using SpyTag-SpyCatcher chemistry

We developed a method called “suction coating” (**Fig 2.4a**) to efficiently coat polycarbonate filters with bacteria. Individual colonies harvested from LB plates were grown overnight to stationary phase in liquid LB medium supplemented with 100 mg/L ampicillin to maintain plasmid stability. The resulting cultures were then diluted to an optical density at 600 nm (OD_{600}) of approximately 0.8. Diluted cultures were loaded on UV-sterilized track-etched polycarbonate filters (Nuclepore Whatman, 0.2 μm pore size) mounted in vacuum filter units (Nalgene Rapid-flow Thermo-Fisher). For 2.5 cm diameter polycarbonate filters, 200 μL culture volumes were loaded and vacuum filtered to produce roughly circular bacterial layers with diameters around 2 cm. After filtration was complete, filters were transferred to fresh LB plates. Bacterial films were grown in a 37 °C incubator. Filters were moved to fresh LB agar plates containing 100 mg/ml ampicillin every day for 7 days to allow film maturation and mechanical testing.

In order to “glue” cells together to form cohesive bacterial films, we started with SpyTag-SpyCatcher surface display constructs previously used by our laboratory to generate aggregates in planktonic culture.¹⁵ SpyTag and SpyCatcher are derived from the fibronectin-binding protein FbaB of *Staphylococcus pyogenes*, as first reported by Howarth and coworkers.^{16,17} After splitting the full length protein into two polypeptide chains, the resulting SpyTag and SpyCatcher fragments undergo spontaneous reaction via formation of an isopeptide bond between lysine residue K31 in SpyCatcher and aspartic acid residue D117 in SpyTag. By fusing SpyTag to a 125-amino acid elastin-like-peptide linker (designated E6) previously used by our laboratory for making hydrogels^{18–20} and SpyCatcher to an EhaA autotransporter (AT) domain,²¹ we were able

to display SpyTag and SpyCatcher peptides at the *E. coli* cell surface and generate aggregates in planktonic culture.¹⁵ Sequences encoding SpyTagE6-AT (plasmid name: pAT-ST) and SpyCatcher-AT (plasmid name: pAT-SC) proteins were introduced into pQE80 plasmids under control of a T5-lac promoter. The plasmids encoding SpyTagE6-AT and SpyCatcher-AT proteins were transformed into DH10B *E. coli* cells. We grew overnight cultures of SpyTagE6-AT and SpyCatcher-AT DH10B, then diluted both cultures to OD₆₀₀ ca. 0.8. We mixed SpyTagE6-AT and SpyCatcher-AT expressing cells at a 1:1 ratio (**Fig 2.4 b**) and coated 200 μ l of mixed culture onto polycarbonate filters. Bacterial films were grown at 37 °C for 3 days on LB agar plates containing 100 mg/ml ampicillin but no IPTG (LB agar plates were changed on a daily basis to ensure fresh nutrition was supplied to bacterial films). Surprisingly, we found that mixed SpyTag-SpyCatcher films, without IPTG induction, were already cohesive and could be peeled intact from the polycarbonate filter as shown in **Fig 2.4c**.

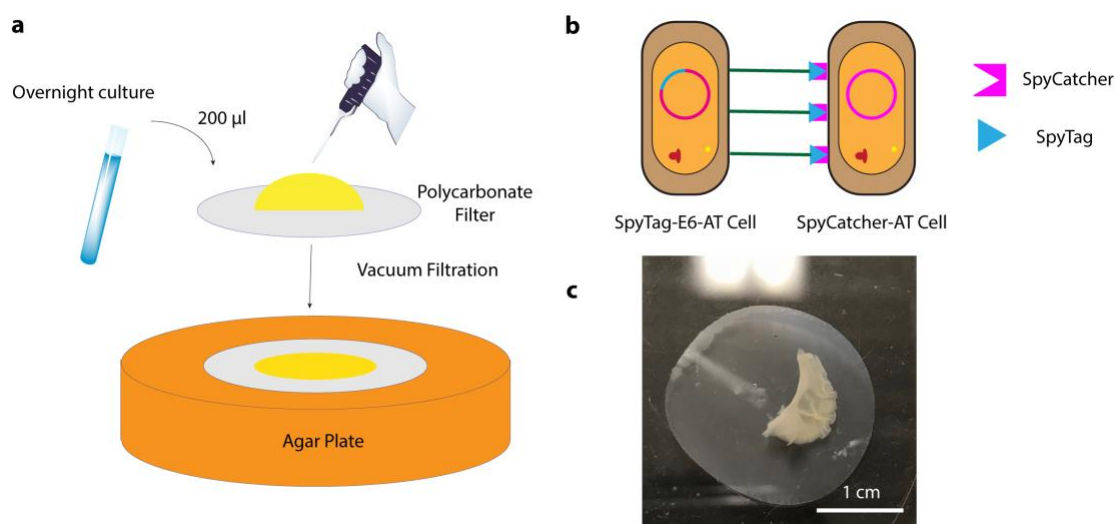


Figure 2.4. Scheme of suction coating method and SpyTag-SpyCatcher expressing bacteria **a**, Scheme of suction coating method. **b**, Schematic of cells expressing SpyTagE6-AT proteins and SpyCatcher-AT proteins. SpyTag and SpyCatcher react with each other covalently. **c**, Image of a 7 day old bacterial film made of SpyTag & SpyCatcher expressing cells starting with 1:1 ratio. The film stays cohesive in water, and can be peeled from polycarbonate. Scale bar, 1 cm.

To test our hypothesis that the cohesiveness of mixed SpyTag-SpyCatcher films comes from intercellular adhesion caused by SpyTag-SpyCatcher isopeptide bond formation

and homogeneous mixing of SpyTagE6-AT cells and SpyCatcher-AT cells, we ran flow cytometry on SpyTagE6-AT films and SpyCatcher-AT films and grew a mixed film made of mCherry-expressing SpyTagE6-AT cells and mWasabi-expressing SpyCatcher-AT cells at 1:1 ratio (**Fig 2.5a**). The flow-cytometry data are shown in **Fig S2.1**. Surprisingly, without IPTG induction, SpyTagE6-AT proteins showed high expression compared to the negative control, indicating that the promoter is leaky in the DH10b strain. SpyCatcher-AT cultures, on the other hand, contain a small population characterized by high expression levels but most of the cells exhibit labeling intensity similar to that of the negative control. These results called into question the hypothesis that SpyTag-SpyCatcher covalent bonds were the major source of cohesion in the mixed films, since the SpyCatcher-AT expression level was much lower than that of SpyTagE6-AT. Since SpyTag and SpyCatcher form a strong covalent interaction, it is still possible that a small amount of SpyTag-SpyCatcher covalent crosslinking can contribute to the cohesion of the film. The results from mixed fluorescent cell experiments, however, disprove this hypothesis. As shown in the low magnification microscopy image in **Fig 2.5b**, mWasabi-expressing SpyCatcher-AT cells (Green) spread out everywhere in the film while mCherry-expressing SpyTagE6-AT cells (Red) form islands and patches in the green lawn of SpyCatcher-AT cells. Under higher magnification (**Fig 2.5c**), we observed that mCherry-expressing SpyTagE6-AT formed densely packed aggregates with mWasabi-expressing SpyCatcher-AT cells distributed around them. This result suggests that SpyTagE6-AT cells tend to self-aggregate and that mixing of SpyTag and SpyCatcher cells isn't homogeneous. To further understand the mechanism behind SpyTagE6-AT self-association and to rule out the possibility that low expression of SpyCatcher was the cause of separation between SpyTag and SpyCatcher expressing cells, we transferred SpyTagE6-AT and SpyCatcher-AT to a

pBAD33 plasmid to ensure that protein would be expressed only upon addition of L-arabinose. Work¹⁵ done by previous group members had already shown that SpyCatcher-AT when induced by L-arabinose expresses at levels similar to that of SpyTagE6-AT. We transformed the pBAD33 plasmid containing protein of interest into DH10B cells with chromosomally encoded fluorescent protein expression (**Fig 2.5d**) and prepared 1:1 mixed films using protocols similar to that described earlier. One film was placed on an LB agar plate without L-arabinose while the other was placed on an LB agar plate containing 0.1% L-arabinose. After 3 days of incubation at 37 °C, the films were imaged on a ChemiDoc Gel imager; the resulting images are shown in **Fig 2.5e,f**. In **Fig 2.5e**, cells without surface protein expression are homogeneously mixed as shown by the red and green colors of the marker proteins mixed into yellow. In **Fig 2.5f**, however, separation between mCherry SpyTagE6-AT expressing cells and mWasabi SpyCatcher-AT expressing cells is observed. The SpyTagE6-AT-expressing red cells formed small aggregates hundreds of microns in diameter, which can be seen by naked eye. Green SpyCatcher-AT expressing cells behaved similarly as in **Fig 2.5b&c** with cells growing everywhere. These results suggested that SpyTagE6-AT expressing cells can self-associate and might play the major role in generating cohesive behavior in the mixed SpyTag-SpyCatcher film.

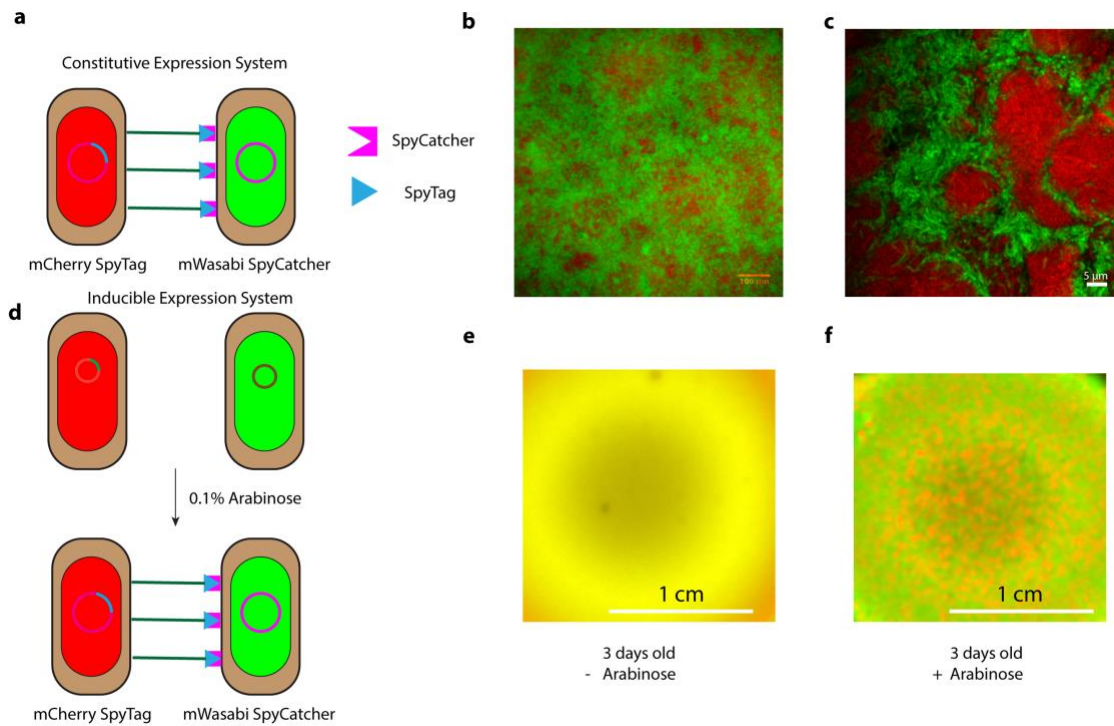


Figure 2.5. Scheme of growing mixed SpyTag-SpyCatcher films with fluorescent protein tags **a**, Scheme of mixing mCherry SpyTag expressing cells and mWasabi SpyCatcher expressing cells. **b**, Low magnification microscopy image of mixed film with fluorescence. Green corresponds to mWasabi SpyCatcher cells and Red corresponds to mCherry SpyTag cells. Scale bar, 100 μm. **c**, High magnification microscopy image of mixed film with fluorescence. Green corresponds to mWasabi SpyCatcher cells and Red corresponds to mCherry SpyTag cells. Scale bar, 5 μm. **d**, Scheme of mixing mCherry SpyTag expressing cells and mWasabi SpyCatcher expressing cells under control of an araBAD promoter. SpyTag and SpyCatcher are expressed only in the presence of 0.1% arabinose. **e**, Gel imager image of 3 days old mixed SpyTag-SpyCatcher film without arabinose in the medium. Green corresponds to mWasabi SpyCatcher cells and Red corresponds to mCherry SpyTag cells. Scale bar, 1 cm. **f**, Gel imager image of 3 day-old mixed SpyTag-SpyCatcher film with 0.1% arabinose in the medium. Green corresponds to mWasabi SpyCatcher cells and Red corresponds to mCherry SpyTag cells. Scale bar, 1 cm.

2.3 Surface-display of elastin-like-peptide contributes to bacterial film cohesiveness

To quantitatively characterize the degree of cohesiveness of bacterial films with surface protein expression, we used an erosion assay. A 7-day-old bacterial film grown on a membrane filter was immersed in 7 mL of 1x PBS buffer at pH 7.4 in a well of a 6-well plate (Corning, Thermofisher). The 6-well plate was then placed on a rocking platform (Bio-Rad) set at 15 ° tilt angle and 15 rpm frequency. The OD₆₀₀ of PBS in contact with the bacterial film was measured 1 h and 24 h after rocking started. If the bacterial film was cohesive enough to withstand erosion from shaking PBS buffer, few cells would

be released and the OD₆₀₀ value of the PBS buffer would remain low. If a bacterial film was not cohesive, many more cells would be washed off and the OD₆₀₀ value of the PBS buffer would increase more substantially.

The erosion assay results are presented in **Fig 2.6** with all engineered proteins encoded in pQE80 plasmids. First, the control group, which is film formed by DH10B cells carrying empty pQE80 plasmid was examined. Flow cytometry data in **Fig S2.2** (QH group), indicated minimal protein expression at the surface. The OD₆₀₀ value of PBS in contact with the control increased to 0.1 after 1 h of erosion and the buffer was turbid when viewed with the naked eye. After 24 h of erosion, the OD₆₀₀ increased to roughly 0.3 and the films were disintegrating. This behavior can be used as the standard for a non-cohesive bacterial film. Erosion assay results for STE6-AT (ST = SpyTag) and SC-AT (SC = SpyCatcher) were consistent with the results reported in the previous section. After 1 h of erosion, OD₆₀₀ of STE6-AT is only 0.001 and after 24 h remained around 0.01, an order of magnitude lower than that of the control. SC-AT on the other hand is even less cohesive compared to the control. These results are consistent with the hypothesis that surface-display of STE6-AT plays a major role making mixed films cohesive.

What's causing the STE6-AT film to be cohesive? Is it the SpyTag peptide displayed at the end of the protein or the unstructured elastin-like-peptide that connects SpyTag with the autotransporter? We cloned a construct with only E6 displayed at the surface and designated it E6-AT. As shown in **Fig S2.2**, flow cytometry confirmed that E6-AT was expressed at a level similar to that of STE6-AT in the bacterial film. The erosion assay results showed that E6-AT and STE6-AT were both cohesive with similar OD₆₀₀ values at both 1 h and 24 h. This result suggests that surface display of the unstructured elastin-like peptide is sufficient to stick cells together and form cohesive films. We

wondered whether similar results would be observed with other unstructured peptides. To address this question, we cloned another unstructured peptide Xten²² to be displayed on the *E. coli* surface. Xten is an unstructured hydrophilic peptide made of amino acids A, G, E, P, S, and T and can be used to increase protein solubility²³ and extend half-life of biological active biomolecules²⁴. We cloned an Xten variant 144 amino acids long to make it comparable to E6 (152 aa) and ran flow cytometry to confirm expression at similar levels. The results were consistent with our expectation that Xten-AT would enhance film cohesion, though after 24 h of erosion, more Xten-AT cells were washed off compared to E6-AT(**Fig 2.6**).

Understanding that display of unstructured peptides can cause cell aggregation and make cohesive bacterial films, we sought to incorporate moieties that are known to self-associate through more well-defined interactions. We cloned the “A” coiled-coil peptide²⁵ previously used in our laboratory to control the mechanical behavior of protein hydrogels.^{19,20,26} The “A” coiled-coil peptides form tetrameric α -helical bundles.²⁶ We hoped that introducing coiled-coil proteins would generate more cohesive bacterial films with greater mechanical strength. Although we saw AE6-AT proteins could be expressed at levels similar to those of other constructs, the erosion assay results implied that AE6-AT film is not as cohesive as E6-AT film alone. This result prompted us to develop a cysteine-based strategy to enhance mechanical properties of bacterial films as described in Chapter 3.

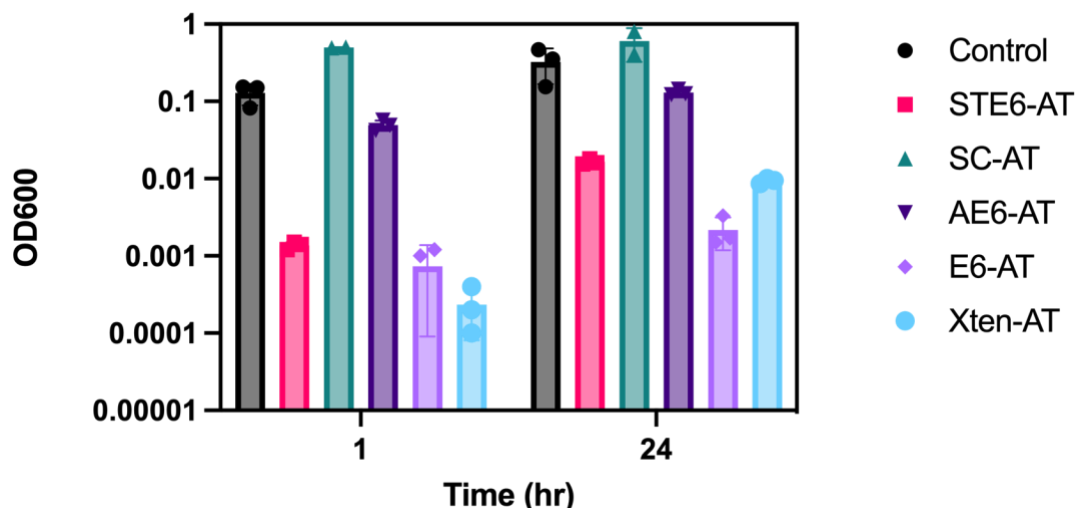


Figure 2.6. Erosion assay data of different films. STE6-AT stands for SpyTagE6-AT and SC-AT stands for SpyCatcher-AT. AE6-AT, A is a self-associative coiled-coil protein. All groups except SC-AT were run in triplicate. SC-AT was run in duplicate.

2.4 Using a double plasmid system to generate cohesive films with SpyTag-

SpyCatcher covalent crosslinks

Knowing that STE6-AT protein is self-associative while SC-AT is not, we explored a different strategy to generate cohesive bacterial films containing SpyTag-SpyCatcher covalent crosslinks. Inspired by work using antigen-nanobody interaction to generate *E. coli* assembly,²⁷ we developed a double plasmid strategy (**Fig 2.7a**) to generate a film containing SpyTag-SpyCatcher covalent bonds. In the double plasmid system, DH10B cells were transformed with a pQE80 plasmid encoding the STE6-AT protein and a pBAD33 plasmid encoding the SC-AT protein. When encoded in the pQE80 plasmid, STE6-AT are constitutively expressed to give films cohesive properties. When 0.1% L-arabinose is present in the agar, expression of SC-AT is turned on and individual *E. coli* cells express both STE6-AT and SC-AT, allowing isopeptide bond formation either intracellularly or intercellularly. In order to detect expression of both STE6-AT and SC-AT in western blot, we replaced the 6 x His tag in SC-AT with a FLAG tag. We also engineered a series of STE_x-AT proteins in pQE80 plasmids, with

x = 3, 6, 9, 12 and transferred these plasmids into cells containing pBAD33 encoding a SpyCatcher-AT protein with FLAG tag instead of 6 x His tag (plasmid name: pBAD-SpyCatcher). We grew a series of these films under 0.1% arabinose induction for a week and lysed them in 100°C 4% SDS buffer for 0.5 h. The high temperature was required because of the high thermostability of autotransporter proteins.²⁸ We stained the western blot with Dylight 488 anti-His tag antibody and Dylight 647 anti-FLAG tag antibody to visualize the proteins of interest. As shown in **Fig 2.7b**, the STE_x-AT proteins were labeled by green fluorescence, forming a beautiful molecular ladder, while (FLAG)SC-AT was labeled by red fluorescence at the same mass across all lanes. It's exciting that the SpyTag-SpyCatcher reacted protein bands were also visible above > 100 kDa mass range with mass directly proportional to the length of elastin linker. The reacted product band was labeled both by anti-His tag antibody and anti-FLAG tag antibody, confirming its identity as the reaction product. Erosion assays were performed on pQE80 STE₆-AT & pBAD33 SC-AT with and without arabinose induction. Interestingly, though induced films could be picked up more easily using tweezers compared to the uninduced films, the erosion assay suggested that induced films containing SpyTag-SpyCatcher crosslinks are less cohesive against erosion compared to uninduced films as shown in **Fig 2.7c**. It's likely that induction caused stress in the film and reduced the number of viable cells (**Fig S2.3**). These results prompted us to find a single plasmid, induction-free system that contains covalent crosslinks to enhance mechanical strength of bacterial films. Such a system, using disulfide crosslinks, will be discussed in chapter 3.

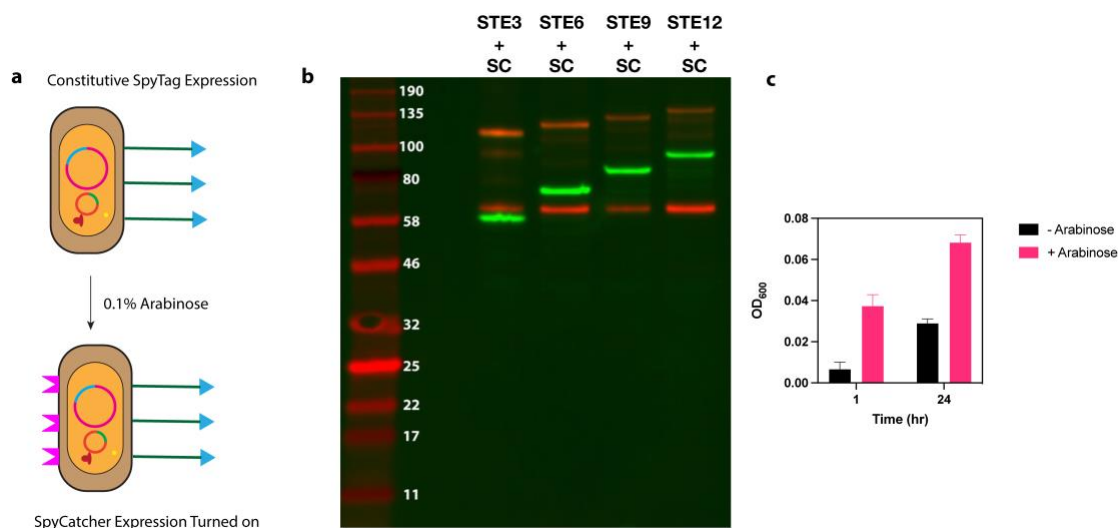


Figure 2.7. Double plasmid system of SpyTag-SpyCatcher film. **a.** Schematic of dual plasmid system. **b.** Western blot image of SpyTag-SpyCatcher films with different linker length of elastin. **c.** Erosion assay result of pQE80 STE6-AT & pBAD33 SC-AT with or without arabinose induction. Make panel c larger and move key inside.

4. Conclusion

An efficient suction-coating method was developed to grow bacterial films on perforated polycarbonate membrane filter with 0.2 μm pore size, with nutrition supplied by LB agar plates. Using the SpyTag-SpyCatcher model system, we explored a series of related strategies for growing cohesive bacterial films using protein surface-display methods. Unexpectedly, display of unstructured peptides, specifically elastin-like-peptides and Xten, is sufficient to generate cohesive bacterial films. Using a double plasmid system, we managed to grow cohesive bacterial films containing SpyTag-SpyCatcher covalent crosslinks, but erosion assay results revealed that they are not as cohesive as SpyTag expressing films alone. These results build foundations for our next steps of making cohesive bacterial films with enhanced mechanical strength from covalent crosslinks between the cells. We envisioned an engineered *E. coli* strain carrying single plasmid that drives constitutive expression of unstructured elastin at surface and a cysteine addition at the exposed end of elastin would cause disulfide bond formation between cells. The results of such system will be discussed in Chapter 3.

5. Materials and Methods

Bacterial Strains. Most experiments were conducted in *E. coli* strain DH10B (Invitrogen, Carlsbad, CA). Only in experiments used to determine the ideal pore size of polycarbonate filters was the MG1655 strain of *E. coli* used. Details of reagents, cloning and protein expression experiments can be found in **Table S2.1** and **Supplementary Notes 2.1-2**.

Preparation of Bacterial Films. Individual colonies harvested from LB plates were grown overnight to stationary phase in liquid LB medium supplemented with 100 mg/L ampicillin to maintain plasmid stability. The resulting cultures were then diluted to an optical density at 600 nm (OD₆₀₀) of approximately 0.8. Diluted cultures were loaded on UV-sterilized track-etched polycarbonate filters (Nuclepore Whatman, 0.2 µm pore size) mounted in vacuum filter units (Nalgene Rapid-flow Thermo-Fisher). For 2.5 cm diameter polycarbonate filters, 200 µL culture volumes were loaded and vacuum filtered. After filtration was complete, filters were transferred to fresh LB plates. Bacterial films were grown in a 37 °C incubator. Filters were moved to fresh LB agar plates containing suitable antibiotics every day for 7 days to allow film maturation and mechanical testing.

Erosion Assay. A 7 day old bacterial film grown on membrane filters was immersed in 7 mL of 1x PBS buffer at pH 7.4 in a well of 6-well plate (Corning, Thermofisher). The 6-well plate was then placed on a rocking platform (Bio-Rad) set at 15 ° tilt angle and 15 rpm frequency. The OD₆₀₀ of PBS in contact with the bacterial film was measured at 1 h and 24 h after rocking started.

Imaging Bacterial Films and Western Blots. Bacterial films grown on polycarbonate filters on agar plate were placed in the chamber of a ChemiDoc XRS+ Imager (Bio-Rad) and the appropriate channel – either bright field or fluorescence – was selected. The Imager automatically imaged the film. The same method was applied to Western Blot imaging.

Sample Mounting and ESEM Imaging. Bacterial films grown on polycarbonate filters were stuck to a conductive copper tape on a metal sample platform. The platform was then placed in the chamber of a Quanta 200 F (FEI, now Thermo Fisher) scanning electron microscope (SEM). The SEM was turned to environmental SEM (ESEM) mode with 0.2 mBar pressure in the chamber. Voltage applied to the sample is tuned between 3 kV and 5 kV.

Flow Cytometry. Bacterial films were scraped from their filters and transferred to Eppendorf tubes, blocked for 30 min with agitation (3% BSA in PBS). Cells were then centrifuged and resuspended in staining solution [5 µg/mL Anti-His conjugated Dylight 488 Antibody (HIS.H8 Thermofisher), 1% BSA in PBS]. The suspension was agitated for 1 h, after which the cells were washed three times in PBS. Cells were strained through a 40 µm filter to remove aggregates and run on a MoFlo XDP cell sorter equipped with a 488 nm laser. Flow cytometry data were analyzed using MatLab.

Fluorescence Imaging. Fluorescence images of processed samples with fluorescent labels were obtained with a 63X, 1.518 N.A. oil-immersion objective on a Zeiss LSM 880 confocal microscope (Carl Zeiss AG, Oberkochen, Germany) at the Caltech

Biological Imaging Facility. Single-photon confocal laser scanning imaging was performed with 488-nm and 591-nm lasers with read-out in the mWasabi ($\lambda_{ex}/\lambda_{em}$: 493/509 nm) and mCherry Channels ($\lambda_{ex}/\lambda_{em}$: 587/610 nm). Images were visualized and analyzed with Fiji or Imaris Viewer. (Oxford Instruments, Abingdon, UK)

6. Acknowledgements and Contributions

Hanwei Liu conceived and designed the experiments under the supervision of Professor David A. Tirrell. Hanwei Liu was responsible for all the genetic engineering experiments, bacterial film growth, sample preparation and fluorescence imaging. Fluorescence microscopy was done at the Biological Imaging Facility (BIF) of the Beckman Institute at Caltech. The Shapiro laboratory provided the gel imaging system used for imaging bacterial films and western blots. ESEM imaging was done at the Kavli Nanoscience Institute (KNI) at Caltech. Dr. Bradley Silverman performed flow cytometry.

7. Supporting Information

Supplementary Note 2.1: Reagents and suppliers

Restriction enzymes, ligase, and Q5 DNA polymerase were purchased from New England Biolabs (Beverly, MA). DNA oligos and G-blocks were purchased from Integrated DNA Technologies (Coralville, IA).

Supplementary Note 2.2: Plasmid subcloning

Recombinant fusion proteins were produced by standard recombinant DNA technology. *E. coli* strain DH10B was used for all cloning steps and material preparation.

Genes encoding the autotransporter protein along with elastin solubility/stability tags have been previously cloned by our group into modified pQE-80L plasmids.

pBAD-SpyCatcher(FLAG) was made by site directed mutagenesis from pBAD-SpyCatcher with primers designed on the NEB base changer website²⁹ and 6 x His tag was mutated into FLAG Tag using PCR.

pX-E6 plasmid containing 6 elastin-like-peptide repeat reported in previous works^{15,20,30} with 5' BamHI and 3' XhoI was digested by corresponding enzymes and inserted into BamHI and XhoI digested pAT-ST vector to make pAT-E6 plasmid.

pAT-Xten plasmid was created by ordering a G-Block containing 144 aa Xten sequence containing 5' BamHI and 3' XhoI restriction sites. The G-Block was digested by BamHI and XhoI restriction enzymes and ligated with a BamHI and XhoI digested pAT-ST vector to make pAT-E6 plasmid.

pAT was made by first digesting pAT-ST vector with Sall and XhoI restriction enzymes and then ligate the vector. (Sall and XhoI sites can be ligated together).

pAT-ST(E3), pAT-ST(E9) and pAT-ST(E12) was made by digesting pX-E3, pX-E9, pX-E12 plasmid with Sall and HindIII restriction enzyme and the insert DNA encoding elastin-like-peptide was purified. pX-ST plasmid was digested by XhoI and HindIII restriction enzyme and vector was purified. By ligating insert with elastin-like-peptide sequence and vector containing Spytag sequence, pX-ST(E3), pX-ST(E9) and pX-ST(E12) was made. , pX-ST(E3), pX-ST(E9) and pX-ST(E12) were then digested by

BamHI and XhoI restriction enzymes and ligated with a BamHI and XhoI digested pAT-ST vectors to make pAT-ST(E3), pAT-ST(E9) and pAT-ST(E12) plasmid. The sequence of all constructs were sequenced and confirmed by Laragen Inc. (Culver City, CA).

Supplementary Note 3.3: Buffer recipe

The 1x PBS buffers used in this work was purchased from ThermoFisher Scientific containing 155 mM NaCl, 1 mM KH₂PO₄ and 3 mM Na₂HPO₄ buffered at pH 7.4.

Table S2.1: Plasmids used in this study

Name	Backbone/origin/promoter	Purpose
pQE-Empty	pQE801/colE1/T5	Empty plasmid for cloning and providing ampicillin resistance
pAT-E6	pQE801/colE1/T5	Constitutive expression of E6-AT protein on cell surface
pAT-ST	pQE801/colE1/T5	Constitutive expression of SpyTagE6-AT protein on cell surface
pX-E3	pQE801/colE1/T5	Cloning of pAT-ST(E3)
pX-E6	pQE801/colE1/T5	Cloning of pAT-E6
pX-E9	pQE801/colE1/T5	Cloning of pAT-ST(E9)
pX-E12	pQE801/colE1/T5	Cloning of pAT-ST(E12)
pX-ST(E3)	pQE801/colE1/T5	Cloning of pAT-ST(E3)
pX-ST(E9)	pQE801/colE1/T5	Cloning of pAT-ST(E9)
pX-ST(E12)	pQE801/colE1/T5	Cloning of pAT-ST(E12)

pAT-ST(E3)	pQE801/colE1/T5	Constitutive expression of SpyTagE3-AT protein on cell surface
pAT-ST(E9)	pQE801/colE1/T5	Constitutive expression of SpyTagE9-AT protein on cell surface
pAT-ST(E12)	pQE801/colE1/T5	Constitutive expression of SpyTagE12-AT protein on cell surface
pAT-SpyCatcher	pQE801/colE1/T5	Constitutive expression of SpyCatcher-AT protein on cell surface
pBAD-SpyCatcher	pBAD33/p15a/pJ23100	Arabinose inducible expression of SpyCatcher-AT protein with 6x His tag
pBAD-SpyCatcher(FLAG)	pBAD33/p15a/pJ23100	Arabinose inducible expression of SpyCatcher-AT protein with FLAG tag
pKPY680	pBAD33/p15a/pJ23100	Constitutive expression of mWasabi
pKPY681	pBAD33/p15a/pJ23100	Constitutive expression of mCherry

Table S2.2: Protein sequences

Protein	Sequence
E6-AT	<p>MKYLLPTAAAGLLLLAAQPAMAMRGSHHHHHH GSVDVPGAGVPGAGVPGEGVPGAGVPGAGVPGA GVPGAGVPGEGVPGAGVPGAGVPGAGVPGAGVPG GEGVPGAGVPGAGLDVPGAGVPGAGVPGEGVPG AGVPGAGVPGAGVPGAGVPGEGVPGAGVPGAGV PGAGVPGAGVPGEGVPGAGVPGAGLETPTPGPD LNVNDLRPEAGSYIANLAAANTMFTTRLHERLGN TYYTDMVTGEQKQTTMWMRHEGGHMKWRDGS GQLKTQSNRYVLQLGGDVAQWSQNGSDRWHVG VMAGYGNSDSKTISSRTGYRAKASVNGYSTGLYA TWYADDESNGAYLDSWAQYSWFDNTVKGDDL QSESYKSKGFTASLEAGYKHKLAEFNGSQGTRNE WYVQPQAQVTWMGVKADKHRESNGTLVHSNGD GNVQTRLGVKTWLKSHHKMDDGKSREFQPFVEV NWLHNSKDFSTSMGVSVTQDGARNIAEIKTGVE GQLNANLNVWGNVGVQVADRGYNDTSAMVGIK WQF</p>
STE3-AT	<p>MKYLLPTAAAGLLLLAAQPAMAMRGSHHHHHH GSVDAHIVMVDAYKPTKLDVPGAGVPGAGVPGE GVPGAGVPGAGVPGAGVPGAGVPGEGVPGAGVPG GAGVPGAGVPGAGVPGEGVPGAGVPGAGLETP TPGPDNLNVNDLRPEAGSYIANLAAANTMFTTRLH ERLGNTTYYTDMVTGEQKQTTMWMRHEGGHMK WRDGSQQLKTQSNRYVLQLGGDVAQWSQNGSD RWHVGVMAGYGNSDSKTISSRTGYRAKASVNGY STGLYATWYADDESNGAYLDSWAQYSWFDNT VKGDDLQSESYKSKGFTASLEAGYKHKLAEFNGS QGTRNEWYVQPQAQVTWMGVKADKHRESNGTL VHSNGDGNVQTRLGVKTWLKSHHKMDDGKSRE FQPFVEVNWLHNSKDFSTSMGVSVTQDGARNIA EIKTGVEGQLNANLNVWGNVGVQVADRGYNDTS AMVGIKWQF</p>
STE6-AT	<p>MKYLLPTAAAGLLLLAAQPAMAMRGSHHHHHH GSVDAHIVMVDAYKPTKLDVPGAGVPGAGVPGE GVPGAGVPGAGVPGAGVPGAGVPGEGVPGAGVPG GAGVPGAGVPGAGVPGEGVPGAGVPGAGLDVPG AGVPGAGVPGEGVPGAGVPGAGVPGAGVPGAGV PGEGVPGAGVPGAGVPGAGVPGAGVPGEGVPGA GVPGAGLETPTPGPDNLNVNDLRPEAGSYIANLA AANTMFTTRLHERLGN TYYTDMVTGEQKQTTM WMRHEGGHMKWRDGSQQLKTQSNRYVLQLGGD VAQWSQNGSDRWHVGVMAGYGNSDSKTISSRTG YRAKASVNGYSTGLYATWYADDESNGAYLDS WAQYSWFDNTVKGDDLQSESYKSKGFTASLEAG YKHKLAEFNGSQGTRNEWYVQPQAQVTWMGVK ADKHRESNGTLVHSNGDGNVQTRLGVKTWLKSH HKMDDGKSREFQPFVEVNWLHNSKDFSTSMGVS</p>

	SVTQDGARNIAEIKTGVEGQLNANLNVWGNVGV QVADRGYNDTSAMVGIKWQF
STE9-AT	MKYLLPTAAAGLLLLAAQPA MAMRGS HHHHHH GSVD AHIVMVDAYKPTKLD VPGAGVPGAGVPGE GVPGAGVPGAGVPGAGVPGAGVPGEGVPGAGVP GAGVPGAGVPGAGVPGEGVPGAGVPGAGLDVPG AGVPGAGVPGEGVPGAGVPGAGVPGAGVPGAGV PGEVPGAGVPGAGVPGAGVPGAGVPGAGVPGAG GVPGAGLDVPGAGVPGAGVPGEGVPGAGVPGAG VPGAGVPGAGVPGEGVPGAGVPGAGVPGAGVPG AGVPGEGVPGAGVPGAGLETPTPGPD LNVDNDR PEAGSYIANLAAANTMFTTRLHERLGNTYYTDMV TGEQKQTTMWMRHEGGHKNWRDGSGLKTQSN RYVLQLGGDVAQWSQNGSDRWHVGV MAGYGN SDSKTISSRTGYRAKASVNGYSTGLYATWYADDE SRNGAYLDSWAQYSWFDNTVKGDDLQSESYKSK GFTASLEAGYKHKLAEFNGSQGTRNEWYVQPQA QVTWGMGVKADKHRESNGTLVHSNGDGNVQTRL GVKTWLKSHHKMDDGKSREFQPFVEVNWLHNS KDFSTSMGVSVTQDGARNIAEIKTGVEGQLNAN LNVWGNVGVQVADRGYNDTSAMVGIKWQF
STE12-AT	MKYLLPTAAAGLLLLAAQPA MAMRGS HHHHHH GSVD AHIVMVDAYKPTKLD VPGAGVPGAGVPGE GVPGAGVPGAGVPGAGVPGAGVPGEGVPGAGVP GAGVPGAGVPGAGVPGEGVPGAGVPGAGLDVPG AGVPGAGVPGEGVPGAGVPGAGVPGAGVPGAGV PGEVPGAGVPGAGVPGAGVPGAGVPGAGVPGAG GVPGAGLDVPGAGVPGAGVPGEGVPGAGVPGAG VPGAGVPGAGVPGEGVPGAGVPGAGVPGAGVPG AGVPGEGVPGAGVPGAGLDVPGAGVPGAGVPGE GVPGAGVPGAGVPGAGVPGAGVPGEGVPGAGVP GAGVPGAGVPGAGVPGEGVPGAGVPGAGLETP TPGPD LNVDNDRPEAGSYIANLAAANTMFTTRLH ERLGNTYYTDMVTGEQKQTTMWMRHEGGHKN WRDGSGLKTQSNRYVLQLGGDVAQWSQNGSD RWHVGV MAGYGNSDSKTISSRTGYRAKASVNGY STGLYATWYADDES RNNGAYLDSWAQYSWFDNT VKGDDLQSESYKSKGFTASLEAGYKHKLAEFNGS QGTRNEWYVQPQAQVTWGMGVKADKHRESNGTL VHSNGDGNVQTRLGVKTWLKSHHKMDDGKSRE FQPFVEVNWLHNSKDFSTSMGVSVTQDGARNIA EIKTGVEGQLNANLNVWGNVGVQVADRGYNDTS AMVGIKWQF
SpyCatcher-AT	MKYLLPTAAAGLLLLAAQPA MAMRGS HHHHHH GSVD GAMVDTL SGLSSEQQSGDMTIEEDSATHI KFSKRDEDGKELAGATMELRDSSGKTISTWISDG QVKDFYLYPGKYTFVETAAPDGYEVATAITFTVN EQGQVTVNGKATKGDAHIDLETPTPGPD LNVDND LRPEAGSYIANLAAANTMFTTRLHERLGNTYYTD MVTGEQKQTTMWMRHEGGHKNWRDGSGLKT

	<p>QSNRYVLQLGGDVAQWSQNGSDRWHVGV MAG YGNSDSKTISSRTGYRAKASVNGYSTGLYATWYA DDESRNGAYLDSWAQYSWFDNTVKGDDLQSESY KSKGFTASLEAGYKHKLAEFNGSQGTRNEWYVQ PQAQVTWMGVKADKHRESNGTLVHSNGDGNVQ TRLGVKTWLKSHHKMDDGKSREFQPFVEVNWLH NSKDFSTSMDGVSVTQDGARNIAEIKTGVEGQLN ANLNVWGNVGVQVADRGYNDTSAMVGIKWQF</p>
(FLAG)SpyCatcher-AT	<p>MKYLLPTAAAGLLLLAAQPAMAMRGSSDYKDDD DKGSVDGAMVDTLSGLSSEQGQSGDMTIEEDSAT HIKFSKRDEDGKELAGATMELRDSSGKTISTWISD GQVKDFLYLPGKYTFVETAAPDGYEVATAITFTV NEQGQVTVNGKATKGAHIDLETPTPGPDLNVDN DLRPEAGSYIANLAAANTMFTTRLHERLGNTYYT DMVTGEQKQTTMWMRHEGGHKNKWRDGSQGLK TQSNRYVLQLGGDVAQWSQNGSDRWHVGV MAG YGNSDSKTISSRTGYRAKASVNGYSTGLYATWYA DDESRNGAYLDSWAQYSWFDNTVKGDDLQSESY KSKGFTASLEAGYKHKLAEFNGSQGTRNEWYVQ PQAQVTWMGVKADKHRESNGTLVHSNGDGNVQ TRLGVKTWLKSHHKMDDGKSREFQPFVEVNWLH NSKDFSTSMDGVSVTQDGARNIAEIKTGVEGQLN ANLNVWGNVGVQVADRGYNDTSAMVGIKWQF</p>
AT	<p>MKYLLPTAAAGLLLLAAQPAMAMRGSHHHHHH GSVETPTPGPDLNVDNDLRPEAGSYIANLAAANT MFTTRLHERLGNTYYTDMVTGEQKQTTMWMRH EGGHKNKWRDGSQGLKTQSNRYVLQLGGDVAQW SQNGSDRWHVGV MAGYGNDSKTISSRTGYRAK ASVNGYSTGLYATWYADDESRNGAYLDSWAQY SWFDNTVKGDDLQSESYKSKGFTASLEAGYKHK LAEFNGSQGTRNEWYVQPQAQVTWMGVKADKH RESNGTLVHSNGDGNVQTRLGVKTWLKSHHKM DDGKSREFQPFVEVNWLHNSKDFSTSMDGVSVT QDGARNIAEIKTGVEGQLNANLNVWGNVGVQVA DRGYNDTSAMVGIKWQF</p>
Xten-AT	<p>MKYLLPTAAAGLLLLAAQPAMAMRGSHHHHHH GSVDGSPAGSPTSTEEGTSESATPESGPGTSTEPSE GSAPGSPAGSPTSTEEGTSTEPSEGSAPGTSTEPSE GSAPGTSESATPESGPGSEPATSGSETPGSEPATSG SETPGSPAGSPTSTEEGTSESATPESGPGTSTEPSEG SAPLETPTPGPDLNVDNDLRPEAGSYIANLAAANT MFTTRLHERLGNTYYTDMVTGEQKQTTMWMRH EGGHKNKWRDGSQGLKTQSNRYVLQLGGDVAQW SQNGSDRWHVGV MAGYGNDSKTISSRTGYRAK ASVNGYSTGLYATWYADDESRNGAYLDSWAQY SWFDNTVKGDDLQSESYKSKGFTASLEAGYKHK LAEFNGSQGTRNEWYVQPQAQVTWMGVKADKH RESNGTLVHSNGDGNVQTRLGVKTWLKSHHKM DDGKSREFQPFVEVNWLHNSKDFSTSMDGVSVT</p>

	QDGARNIAEIKTGVEGQLNANLNVWGNVGVQVA DRGYNDTSAMVGIKWQF
AE6-AT	MKYLPTAAAGLLLLAAQPA MAMRGS HHHHHH GSVDGSGSGSGSGSGASG DLENEVAQLEREVRS EDEAAELEQKVSRLKNEIEDLKAE GSGSGSGSGSG ALDVPGAGVPGAGVPGEGVPGAGVPGAGVPGAG VPGAGVPGEGVPGAGVPGAGVPGAGVPGAGVPG EGVPGAGVPGAGLDVPGAGVPGAGVPGEGVPGA GVPGAGVPGAGVPGAGVPGEGVPGAGVPGAGVPG GAGVPGAGVPGEGVPGAGVPGAGLE TPTGPDLN VDNDLRPEAGSYIANLAAANTMFTTRLHERLGNT YYTDMVTGEQKQTTMWMRHEGGHKNKWRDGS QLKTQSNRYVLQLGGDVAQWSQNGSDRWHVGV MAGYGNSDSKTISSRTGYRAKASVNGYSTGLYAT WYADDES RNGAYLDSWAQYSWFDNTVKGDDLQ SESYKSKGFTASLEAGYKHKLAEFNGSQGTRNEW YVQPQAQVTWMGVKADKHRESNGTLVHSNGDG NVQTRLGVKTWLKSHHKMDDGKSREFQPFEVN WLHNSKDFSTSMGVSVTQDGARNIAEIKTGVEG QLNANLNVWGNVGVQVADRGYNDTSAMVGIKW QF

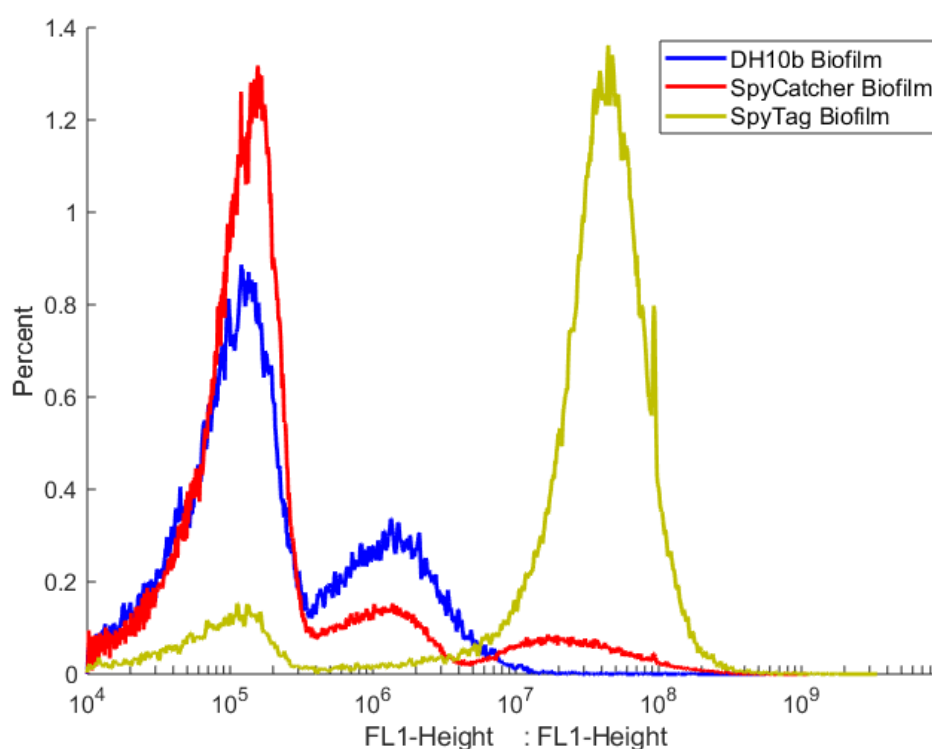


Figure S2.1, Flow cytometry data illustrating expression level of SpyTagE6-AT and SpyCatcher-AT in bacterial films. The DH10B biofilm is the negative control that should not have surface protein expression. From this diagram, we can tell that SpyTagE6-AT proteins encoded in pQE80 plasmids are constitutively expressed when grown in bacterial films. SpyCatcher-AT on the other hand is not expressing as strongly as SpyTagE6-AT but has higher expression compared to control as there is a small population with high protein expression.

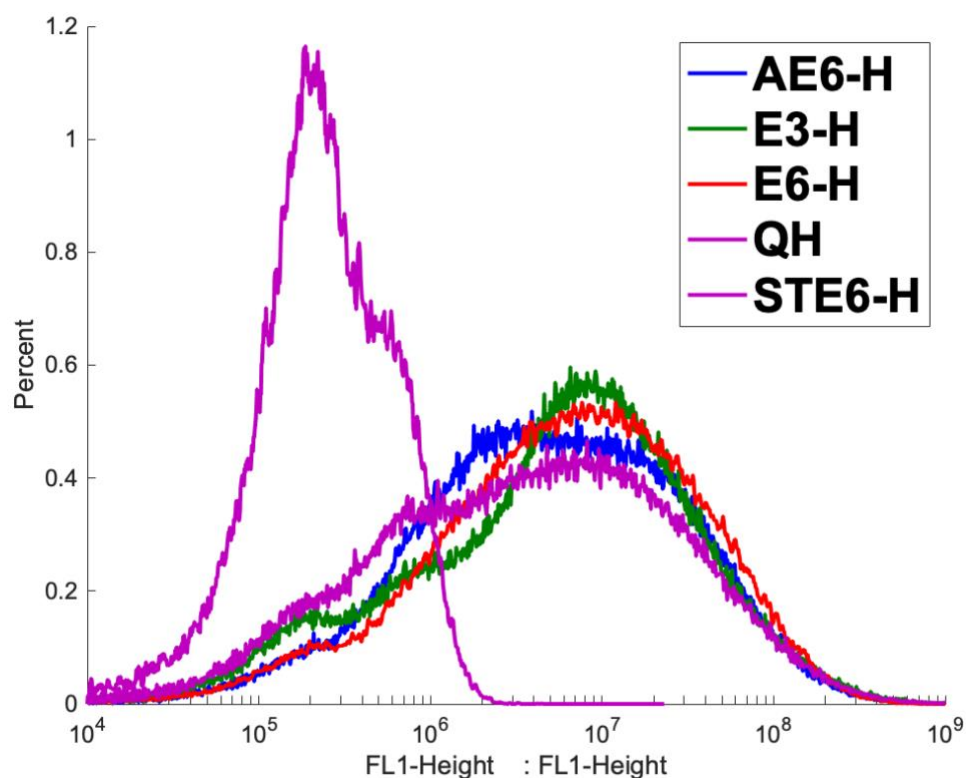


Figure S2.2, Flow cytometry data showing constitutive expression of multiple kinds of proteins. Q stands for empty pQE80 plasmid, which is the negative control group in this diagram. H stands for anti-6x His tag antibody. This diagram showed that apart from SpyTagE6-AT (STE6), AE6-AT, E6-AT and E3-AT are constitutively expressed when encoded in pQE80 plasmid in a cell in bacterial film. The expression levels of these proteins are similar.

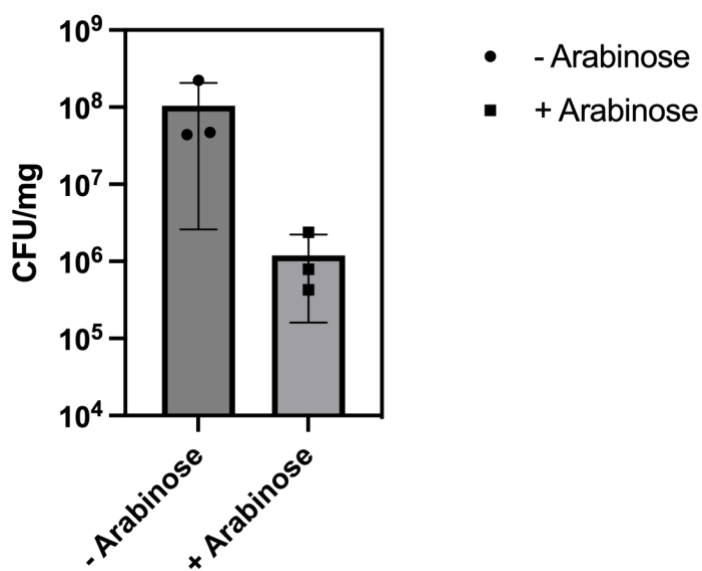


Figure S2.3, Colony forming units (CFU) per unit mass, pQE80 STE6-AT & pBAD33 SC-AT films with or without 0.1 % arabinose induction.

8. Reference

1. Gilbert, C. & Ellis, T. Biological Engineered Living Materials: Growing Functional Materials with Genetically Programmable Properties. *ACS Synth. Biol.* **8**, 1–15 (2019).
2. Nguyen, P. Q., Courchesne, N.-M. D., Duraj-Thatte, A., Praveschotinunt, P. & Joshi, N. S. Engineered Living Materials: Prospects and Challenges for Using Biological Systems to Direct the Assembly of Smart Materials. *Adv. Mater. Deerfield Beach Fla* **30**, e1704847 (2018).
3. Srubar, W. V. Engineered Living Materials: Taxonomies and Emerging Trends. *Trends Biotechnol.* **39**, 574–583 (2021).
4. Flemming, H.-C. & Wingender, J. The biofilm matrix. *Nat. Rev. Microbiol.* **8**, 623–633 (2010).
5. Flemming, H.-C. *et al.* Biofilms: an emergent form of bacterial life. *Nat. Rev. Microbiol.* **14**, 563–575 (2016).
6. Nguyen, P. Q., Botyanszki, Z., Tay, P. K. R. & Joshi, N. S. Programmable biofilm-based materials from engineered curli nanofibres. *Nat. Commun.* **5**, 4945 (2014).
7. Chen, A. Y. *et al.* Synthesis and patterning of tunable multiscale materials with engineered cells. *Nat. Mater.* **13**, 515–523 (2014).
8. Gilbert, C. *et al.* Living materials with programmable functionalities grown from engineered microbial co-cultures. *Nat. Mater.* **20**, 691–700 (2021).
9. Chen, B. *et al.* Programmable living assembly of materials by bacterial adhesion. *Nat. Chem. Biol.* **18**, 289–294 (2022).
10. Molinari, S. *et al.* A de novo matrix for macroscopic living materials from bacteria. *Nat. Commun.* **13**, 5544 (2022).

11. González, L. M., Mukhitov, N. & Voigt, C. A. Resilient living materials built by printing bacterial spores. *Nat. Chem. Biol.* **16**, 126–133 (2020).
12. Jo, H. & Sim, S. Programmable Living Materials Constructed with the Dynamic Covalent Interface between Synthetic Polymers and Engineered *B. subtilis*. *ACS Appl. Mater. Interfaces* **14**, 20729–20738 (2022).
13. Peterson, S. B. *et al.* Different Methods for Culturing Biofilms In Vitro. in *Biofilm Infections* (eds. Bjarnsholt, T., Jensen, P. Ø., Moser, C. & Høiby, N.) 251–266 (Springer, 2011). doi:10.1007/978-1-4419-6084-9_15.
14. Bertani, G. Lysogeny at Mid-Twentieth Century: P1, P2, and Other Experimental Systems. *J. Bacteriol.* **186**, 595–600 (2004).
15. Kozlowski, M. T., Silverman, B. R., Johnstone, C. P. & Tirrell, D. A. Genetically Programmable Microbial Assembly. *ACS Synth. Biol.* **10**, 1351–1359 (2021).
16. Zakeri, B. & Howarth, M. Spontaneous Intermolecular Amide Bond Formation between Side Chains for Irreversible Peptide Targeting. *J. Am. Chem. Soc.* **132**, 4526–4527 (2010).
17. Zakeri, B. *et al.* Peptide tag forming a rapid covalent bond to a protein, through engineering a bacterial adhesin. *Proc. Natl. Acad. Sci.* **109**, E690–E697 (2012).
18. Sun, F., Zhang, W.-B., Mahdavi, A., Arnold, F. H. & Tirrell, D. A. Synthesis of bioactive protein hydrogels by genetically encoded SpyTag-SpyCatcher chemistry. *Proc. Natl. Acad. Sci.* **111**, 11269–11274 (2014).
19. Dooling, L. J. & Tirrell, D. A. Engineering the Dynamic Properties of Protein Networks through Sequence Variation. *ACS Cent. Sci.* **2**, 812–819 (2016).
20. Rapp, P. B. *et al.* Analysis and Control of Chain Mobility in Protein Hydrogels. *J. Am. Chem. Soc.* **139**, 3796–3804 (2017).

21. Wells, T. J. *et al.* EhaA is a novel autotransporter protein of enterohemorrhagic *Escherichia coli* O157:H7 that contributes to adhesion and biofilm formation. *Environ. Microbiol.* **10**, 589–604 (2008).
22. Haeckel, A., Appler, F., Ariza de Schellenberger, A. & Schellenberger, E. XTEN as Biological Alternative to PEGylation Allows Complete Expression of a Protease-Activatable Killin-Based Cytostatic. *PLoS ONE* **11**, e0157193 (2016).
23. Ding, S. *et al.* Multivalent Antiviral XTEN–Peptide Conjugates with Long in Vivo Half-Life and Enhanced Solubility. *Bioconjug. Chem.* **25**, 1351–1359 (2014).
24. Podust, V. N. *et al.* Extension of in vivo half-life of biologically active molecules by XTEN protein polymers. *J. Control. Release Off. J. Control. Release Soc.* **240**, 52–66 (2016).
25. Liu, J. *et al.* A seven-helix coiled coil. *Proc. Natl. Acad. Sci. U. S. A.* **103**, 15457–15462 (2006).
26. Shen, W., Zhang, K., Kornfield, J. A. & Tirrell, D. A. Tuning the erosion rate of artificial protein hydrogels through control of network topology. *Nat. Mater.* **5**, 153–158 (2006).
27. Glass, D. S. & Riedel-Kruse, I. H. A Synthetic Bacterial Cell-Cell Adhesion Toolbox for Programming Multicellular Morphologies and Patterns. *Cell* **174**, 649–658.e16 (2018).
28. Marín, E., Bodelón, G. & Fernández, L. Á. Comparative analysis of the biochemical and functional properties of C-terminal domains of autotransporters. *J. Bacteriol.* **192**, 5588–5602 (2010).
29. NEBaseChanger. <https://nebasechanger.neb.com/>.
30. Obana, M., Silverman, B. R. & Tirrell, D. A. Protein-Mediated Colloidal Assembly. *J. Am. Chem. Soc.* **139**, 14251–14256 (2017).

Chapter 3

Cohesive Living Bacterial Films with Tunable Mechanical Properties from Cell Surface Protein Display

1. Abstract

Engineered living materials constitute a novel class of functional materials made from living organisms whose properties and functions can be programmed genetically. In this chapter, we discuss the use of a protein surface display system to engineer bacterial cells into particles bearing adhesive coatings made of artificial unstructured proteins. Engineered bacteria can grow into cohesive thin films on perforated solid supports that provide access to nutrition as cells proliferate. Mechanical properties of such bacterial films were measured using hydraulic bulge tests with “ramp” and “oscillatory” pressure profiles. From ramp bulge tests, we found that bacterial films displaying an elastin-like-peptide with a single cysteine were non-yielding under our test conditions and had Young’s moduli around 44 kPa, while films displaying only the elastin-like peptide yield at a strain around 0.11 and had Young’s moduli around 14 kPa. Disulfide bond formation and its crucial role in enhancing mechanical strength of cysteine-expressing bacterial films were confirmed by treating films with the reducing agent TCEP. Oscillatory bulge tests revealed viscoplasticity of elastin expressing films and viscoelasticity of elastin expressing films with terminal cysteines. These bacterial films can also self-heal in a day after defect creation with their Young’s moduli fully restored and toughness partly restored. This work established an approach to produce genetically programmable, self-healable bacterial-based living materials that have potential in biomanufacturing, construction and bioremediation.

2.Introduction

In nature, microorganisms including bacteria can autonomously assemble into hierarchical structures called biofilms,¹ composed in part of living cells that can sense environmental stress² and catalyze reactions,^{3,4} and in part of extracellular polymeric matrices (EPS)⁵ that are secreted by cells and composed of proteins, lipids, polysaccharides and nucleic acids.⁶ These polymeric matrices protect bacteria and create microenvironments that help bacteria survive.⁷ Inspired by natural biofilms, the field of engineered living materials lies at the interface between materials science and synthetic biology. Through manipulation of genetic information, organisms can be directed to assemble into materials that possess desirable characteristics of living systems, such as autonomous assembly, adaptiveness to environmental stimuli and self-healing.⁸⁻¹² Recently, several biofilm-inspired living materials have reported, in which researchers either rewired the original biopolymer synthetic pathways like curli fibrils^{13,14} or cellulose^{15,16}, or encapsulated living bacteria in synthetic polymeric matrix.^{17,18} These approaches have certain limits. For example, the curli secretion system is sensitive to the size of proteins and peptides fused with curli protein monomers which limits the size of functional moieties that decorate the curli fibrils,^{19,20} and cellulose producing bacteria require an oxygen-rich air-water interface for efficient cellulose synthesis.^{21,22} Encapsulating bacteria in synthetic polymer networks has drawbacks with respect to sustainability, as synthetic polymers are not produced by bacteria. These systems thus cannot self-heal through secretion from living cells.

Matrix-free approaches to living materials utilizing cell-cell adhesion have recently received much attention. In such systems, modified bacteria express associative proteins at the cell surface, forming cell aggregates. This approach requires neither

matrix secretion nor synthetic polymers, and living materials in principle can be generated from a single cell. One reported cell adhesion mediated living material utilizes “nanobody-antigen” interactions in *E. coli*;^{23,24} another is based on engineering *C. crescentus* rsaA protein²⁵. These two methods, however, still have limitations. For “nanobody-antigen” method, two kinds of cells, one expressing nanobodies and one expressing antigen are required, and only when the two kinds of cells are mixed together at 1:1 ratio does the material have desirable mechanical properties. Furthermore, the proteins used in this work are natural antibodies and antigens with complex protein structures. In the *C. crescentus* system, the rsaA protein is not anchored in the cell membrane but binds to the saccharide coating on the surface of *C. crescentus*.²⁶ This means that the protein must be secreted from the cell and then bind to the glyco-coating of bacterium. Both methods both require the material to be grown in liquid culture media and then collected and assembled into cm-scale structures.

Here we describe a novel method to grow cm-scale bacterial films on perforated membrane filters. Using a previously developed protein surface display system, we engineered *E. coli* to surface display unstructured elastin-like-peptides of 150 amino acid in length. We found that these peptides were adhesive enough to generate cohesive bacterial films that can be tested for mechanical properties measurements. Furthermore, we placed a single cysteine at the exposed N-terminal end of elastin and introduction of this single cysteine drastically improved the mechanical performance of bacterial films by forming intercellular disulfide bonds covalent crosslinks. The bacterial films with disulfide covalent intercellular interactions behaves non-yielding upon deformation, endure multiple pressure loading cycles without permanent deformation and can self-heal rapidly within a day with Young’s modulus fully recovered.

3.Results and Discussion

3.1 Design of surface displayed protein and growing of bacterial films

To make cohesive bacterial films, we expressed two different kinds of associative proteins on the *E. coli* surface using an “autodisplay system” previously reported to display a wide variety of proteins including enzymes and vaccine epitopes²⁷⁻³⁰ and used by our laboratory to generate bacterial aggregates in planktonic culture.³¹ We used the autotransporter system to display unstructured elastin-like-peptides with or without N-terminal cysteines at the cell surface to control the mechanical properties of bacterial films.

Illustrations of the cells used in this work to generate bacterial films, sequences of the surface-displayed proteins, and the types of intercellular adhesion are shown in **Fig 3.1a**. The expression constructs are shown in **Fig S3.1**. In each construct, the target associative domain is fused to a 6xHis tag (for immunostaining) and inserted between a PelB secretion sequence and the autotransporter. The elastin-like-peptide (E) domain was previously used in our laboratory to prepare protein based hydrogels³²⁻³⁴ and as a spacer in surface-displayed proteins that drive formation of cellular aggregates.³¹ Since we use 6 repeats of a 25-amino acid elastin-like peptide, we refer to this construct as E6-AT (with AT representing the autotransporter). The CE6-AT construct differs from E6-AT by a single amino acid, with cysteine placed between the 6xHis tag and the elastin-like-peptide. The goal of introducing cysteine into the displayed protein was to generate intercellular covalent disulfide bonds as crosslinks and thus enhance the mechanical strength of the bacterial films generated. These surface-displayed proteins were encoded in a pQE80 plasmid backbone under control of a T5-lac promoter. In the

DH10B cells used in this work, the T5-lac promoter drives constitutive expression of surface displayed protein; no IPTG inducer is required.

The method of coating and growing bacterial films is shown in **Fig 3.1b**. As described in Chapter 2, 200 μL of an overnight bacterial culture grown from a single colony on an agar plate was pipetted onto a 2.5 cm diameter polycarbonate membrane filter with 0.2 μm pore size. Vacuum filtration was applied to remove the liquid media and leave bacteria as a coating on top of the membrane filter. The filter was then transferred onto an LB agar plate, which provides nutrition for bacterial film growth and antibiotics to maintain the plasmid. Nutrition was replenished by transferring the filter to a fresh LB agar plate every day. After 7 days of growth, bacterial films were ready to be tested.

To ensure that films would remain cohesive in the buffer used for mechanical testing, we applied the erosion assay described in Chapter 2. A 7 day-old bacterial film was immersed in 7 ml of PBS buffer and placed on a rocking platform with shaking. The optical density (OD_{600}) of the buffer was measured at 1 h and 24 h. After 1 h of erosion in PBS, control films without surface protein expression reached an OD_{600} value above 0.1 while for both E6-AT and CE6-AT OD_{600} remained below 0.001. After 24 h of erosion, the OD_{600} of the control increased to values greater than 0.3 and the film disintegrated. In contrast, E6-AT and CE6-AT films remained intact and OD_{600} of the buffer was still below 0.01 (**Fig S3.2**). These results suggested that films made from cells with E6 and CE6 surface display were cohesive and could be tested for mechanical properties.

To understand the structure of these bacterial films at microscale, we introduced another plasmid that drove constitutive expression of fluorescent proteins in the cell.

Fig 3.1c shows a the microtome cross-sectional view of a 7 day-old CE6-AT film that expresses the fluorescent protein mWasabi. From the image, it is clear that 7 day-old CE6 films have reached a thickness of approximately 70 μm and contain densely packed bacterial particles . To ensure that proteins are in fact displayed at the bacterial surface in these films, we stained microtome sections of CE6-AT films with anti-His tag antibody conjugated to Dylight-488 fluorophore; the resulting image is shown in **Fig 3.1d**. The film shows evidence of staining across the full thickness. The reconstructed 3D image of the antibody-stained microtome section also showed reasonably uniform expression of protein throughout the sample (**Fig S3.3**). In the enlarged view of cells in the lower left corner of the image, we see evidence of antibodies surrounding the cell body and forming a ring. These images suggest that we have expression of His-tagged protein at the cell surface, consistent with the expected surface display of CE6-AT in the bacterial films. Similar experiments and flow cytometry using anti-His tag fluorescent antibody staining were applied to E6-AT films, with results shown in **Fig S3.4&5**. We also used live/dead staining to determine if there significant numbers of dead cells in the interior of the film where oxygen diffusion might be limited. The results showed that living cells and dead cells are distributed relative uniformly across the full thickness for E6-AT films. In CE6-AT films we detected a thin layer with more evidence of dead cells about 60 μm below the film surface (**Fig S3.6**). From these results, we are confident that E6-AT and CE6-AT bacterial films are characterized by expression across the full film thickness are cohesive thin films made of cells packed with each other densely.

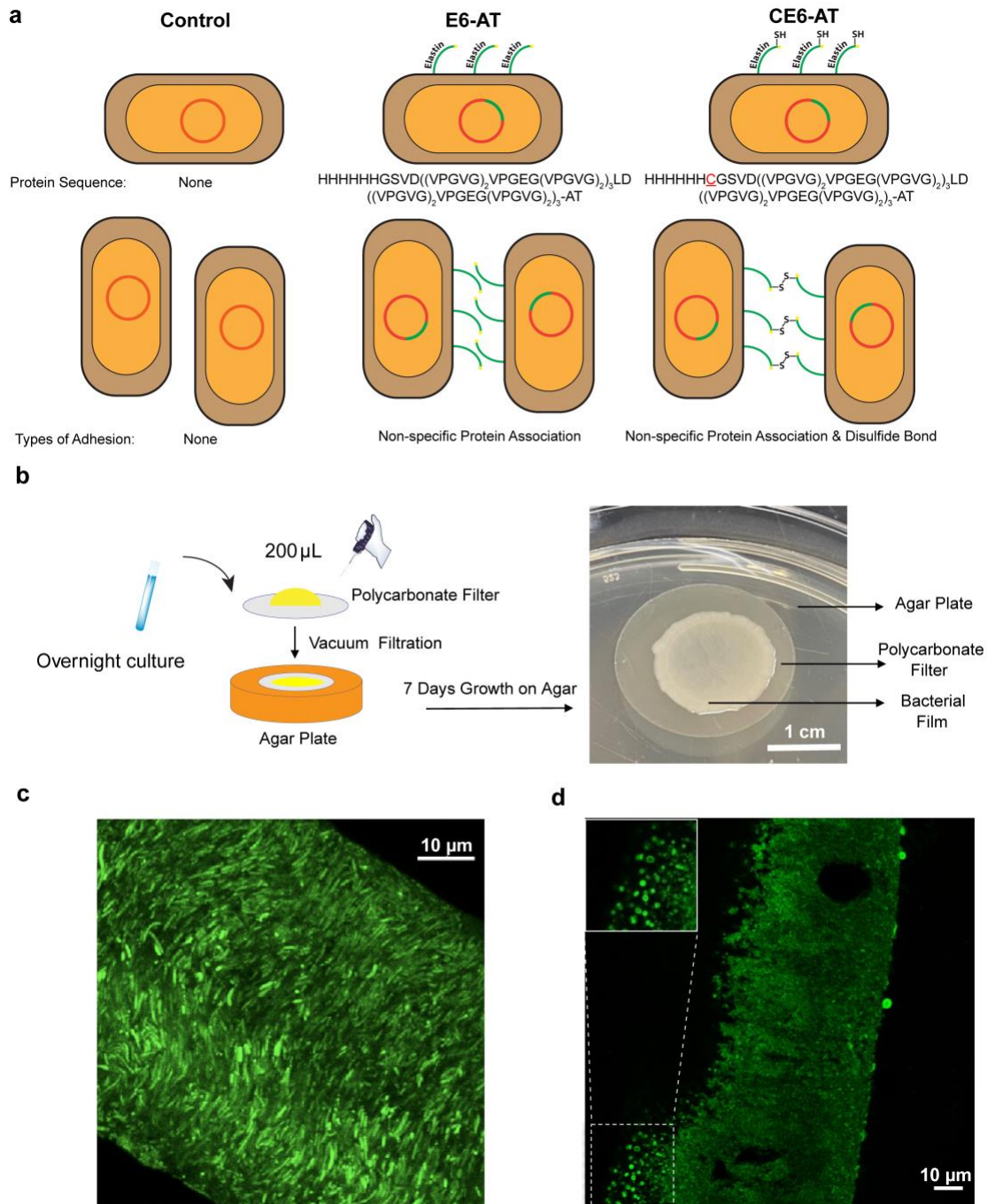


Figure 3.1. Cohesive living bacterial film made of engineered bacterium. **a**, Schematics of engineered *E. coli* cells used as building blocks of living materials in this work. Schemes of engineered bacteria, protein sequences and types of intercellular adhesions. **b**, Schematics of suction coating method of bacterial film preparation. Overnight planktonic culture of bacteria of interest was pipetted onto a perforated polycarbonate filter with 0.2 µm diameter pore size. Vacuum filtration was applied to remove liquid media and retain bacteria on top of the filter. The filter with bacteria coating was then transferred to an agar plate and allowed to grow for 7 days. A image of 7 day old mature CE6-AT bacterial film on polycarbonate filter on LB agar plate. Scale bar, 1 cm. **c**, Microscopy image of mWasabi expressing 7 day old CE6-AT film microtome cross-section. Scale bar, 10 µm. **d**, Microscopy image of 7 day old CE6-AT film microtome cross-section immunostained by anti-His-tag antibody conjugated to Dylight-488 fluorophore. Scale bar, 10 µm. The image shown in the upper left corner is an enlargement of the dashed-square portion of the image in the lower left corner.

3.2 Measuring mechanical properties of bacterial films using ramp bulge tests

In order to measure the mechanical properties of bacterial films with different surface displayed proteins, we constructed a custom millifluidic device suitable for imposing Pa-kPa pressure differences across freely suspended bacterial film samples, equipped with an optical coherence tomography (OCT) system to quantify the resulting changes in the shape of the biofilm (**Fig 3.2 a&b**).³⁵ A 3 mm diameter bacterial film sample, punched from a 7 day old bacterial film, was sandwiched between two transmission electron microscopy (TEM) disks with 1.5 mm diameter aperture, and placed in the central chamber of the bulge test device. One vertical cylindrical hole and horizontal channel allowed “Reservoir 1” to be connected the top face of the device and control the pressure on the top face of the sample (p_1 in **Fig 3.2b**); another vertical cylindrical hole passed through the top part and connected to the horizontal channel in the lower part, allowing “Reservoir 2” to control the pressure below the sample (p_2 in **Fig 3.2b**). When the liquid level in “Reservoir 2” is higher than that in “Reservoir 1”, $p_2 > p_1$, a net pressure from below the sample will be applied and the sample will bulge upward. The deformation of the sample is imaged by optical coherence tomography (OCT) (**Fig S3.7**).

A syringe pump was used to impose a “Ramp” pressure-time profile (**Fig 3.2c**), in which PBS buffer was added at a flow rate of 70 ml/min, with a final target volume of 55 ml. The rate of pressure increase in this pressure-time profile is 20.4 Pa/s. Since we know the rate of pressure increment over the time, the pressure applied to the sample at any given point is known and through image analysis, the strain developed in the sample can be acquired. The relationship between stress and strain can then be calculated. The calculation method for stress developed in the material is discussed in

the Materials and Methods section and Supporting Information. Material properties can be revealed by plotting stress versus strain curves. In **Fig 3.2d**, three stress versus strain curves for CE6-AT films and three curves for E6-AT films (each curve comes from a different biological replicate) are shown. All E6-AT films were tested until failure, while the CE6-AT films didn't fail even at the maximum pressure of 960 Pa. The slopes of the stress-strain curves for CE6-AT samples are larger than those for E6-AT films, indicating that CE6-AT films have larger Young's moduli. In **Fig 3.2e**, the Young's modulus values calculated using the slopes of the stress- strain curves below strain = 0.05 are shown. The average Young's modulus of CE6-AT films is around 44.0 ± 5.6 kPa, approximately three times that of E6-AT films, which is 14 ± 2.1 kPa. Furthermore, we observe that E6-AT films yield when they reach a strain around 0.11, transitioning from elastic behavior to plastic behavior and eventually failing, while CE6-AT films showed no evidence of yielding, even when the maximum pressure was applied. The difference in the yielding behavior of E6-AT films CE6-AT films was also observed when we tried to peel films from their filter membrane supports using tweezers; E6-AT films stretch and then break like soft dough, while CE6-AT films can be peeled from the filter intact with little deformation. The only one time we observed a CE6-AT film failure was from a film accidentally left in 1xPBS buffer for 4 hours, and the failure happened abruptly when the film was still undergoing elastic deformation. Videos of OCT scanned "Ramp" bulge tests of E6-AT and CE6-AT films, peeling experiments and the only failure of an CE6-AT film (**Figure S3.8**) are shown in the attached **Supporting slide of chapter 3**.

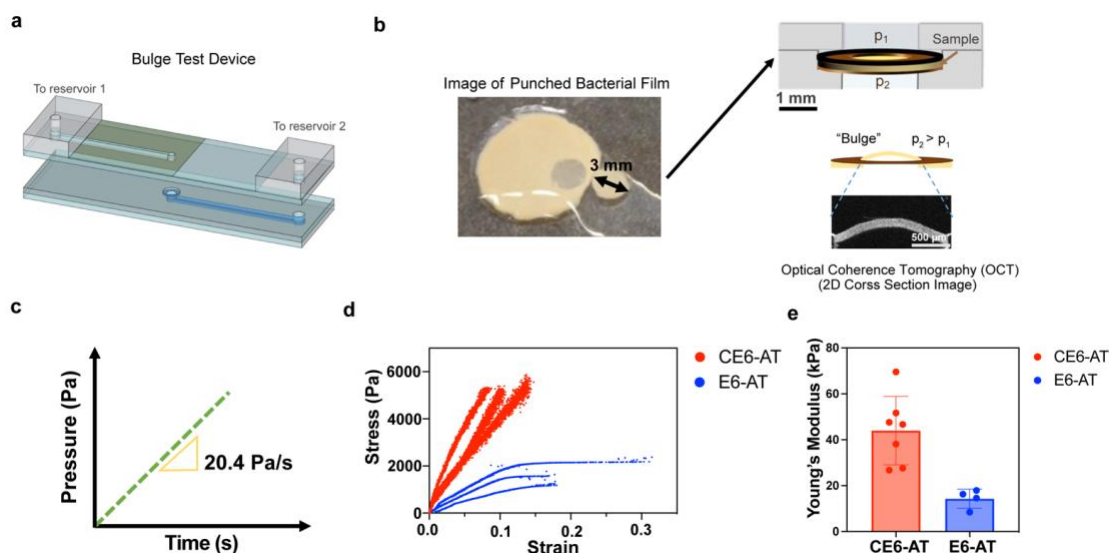


Figure 3.2. Mechanical strength of engineered bacterial films measured by ramp bulge test . **a**, Schematic of bulge test device, fabricated as two parts that are separated to load a sample in the central chamber at the center of the device; the top and bottom parts seal with vacuum grease. When loaded and sealed, port 1 connects to a reservoir of fluid that is used to control pressure on the top face of the sample (not shown); similarly, port 2 permits control of the pressure on the bottom face of the sample. Gray layers are acrylic; blue layer indicates etched channel; green thin layer is cover slip glass; layers are bonded using epoxy. Horizontal channels are longer than shown. **b**, Schematic of loading bacterial film sample onto the bulge test device and imaging of deformed film by optical coherence tomography (OCT). Punched bacterial film sample (3 mm diameter) supported by two washer-shaped disks was transferred to the central chamber of the device. A thin O-ring sealed this “sandwich” to the top half of the device. When pressure in reservoir 2 was larger than that in reservoir 1, a net pressure upward was applied to bacterial film and film bulged upward and was imaged by OCT. **c**, Pressure profile of ramp bulge test. In ramp bulge test, the pressure applied to the material increased linearly at a rate of 20.4 Pa/s. **d**, Stress versus strain curves of CE6-AT and E6-AT films. Number of curves shown for CE6-AT films: 3. Number of curves shown for E6-AT films: 3. **e**, Young’s modulus values of CE6-AT and E6-AT films. Number of replicates for CE6-AT: 7. Number of Replicates for E6-AT films: 4. Error bar is 1 standard deviation.

3.3 Disulfide bonds play an essential role in enhancing the moduli of CE6-AT films

Bulge test results showing that CE6-AT films exhibit larger Young’s moduli compared to E6-AT films support with our hypothesis that covalent disulfide bonds between cells should enhance film strength. However, measuring mechanical properties alone cannot confirm the presence or role of disulfide bonds in CE6-AT films. To probe the possibility that factors other than protein sequence caused the differences in mechanical properties between E6-AT and CE6-AT films, the water content (**Fig S3.9**), CFU per unit mass of film (**Fig S3.10**) and protein expression level (**Fig S3.11**) were all measured. These results showed that E6-AT and CE6-AT films are physiologically similar and that there is not a large difference between the expression levels of E6-AT and CE6-AT proteins.

Disulfide bonds can be reduced by multiple reducing reagents. We chose the odorless TCEP (tris(2-carboxyethyl)phosphine) to reduce and count disulfide bonds in bacterial films. Free thiols before and after reduction can react with a maleimide-fluorophore (**Fig 3.3a**). If CE6-AT forms disulfide bonds, CE6-AT films treated with TCEP should exhibit higher fluorophore labeling than either CE6-AT without TCEP treatment or E6-AT films irrespective of TCEP treatment. We used 50 mM TCEP in 20 mM HEPES buffered at pH 7.0 to react with pre-weighed films for 1 h (TCEP + group). Control films were not treated with TCEP but immersed in 20 mM HEPES buffered at pH 7.0 for 1 h (TCEP – group). TCEP-supplemented buffer was then removed and films of were treated with 50 μ M Dylight 633-maleimide in HEPES buffer at pH 7.0 for 30 min. Films were then lysed and the absorbance of the lysate at 633 nm was measured and normalized by the treated film mass. As shown in **Fig 3.3b**, CE6-AT films treated with TCEP have the highest labeling intensity among the four groups, suggesting that CE6-AT films contain the largest concentration of free thiols after reduction. Interestingly, CE6-AT and E6-AT films without TCEP treatment have similar labeling intensity. This result suggests that thiols in CE6-AT films are mostly in the oxidized (disulfide) form. However, the percentage of *intercellular* disulfide bonds cannot be determined by this method.

Using this assay, we can estimate the number of CE6-AT proteins per cell by assuming that the difference in labeling intensity between the CE6 TCEP+ group and the E6 TCEP- group is caused entirely by reduced CE6-AT proteins. The calculation method is discussed in **Supplementary Note 3.4** and **Fig S3.12** and yields an estimate of 2.5×10^5 CE6-AT proteins per cell. This result agrees with those of quantitative Western blotting (**Supplementary Note 3.5** and **Fig S3.13**), which also gives values around 2.5

* 10^5 E6-AT and CE6-AT protein per cell. Assuming the surface area of a single *E. coli* cell is $6 \mu\text{m}^2$,³⁶ the density of protein expressed is around $4 * 10^5$ proteins per μm^2 . Comparing this value to the literature, we find that a *C. crescentus* based living material²⁵ with RsaA protein fused with elastin-like-peptide displayed at a density around $1.4 * 10^5$ protein per μm^2 .³⁷⁻³⁹ This material has storage modulus of ~ 14 kPa, similar to that of E6-AT films. This result suggests that the surface display density estimated for E6-AT and CE6-AT films is reasonable.

Next we addressed the question of whether disulfide bonds are responsible for the mechanical enhancement of CE6-AT films. We treated CE6-AT and E6-AT films with 50 mM TCEP for 30 min in 20 mM HEPES buffered at pH 7.0 (TCEP +) and control films (TCEP -) in 20 mM HEPES buffered at pH 7.0 for 30 min. Ramp bulge tests were then performed on both the TCEP + and TCEP - groups in 20 mM HEPES buffered at pH 7.0. As shown in **Fig 3.3c**, the stress-strain curves of E6-AT films overlapped well irrespective of TCEP treatment, suggesting that TCEP has minimal effect on mechanical properties on E6-AT films. The Young's modulus values presented in **Fig 3.3d** also suggest that the mechanical properties of E6-AT films aren't affected by TCEP. CE6-AT films, however, are very sensitive to TCEP treatment. As shown in **Fig 3.3c**, the stress versus strain curves of TCEP-treated CE6-AT films lie far below those of the control group. As shown in **Fig 3.3d**, after treatment of CE6-AT films with 50 mM TCEP for 30 min, Young's modulus dropped from above 70 kPa to just slightly above 40 kPa. If we leave CE6-AT films in 50 mM TCEP for 1 h, they become so brittle that they can't be loaded onto the bulge test device and mechanical property characterization becomes impossible. Interestingly, even after TCEP treatment, CE6-AT films still showed no evidence of yielding or failure under the conditions used for

bulge testing. This phenomenon is consistent with the hypothesis that disulfide bond crosslinks are essential to the non-yielding behavior of CE6-AT films, and suggests that TCEP reduction is incomplete. Incomplete reduction appears to reduce the Young's modulus but as long as there are some covalent crosslinks in the bacterial film, the film remains non-yielding.

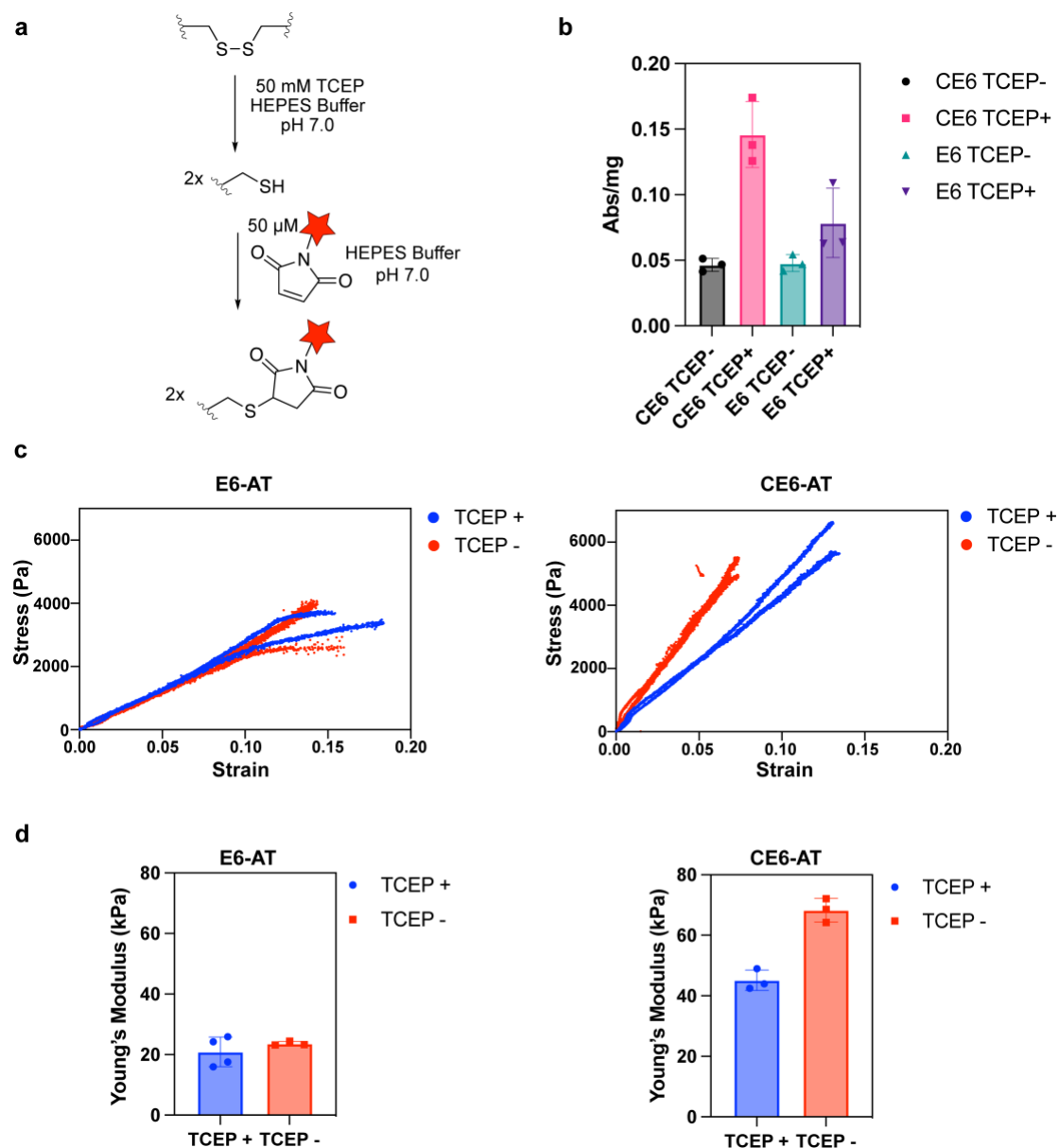


Figure 3.3. Disulfide bond plays essential role in enhanced mechanical strength of CE6-AT films. **a**, Schematic of TCEP reduction of disulfide bond and fluorophore-maleimide labeling of reduced free thiol. **b**, Labeling intensity of fluorophore-maleimide to CE6-AT and E6-AT films treated with or without TCEP. Number of replicates for each group: 3. Error bar is one standard deviation. **c**, Stress versus strain curves of E6-AT and CE6-AT films treated with or without TCEP. Number of curves shown for each group: 2. **d**, Young's modulus values of E6-AT and CE6-AT films treated with or without TCEP. Number of replicates for E6-AT TCEP + is 4 while all other groups have 3. Error bar is 1 standard deviation.

3.4 Viscoelastic behavior of bacterial films revealed by oscillatory bulge test

We investigated elasticity and changes in properties over multiple loading cycles using an oscillatory bulge test. Using the syringe pump, we were able to apply a “sawtooth” loading pattern (**Fig 3.4a**) and observe the biofilm response using OCT.

Elasticity is the ability of a material to return to its original size and shape upon removal of applied loads. A perfectly elastic material would return to its original size and shape, with either a linear or nonlinear stress-strain response that is independent of loading rate with superimposable stress-strain curves during loading and unloading. In a cyclic loading experiment, there is no phase lag between the applied stress and measured response (**Fig 3.4b Left**). A viscoelastic material, on the other hand, has both the characteristics of a solid and a fluid: properties are dependent on loading rate, with steeper response curves at faster loading rates. For a particular loading rate, the stress-strain response does not follow the same path for loading and unloading, and the area between the curves signifies energy dissipated during the process (**Fig 3.4b Middle**). Within limits, viscoelastic materials can completely regain their properties, while in (visco)plastic deformation, there is permanent deformation indicated by a non-zero x-intercept (**Fig 3.4b Right**). In a cyclic loading experiment, a perfectly viscous material would have a phase lag of 90° , while a viscoelastic material would have a phase lag between 0 and 90° (**Fig S3.14**).

The bulge test was performed with a protocol similar to that of the “ramp” method, but using a sawtooth profile (**Fig 3.4 a**). The loading rate (slope) was 70 ml/min (maximum allowable by the syringe pump), to a maximum volume of 2 ml. The acquisition time was consistent at 19 ms. OCT images were processed with MATLAB with the protocol

described in the Materials and Methods section. Inflection points were automatically detected in pressure vs. time (piecewise) plots and strain vs. time plots by identifying points with maximum change in mean and slope relative to surrounding data points, and then used to separate data points and plot information for each loading cycle.

Fig 3.4c shows strain versus time and the pressure profile for an E6-AT film. It is clear that there exists a phase lag in the very first cycle. We plot cycle 1 and cycle 3 of loading and unloading curves in the right panel. From the first loading and unloading cycle, it is apparent that E6-AT films are viscoplastic with permanent deformation observed after the first cycle. In the third cycle, the phase lag was so large that we saw strain decreasing in the beginning of pressure loading and strain increase during pressure unloading. The permanent strain deformation also increased in the third cycle compared to the first cycle. The phase lag for E6-AT is plotted in **Fig S3.15** and the first 8 cycles of loading and unloading are plotted in **Fig S.3.16**.

In **Fig 3.4d**, we show strain versus time and the pressure profile together for a CE6-AT film. The phase lag was not evident in the first cycle but became apparent in later cycles. We plot cycle 1 and cycle 3 of loading and unloading curves on the right panel. In the first loading and unloading cycle, CE6-AT films behave almost like an elastic material. However, the loading and unloading cycles did not overlap perfectly, suggesting CE6-AT is viscoelastic. After the first cycle, the strain returns to 0, implying no permanent deformation. In the third cycle, the phase lag became observable and the area enclosed by the loading and unloading curves increased. This suggests that energy dissipated in the loading and unloading cycle increased, implying CE6-AT films gradually becomes more viscous when undergoing repetitive deformation. Permanent deformation was still not observed in the third cycle but became apparent in later cycles. The permanent

deformation of CE6-AT films after 8 cycles ($= 0.0008$) is still smaller than that of E6-AT films ($= 0.003$) after first cycle. CE6-AT films are viscoelastic and the phase lag increased almost linearly with increasing cycle number. The phase lag for CE6-AT is plotted in **Fig S3.17** and the first 8 cycles of loading and unloading are plotted in **Fig S.3.18**.

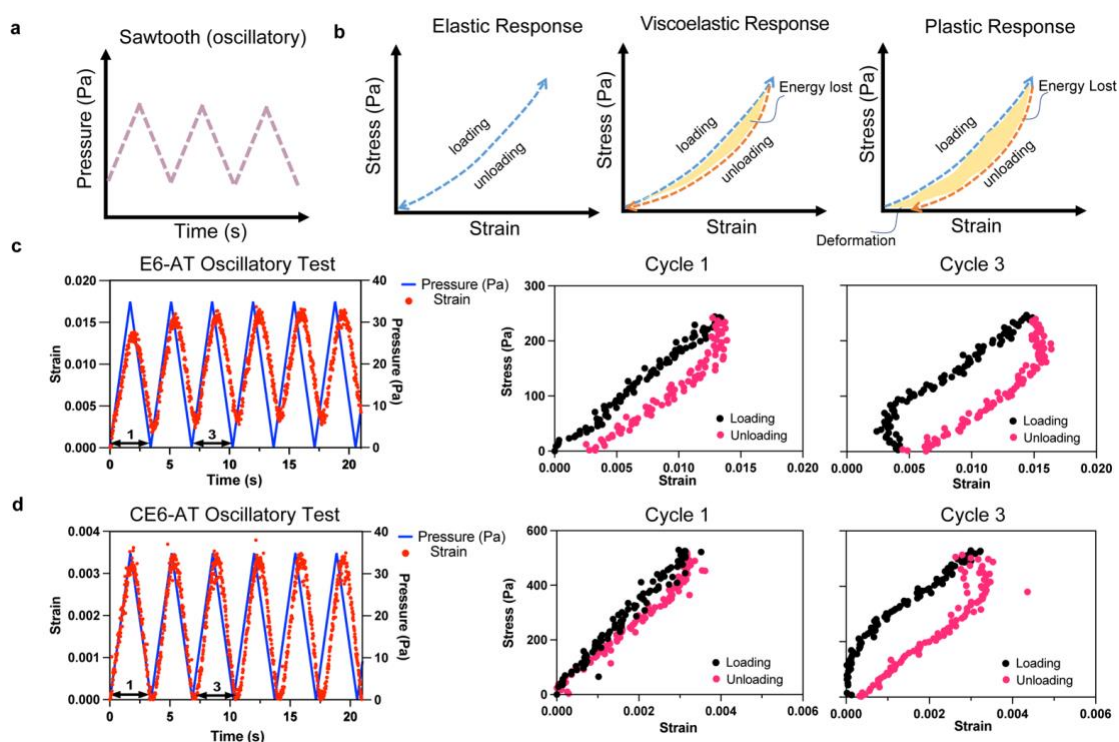


Figure 3.4. Viscoelastic behavior of bacterial films revealed by oscillatory bulge test. **a**, Pressure profile of oscillatory bulge test. **b**, Response of elastic, viscoelastic and (visco)plastic materials upon loading and unloading. **c**, Mechanical behavior of E6-AT film in oscillatory bulge test. Left: Strain versus time curve superimposed with pressure versus time curve. Cycle 1 and cycle 3 of loading were labeled by double headed arrows. Middle: Loading and unloading stress versus strain curves in the first cycle. Right: Loading and unloading stress versus strain curves in the third cycle. **d**, Mechanical behaviors of E6-AT film in oscillatory bulge test. Left: Strain versus time curve superimposed with pressure versus time curve. Cycle 1 and cycle 3 of loading were labeled by double headed arrows. Middle: Loading and unloading stress versus strain curves in the first cycle. Right: Loading and unloading stress versus strain curves in the third cycle.

3.5 CE6-AT films can heal within a day

For self-healing experiments, multiple 3 mm punches from CE6-AT films were separated from the polycarbonate as described above and then placed on a fresh 2YT plate for healing. A 25 μm thick TEM grid was used to make a cut through films. Control films were placed on fresh plates as well, without injury, for comparison. Films

were allowed to grow on the new plate at 37°C and monitored to assess the healing process. OCT imaging of the cut and control biofilms was performed at 3, 6, and 16 h (**Fig 3.5a**). In order to image comparable regions each time, we 3D printed a petri dish holder (**Fig S3.19**) and secured it to the OCT base plate, with a cavity that provided a snug fit for a single 60 mm diameter petri dish. The holder was at roughly a 10° slant to avoid noise from reflections in the OCT image at the air-biofilm interface. Only one biofilm punch was placed at the center of each petri dish, and permanent marks on both the petri dish and holder enabled alignment of the petri dishes each time they were removed from the incubator for imaging. Although the vertical focus of the OCT could necessarily not be kept constant, we reproduced the scan settings in XY using the ThorImage OCT software to ensure that the scanned region was consistent for a given punch. Alignment was further confirmed using the camera images from the ThorImage OCT software, which provided an overall view of the sample as well as the specific scan box (**Fig 3.5b**, camera image insets with red rectangular boundaries). The OCT images of healing (**Fig 3.5b**) provided a baseline for our bulge test time points. From the OCT images, the injured region showed clear healing in as little as 3 h; however the timescale of recovery of mechanical properties could only be assessed by the bulge test. Images were exported either as 3D renders at the same viewing angle and contrast (**Fig 3.5b**, top), or as 2D cross sections at the same XZ plane in each image (**Fig 3.5b**, bottom). The OCT scanned image of control films is presented in **Fig S3.20**.

We attempted to perform bulge tests at 6, 12, 16, and 24 h time points. Statistics are reported in **Table S3.3**, describing the number of samples tested at each time point along with major points of failure. We discovered that healed biofilms could easily be separated from the nutrient plate by gently flooding the plate with PBS. After

approximately 1-2 min, the punches freely separated from the agar underneath. Despite the gentle nature of this step, a few samples failed when peeled from the agar, with the previous injury reopening (second column, **Table S3.1**). The next major point of failure was during the initial pressure equilibration step (third column, **Table S3.1**). The final column in **Table S3.1** detailed whether films failed during the bulge test itself. Properties of the immediately cut biofilm are not reported, since cut films could not sustain a pressure difference (**Fig S3.20**). Fluid simply flowed through to the other side. This feature was also directly used in our experiments to determine the moment when the film failed, also visible by OCT. In comparing the various time points, we discovered that films healed for 6 h could be peeled from the agar and placed in the bulge-testing device; however the small differences in pressure resulting from filling of the device were sufficient to break the film once again. Films healed for 12 and 16 h could be readily tested. Surprisingly, none of the films tested after 24 h of healing could withstand loading, suggesting that there is an optimal time frame for recovery of mechanical properties.

Next, we assessed the extent of recovery of mechanical properties using the 16 h mark as our time point, comparing the original uncut film on day 0, the control (uninjured film grown on the healing plate), and healed films (**Fig 3.5c-e**). It is worth noting that due to the increased thickness of the control and healed films relative to the original film (123 ± 2.78 and 120 ± 15.0 vs 103 ± 11.1 μm respectively, only considering films that were successfully tested), the range of stresses that could be imposed by our device (inversely proportional to the thickness of the film) was not directly comparable. However, we did observe a few clear differences among the films tested: first, the original (uninjured, day 7) films did not fail at the maximum pressure limits imposed

by our device. The actual stress this corresponded to depended on the sample thickness and properties, but the highest observed stress tested on a CE6-AT sample of 89 μm thickness was 7.21 kPa. While there was some variation in the range of applied stresses and observed strains during our test, we observed that CE6-AT films on day 7 consistently tolerated stresses greater than 6.5 kPa (**Fig S3.20A**). In contrast, two out of four of the control films (16 h) failed during the experiment. One failed at a stress of 4.68 kPa, while the other film failed at a stress of 3.65 kPa (**Fig S3.20C**). All of the healed films that could be loaded and tested failed within the range of stresses applied in the test (**Fig S3.20D**). To probe the extent of healing of the defect, we used CE6-AT films expressing the fluorescent protein mWasabi, and observed the healing process using confocal microscopy (which has higher resolution than OCT). Confocal microscopy images (**Fig S3.21**) revealed visible defects until 16 h of healing.

As shown in **Fig 3.5c**, we observed that Young's modulus was similar across all three sets of films. Comparing bacterial films healed for 12 vs. 16 h, we found that the elastic moduli did not show a clear difference (12 h: 52.7 ± 11.4 ; 16 h: 41.4 ± 2.31 kPa). However, based on the observation that every healed biofilm that could be tested failed before the end of the test, we hypothesized that toughness might increase with healing time. We estimated toughness by calculating the area under the stress-strain plots (in **Fig 3.5d**, the shaded area represents the toughness), and discovered that the healing time did indeed influence toughness – despite substantial variability in the 16 h samples, there was a clear increase in toughness of the healed films at the latter time point (**Fig 3.5e**). Because the original films (free of defects) cannot be tested to failure, we do not know the toughness of the original films and thus cannot estimate the extent of recovery using toughness values.

Similar self-healing experiments were applied to E6-AT films; however, E6-AT films that appeared healed by OCT were too fragile for bulge-testing.

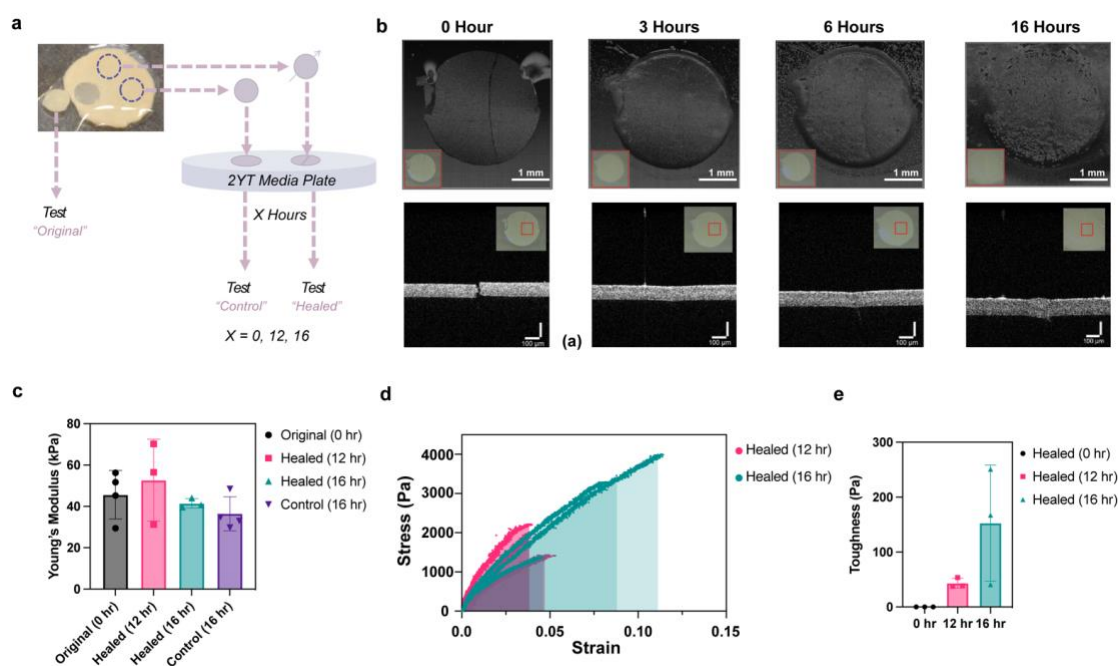


Figure 3.5. Self-healing capability of CE6-AT films. **a**, Schematic of bacterial film healing experiment. **b**, OCT scans of CE6-AT films healing on 2YT plate show rapid healing of injured bacterial film. Top row exported as 3D renders. Scale: top, 4 x 4 mm scan box; bottom, 1 x 1 x 1 mm scan box. Insets are OCT camera images, manually cropped to region being scanned. Red rectangular outline represents scan box. **c**, Young's modulus values of original, healed (12 h), healed (16 h) and control. Number of replicates for each group: 4, 3, 3, 4, respectively. Error bar is 1 standard deviation. **d**, Stress versus strain curves of 12 h healed CE6-AT films and 16 h healed CE6-AT films. Number of curves shown for both time points is 3. **e**, Toughness value of 0, 12 and 16 h healed films. Number of replicates for each group is 3. Error bar is one standard deviation.

4. Conclusion

In this report, we demonstrated the bacteria with surface-displayed associative proteins can assemble and grow into matrix-free cohesive films on perforated solid supports. When unstructured elastin-like-peptides (ELPs) were displayed at the cell surface, the bacterial film were soft and viscoplastic with Young's modulus in the range of tens of kPa. They yield easily and fail at 300-400 Pa of pressure. By adding a cysteine in the N-terminal region of the elastin-like-peptide, the Young's modulus increases three-fold and films no longer yield or fail under our testing conditions. We reduced the cysteine-containing films with TCEP and observed reduced mechanical strength, supporting the hypothesis that covalent disulfide bond crosslinks are crucial to the enhanced mechanical properties. These results imply that the mechanical properties of films made of protein-mediated bacterial assembly can be manipulated genetically and small mutations in protein sequence can markedly change mechanical properties. These living bacterial films can also self-heal within a day after injury. In summary, we created a living material system made of engineered bacteria that can autonomously assemble, with genetically encoded mechanical properties that can recover after damage.

5. Materials and Methods

Bacterial Strains. All experiments were conducted in *E. coli* strain DH10B (Invitrogen, Carlsbad, CA). Details of reagents, cloning and protein expression experiments can be found in **Table S3.1** and **Supplementary Notes 3.1-2**.

Preparation of Bacterial Films. Individual colonies harvested from LB plates were grown overnight to stationary phase in liquid LB medium supplemented with 100 mg/L ampicillin to maintain plasmid stability. The resulting cultures were then diluted to an optical density at 600 nm (OD₆₀₀) of approximately 0.8. Diluted cultures were loaded on UV-sterilized track-etched polycarbonate filters (Nuclepore Whatman, 0.2 µm pore size) mounted in vacuum filter units (Nalgene Rapid-flow Thermo-Fisher). For 2.5 cm diameter polycarbonate filters, 200 µL culture volumes were loaded and vacuum filtered. After filtration was complete, filters were transferred to fresh LB plates. Bacterial films were grown in a 37 °C incubator. Filters were moved to fresh LB agar plates containing suitable antibiotics every day for 7 days to allow film maturation and mechanical testing.

Erosion Assay. 7-day old bacterial films grown on membrane filters were immersed in 7 mL of 1x PBS buffer at pH 7.4 in the wells of 6-well plate (Corning, Thermofisher). The 6-well plate was then placed on a rocking platform (Bio-Rad) set at 15 ° tilt angle and 15 rpm frequency. The OD₆₀₀ of PBS in contact with the bacterial film was measured at 1 h and 24 h after rocking started.

Microtomy of Bacterial Films. 7-day old bacterial films on polycarbonate filters were cut with a 6 mm diameter biopsy punch (Miltex). The circular section of film was embedded in Tissue-Tek® resin (Sakura) and frozen at - 20 °C overnight. The frozen piece was microtomed at – 20 °C with each section of 50 µm thickness. Microtomed sections were placed on glass slides for staining and imaging.

Flow Cytometry. E6-AT films were scraped and transferred to an Eppendorf tube, blocked for 30 min with agitation (3% BSA in PBS). Cells were then centrifuged and resuspended in staining solution (5 µg/mL Anti-His conjugated Dylight 488 Antibody (HIS.H8 Thermofisher), 1% BSA in PBS). This solution was then agitated for 1 h, after which the cells were washed three times in PBS. Cells were strained through a 40 µm filter to remove aggregates and run on a MoFlo XDP cell sorter equipped with a 488 nm laser. Flow cytometry data were analyzed using MatLab.

Microtome staining. For antibody staining, microtome sections on glass coverslips were blocked with 3% BSA in PBS for 0.5 h under static conditions. The blocking buffers were then removed with a Kimwipes paper tissue. A staining solution (5 µg/mL Anti-His conjugated Dylight 488 Antibody (HIS.H8 Thermofisher), 1% BSA in PBS) was dropped on the coverslip and stained for 1 h in a dark chamber. The residual staining solution was removed with Kimwipes and microtome sections were washed with three times with 1% BSA in PBS before imaging. The microtome section on coverslip were then placed between coverslip and slide by a 120-µm spacer (SecureSeal™, VWR).

Bacterial Film Lysis. Bacterial films were scraped from the polycarbonate filter and lysed in 4% SDS 1xPBS pH 7.4 at 100 °C for 30 min on a thermo shaker (VWR Scientific) at 900 rpm in an Eppendoff tube. For 3-6 mg of bacterial films, 500 μ L of lysis buffer was added.

Quantification of Colony Forming Units. The bacterial film was scraped from the polycarbonate filter and weighed in an Eppendoff tube. 500 μ L of 1xPBS buffer pH 7.4 was added to the tube. The film was first agitated by pipetting up and down until broken into small pieces and vortexed at least three times until no large fragments (mm sized) could be observed and the suspension became turbid. The suspension was then serially diluted 10 to 10⁶-fold in a 96 well plate. Three 10 μ L drops of each kind of serial dilution was dropped on LB agar plates and incubated overnight. A plate with 10 to 100 colonies was selected, and the number of colonies on the plate was counted to allow calculation of the number of colony forming units (CFU) in the original bacterial film.

Bulge Test Device Assembly. Clear acrylic sheets (1/16" thickness, McMaster-Carr) were used as the base of the millifluidic device. Two sets of channels were etched or cut into the acrylic using a laser cutter (Industrial Laser ILS 9.75), and the individual pieces were assembled with epoxy adhesive to form the device in two parts that could be assembled reversibly. One vertical cylindrical hole and horizontal channel allowed "Reservoir 1" to be connected the top face of the device and control the pressure on the top face of the sample; another vertical cylindrical hole passed through the top part and connected to the horizontal channel in the lower part, allowing "Reservoir 2" to control the pressure below the sample. The channel above the sample was sealed with a glass cover slip to enable imaging. For the connections to the top face, thicker acrylic slabs

with through holes threaded to accept quick-tube coupling fittings (51525K442, McMaster-Carr) were bonded to the top surface. The reservoirs themselves were syringes of known internal diameters.

Sample Loading Protocol for the Bulge Test. A polycarbonate filter with a bacterial film grown on top was placed in a petri dish containing the sterile buffer used for bulge testing. A 3 mm diameter biopsy punch (Integra Biosciences) was used to gently make a circular cut through the bacterial film but not the polycarbonate. A sample support disk (copper TEM disk, 1.5 mm diameter circular aperture, 3.05 mm outer diameter, thickness 25 μm , Ted Pella) was then slid in between the bacterial film and polycarbonate from the outer edge of the film and used to gently separate the film from the polycarbonate. Once the edge of the film was freed, the cut 3 mm bacterial film disk freely floated away from its polycarbonate support, and could be lifted out of the buffer using the support disk and placed into the bottom chamber of the device (pre-filled with buffer). A second support disk was placed on top to sandwich the bacterial film, followed by an o-ring (Precision Associates, Inc). Prior to sealing the two halves of the device together, a 5 ml syringe was filled with buffer and capped with a 30G needle connected to thin silicone tubing (0.31 mm ID, 0.64 mm OD, HelixMark). The tubing was threaded through into the Luer socket on the top half of the device and placed along the top channel using forceps, such that the tube terminated in the viewing window of the chamber that would eventually be directly above the sample. Following this, the two chamber halves were sealed using a thin layer of vacuum grease. The two chambers were then filled simultaneously with buffer solution: the upper channel using the tubing connected to the syringe filled with buffer, and the lower channel by way of the associated Luer slip connector, drop by drop, until both connectors were filled,

following which the tubing was gently extracted and two reservoirs were attached to the Luer slip connectors on either side. Syringes used as reservoirs in the collected datasets were 60 ml syringes (BD Scientific) with ID = 26.72 mm. The apparatus was rinsed with soap and DI water and allowed to dry between uses; separate reservoirs and syringes were used for different buffers.

Bulge Test Pressure Profile Control. A syringe pump was used to impose various pressure-time profiles in these experiments. “Ramp” and “sawtooth” profiles involved PBS addition at a flow rate of 70 ml/min, with a final target volume of 55 ml in one ramp bulge test and 2 ml in each cycle of an oscillatory bulge test unless otherwise specified. The flow rate was chosen to be the maximum accommodated by the syringe pump in order to minimize perfusion through the biofilm for the duration of the experiment.

OCT Imaging. All OCT imaging was performed with a Thorlabs OCT (GAN210 base unit: 930 nm central wavelength, 6/4.5 μm axial resolution in air/water, 2.9/2.2 mm imaging depth (air/water), OCTP-900 scan head, OCT-LK3-BB scan lens: 36 mm FL, 8 μm lateral resolution). A-Scan/Line Rate was 36 kHz for all measurements (acquisition time = 19 ms). Biofilm thicknesses were calculated estimating a refractive index of 1.4. This value was based on both the manufacturer’s recommendation as well as prior literature on *E. coli*.⁴⁰

Image and Mechanical Property Analysis. The typical loading and imaging process generated over 2500 images showing the evolution of a biofilm cross section throughout the experiment (for some snapshots, see **Fig S3.22**, numbered images). The

features that could be captured were only limited by i) perfusion, which in most cases was negligible, ii) maximum fluid held by the reservoir, which was 70 ml, and iii) the thickness of the samples tested. Thicker samples would experience less stress at a given hydrostatic pressure, which meant the failure of a particular sample could not always be captured. A typical analysis protocol resulted in the stress-strain curve shown in **Fig S3.22**. The analysis protocol followed the assumptions of membrane theory, that: i) the thickness of the membrane is small in comparison to the in-plane dimensions ii) the bending stiffness is negligible and iii) due to (i) and (ii), in-plane stresses are assumed to be constant throughout the thickness of a membrane. Additionally, we assumed i) that there is an idealized equibiaxial deformation throughout the entire inflated membrane. In practice this is only true at the pole, and the deformation transitions to a constant width elongation at the clamped edge; also ii) that stress could be estimated using a spherical cap assumption, and strain could be estimated by changes in arc length of the deformed biofilm (**Fig 3.3A**).

Following the assumptions outlined above, the stress and strain states are as follows:

$$\sigma_{ij} = \begin{pmatrix} \sigma_1 & 0 & 0 \\ 0 & \sigma_2 & 0 \\ 0 & 0 & 0 \end{pmatrix}$$

$$\epsilon_{ij} = \begin{pmatrix} \epsilon_1 & 0 & 0 \\ 0 & \epsilon_2 & 0 \\ 0 & 0 & \epsilon_3 \end{pmatrix}$$

We assume here that $\sigma_1 = \sigma_2 = \sigma$ and $\epsilon_1 = \epsilon_2 = \epsilon$ across the entire membrane.

Applying Hooke's law, the relationship between σ and ϵ is:

$$\sigma = \frac{E}{1-\nu} \epsilon$$

Where $\frac{E}{1-\nu}$ is the biaxial modulus of the material, referred to as the “modulus” in

further text, and evaluated from the linear regions of each plot. We do not report the

two quantities E and ν independently since they cannot be deconvolved using only one measurement method.

2D datasets were exported as tiff files and cropped using ImageJ. The resulting images were processed with in-house MATLAB scripts: the images were binarized; the top and bottom surfaces of the film were detected based on changes in pixel intensity and fit to fourth degree polynomials which were then used to estimate arc lengths of the top and bottom surfaces of the film (**Fig S3.23**). Engineering strain ϵ was calculated as change in arc length divided by the original arc lengths of the top and bottom surfaces respectively.

Nominal stress was calculated with the equation for stress in a thin-walled spherical pressure vessel:

$$\sigma = \frac{PR}{2t}$$

Where σ is film stress, P is the applied pressure, R is bulge radius of curvature, and t is film thickness. Further, $R = \sqrt{a^2 + h^2}$ where a is radius of aperture of the support disk and h is deflected height of the center of the film, directly measurable by OCT. For 2D datasets, the plotted data were averaged (top and bottom surfaces of the biofilm). True stress and strain were used for some films where indicated. The ratio of aperture diameter $2a$ to film thickness t ranged from 16.6 – 25. Although the ideal ratio for the membrane assumption would be > 20 , variations of stresses and strains through the thickness were neglected in our calculations based on the fact that the top and bottom surfaces of the biofilm did not show a significant difference in their stress-strain data (**Fig S3.24**).

Image Processing and Data Analysis. Image color-coding was done by ImageJ. Intensity normalization of the z-stacks was done in ImageJ. 3D rendering of z-stacks

was done in either ImageJ or Zeiss Zen Blue. Data plotting and analysis, were performed in MatLab and Prism (GraphPad).

Fluorescence Imaging. The fluorescence images of processed samples with fluorescent labels were obtained with a 63X, 1.518 N.A. oil-immersion objective on a Zeiss LSM 880 confocal microscope (Carl Zeiss AG, Oberkochen, Germany) at the Caltech Biological Imaging Facility. Single-photon confocal laser scanning imaging was performed with 488-nm and 591-nm lasers and in the mWasabi ($\lambda_{\text{ex}}/\lambda_{\text{em}}$: 493/509 nm), mCherry ($\lambda_{\text{ex}}/\lambda_{\text{em}}$: 587/610 nm), and Dylight 488 channels ($\lambda_{\text{ex}}/\lambda_{\text{em}}$: 493/518 nm). The images were visualized and analyzed with Fiji or Imaris Viewer. (Oxford Instruments, Abingdon, UK)

Statistics and Reproducibility. For most experiments creating the micrographs reported herein, the data generated were done in triplicates. The number of replicates for experiments are specified in figures and supporting information.

6. Acknowledgements and Contributions. Hanwei Liu conceived and designed the experiments under the supervision of Professor David A. Tirrell. Hanwei Liu was responsible for all the genetic engineering experiments, bacterial film growth, sample preparation and fluorescence imaging. Priya K. Chittur performed all experiments related to the biofilm mechanical property analysis using the bulge test device under the supervision of Professor Julia A. Kornfield. This chapter was written mainly by Hanwei Liu; Priya K. Chittur provided written material characterization methods and values of material properties.

7. Supporting Information.

Supplementary Note 3.1: Reagents and suppliers

Restriction enzymes, ligase, and Q5 DNA polymerase were purchased from New England Biolabs (Beverly, MA). DNA oligos and G-blocks were purchased from Integrated DNA Technologies (Coralville, IA).

Supplementary Note 3.2: Plasmid subcloning

Recombinant fusion proteins were produced by standard recombinant DNA technology. DH10B *E. coli* were used for all cloning steps and material preparation.

Genes encoding the autotransporter protein along with elastin solubility/stability tags have been previously cloned by our group into modified pQE-80L plasmids.³¹

pX-E6 plasmid containing 6 elastin-like-peptide repeat reported in previous works^{31,33,34} with 5' BamHI and 3' XhoI was digested by corresponding enzymes and inserted into a similarly digested pAT-ST vector to make pAT-E6 plasmid. The T5 promoter of the plasmid drives constitutive expression of protein E6-AT.

pAT-ST plasmid encoding a SpyTag peptide fused with autotransporter was mutated to have a cysteine after 6xHis tag and before SpyTag peptide. pX-E6 plasmid containing 6 elastin-like-peptide with 5' BamHI and 3' XhoI was digested by corresponding enzymes and inserted into a similarly digested pAT-ST vector with cysteine mutation to make pAT-CE6 plasmid. The T5 promoter of the plasmid drives constitutive expression of protein CE6-AT. The sequence of all constructs were sequenced and confirmed by Laragen Inc. (Culver City, CA)

Supplementary Note 3.3: Buffer recipe

The 20 mM HEPES buffer in this work doesn't contain any PO_4^{3-} . The buffer contains 20 mM HEPES, 115 mM NaCl, and 1.2 mM MgCl_2 buffered at pH 7.0.

The 1x PBS buffers used in this work was purchased from ThermoFisher Scientific containing 155 mM NaCl, 1 mM KH_2PO_4 and 3 mM Na_2HPO_4 buffered at pH 7.4.

Table S3.1: Plasmids used in this study

Name	Backbone/origin/promoter	Purpose
pQE-Empty	pQE80l/colE1/T5	Empty plasmid for cloning and providing ampicillin resistance
pAT-E6	pQE80l/colE1/T5	Constitutive expression of E6-AT protein on cell surface
pAT-CE6	pQE80l/colE1/T5	Constitutive expression of CE6-AT protein on cell surface
pX-E6	pQE80l/colE1/T5	Cloning of pAT-E6 and pAT-CE6
pAT-ST	pQE80l/colE1/T5	Cloning of pAT-E6 and pAT-CE6
pKPY680	pBAD33/p15a/pJ23100	Constitutive expression of mWasabi
pKPY681	pBAD33/p15a/pJ23100	Constitutive expression of mCherry

Table S3.2: Protein sequences

Protein:	Sequence
E6-AT	<p> MKYLLPTAAAGLLLLAAQPAMAMRGSHHHHHHGSVDVPG AGVPGAGVPGEGVPGAGVPGAGVPGAGVPGAGVPGEGVPG AGVPGAGVPGAGVPGAGVPGEGVPGAGVPGAGLDVPGAG VPGAGVPGEGVPGAGVPGAGVPGAGVPGAGVPGEGVPGAG VPGAGVPGAGVPGAGVPGEGVPGAGVPGAGLETPTPGPDL NVDNDLRPEAGSYIANLAAANTMFTTRLHERLGNTYYTDM VTGEQKQTTMWMRHEGGHNKWRDGSQQLKTQSNRYVLQ LGGDVAQWSQNGSDRWVHVMAGYGNSDSKTISSRTGYR AKASVNGYSTGLYATWYADDESNGAYLDSWAQYSWFDN TVKGDDLQSESYKSKGFTASLEAGYKHKLAEFNGSQGTRNE WYVQPQAQVTWMGVKADKHRESNGTLVHSNGDGNVQTR LGVKTWLKSHHKMDDGKSREFQPFVEVNWLNHNSKDFSTSM DGVSVTQDGARNIAEIKTGVEGQLNANLNVWGNVGVQVA DRGYNDTSAMVGIKWQF </p>
CE6-AT	<p> MKYLLPTAAAGLLLLAAQPAMAMRGSHHHHHHCGSVDVP GAGVPGAGVPGEGVPGAGVPGAGVPGAGVPGAGVPGEGVP GAGVPGAGVPGAGVPGAGVPGEGVPGAGVPGAGLDVPGA GVPGAGVPGEGVPGAGVPGAGVPGAGVPGAGVPGEGVPGA GVPGAGVPGAGVPGAGVPGEGVPGAGVPGAGLETPTPGPD LNVDNDLRPEAGSYIANLAAANTMFTTRLHERLGNTYYTD MVTGEQKQTTMWMRHEGGHNKWRDGSQQLKTQSNRYVL QLGGDVAQWSQNGSDRWVHVMAGYGNSDSKTISSRTGY RAKASVNGYSTGLYATWYADDESNGAYLDSWAQYSWFD NTVKGDDLQSESYKSKGFTASLEAGYKHKLAEFNGSQGTR NEWYVQPQAQVTWMGVKADKHRESNGTLVHSNGDGNVQ TRLGVKTWLKSHHKMDDGKSREFQPFVEVNWLNHNSKDFST SMDGVSVTQDGARNIAEIKTGVEGQLNANLNVWGNVGVQ VADRGYNDTSAMVGIKWQF </p>

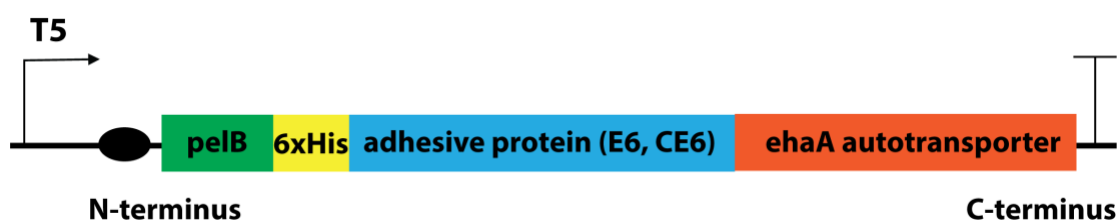


Figure S3.1. Expression construct for surface displayed adhesive proteins.

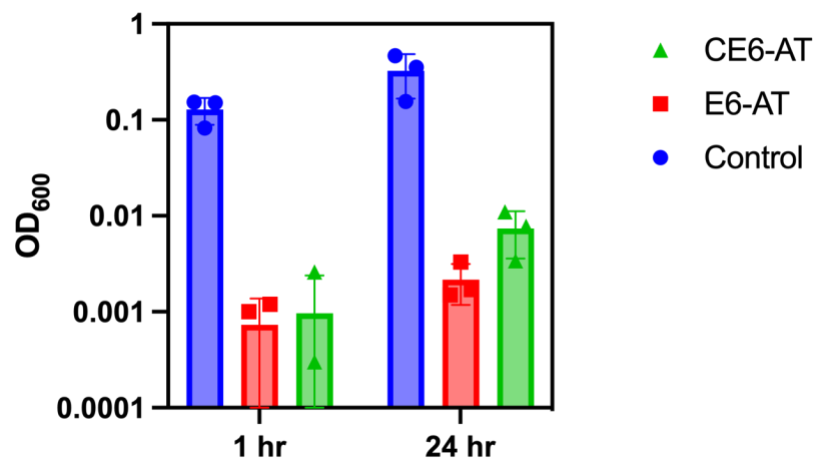


Figure S3.2. Erosion assay results for control, CE6-AT and E6-AT. OD₆₀₀ of PBS buffer was measured at 1 hour and 24 hours after erosion started.

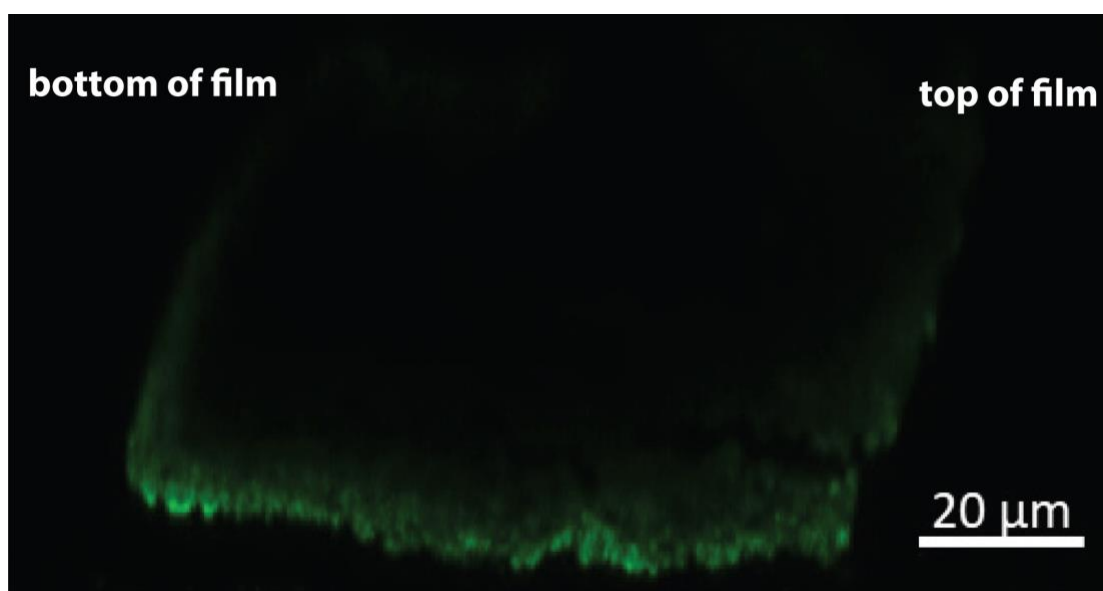


Figure S3.3. Cross sectional view of CE6-AT microtome section stained with fluorescent antibody. The bottom of the original bacterial films is on the left and top of the film on the right. The bottom green line is the cut made by the microtome machine and later stained by fluorescent antibody. Since the film is made of densely packed bacteria and relative large molecular weight of antibody, the antibody only effectively stains around 5 μm deep into the film. From the stained part at the cut site, we can see protein expression (antibody staining) across all thickness in the film. Scale bar 20 μm .

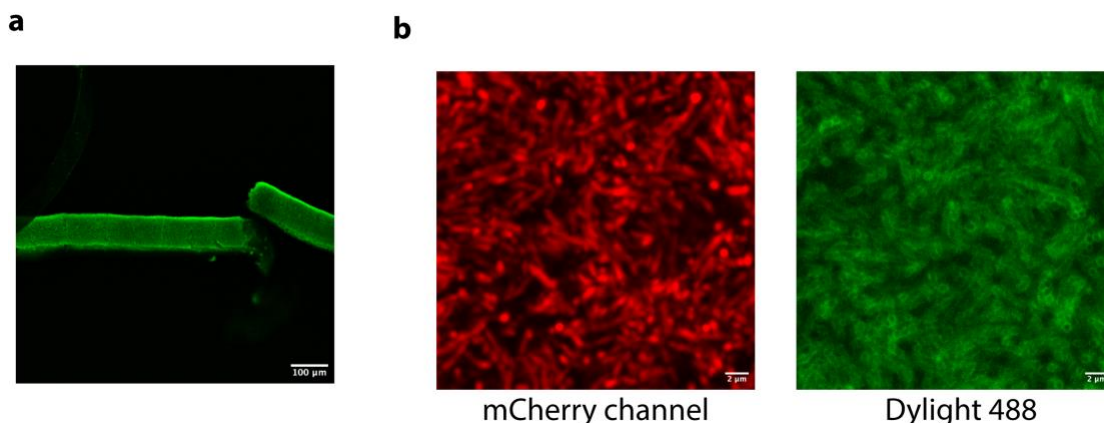


Figure S3.4. Fluorescent antibody staining of E6-AT films. **a**, Microtome sections of E6-AT films were stained with anti-His tag antibody conjugated with Dylight 488 dye. Expression of E6-AT proteins across all thickness was shown. Scale bar, 100 μm . **b**, A E6-AT film was engineered to constitutively express mCherry and stained by anti-His tag antibody conjugated with Dylight 488. mCherry channel showed cells packed in the bacterial film and Dylight 488 channel showed expression of E6-AT protein at cell surface. Scale bar, 2 μm .

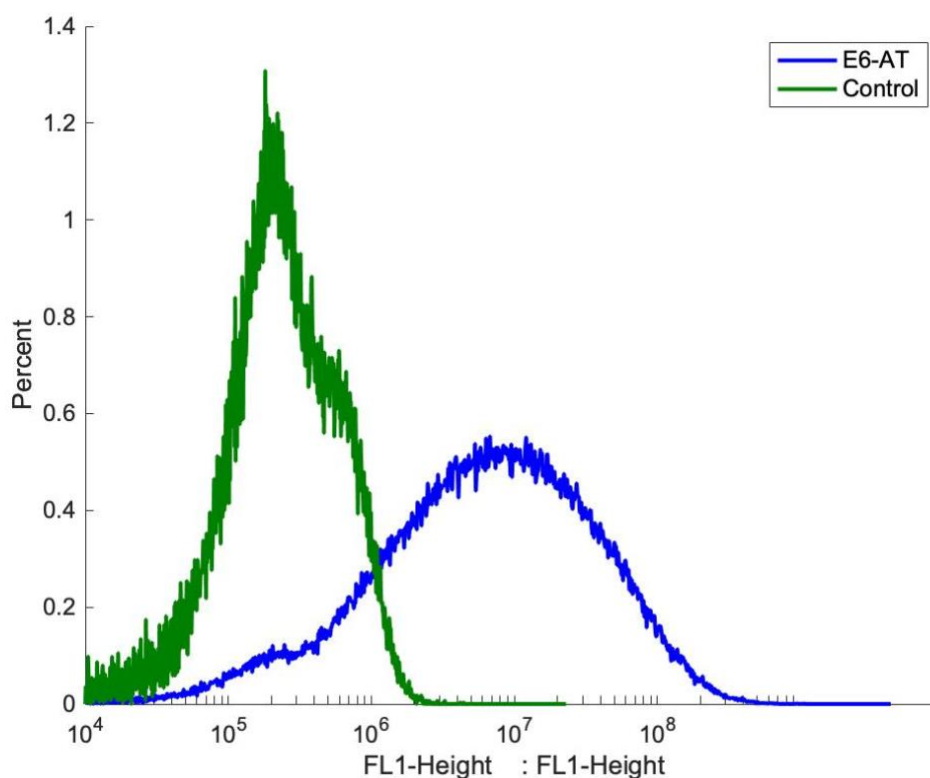


Figure S3.5. Flow cytometry data of E6-AT films. Flow cytometry enables relative quantification of protein expression level. Both control and E6-AT films were sampled and stained with anti-His tag antibody conjugated to Dylight 488 and run through the flow cytometer. X-axis values correspond to labeling intensity of antibody to a single bacterium and Y-axis values corresponds to percentage of population. From this diagram, we can clearly see that E6-AT has stronger labeling intensity compared to the control, meaning relative high expression level of protein at surface. CE6-AT can't be analyzed using flow cytometry due to the concern of giant cell clusters clogging the flow cytometer.

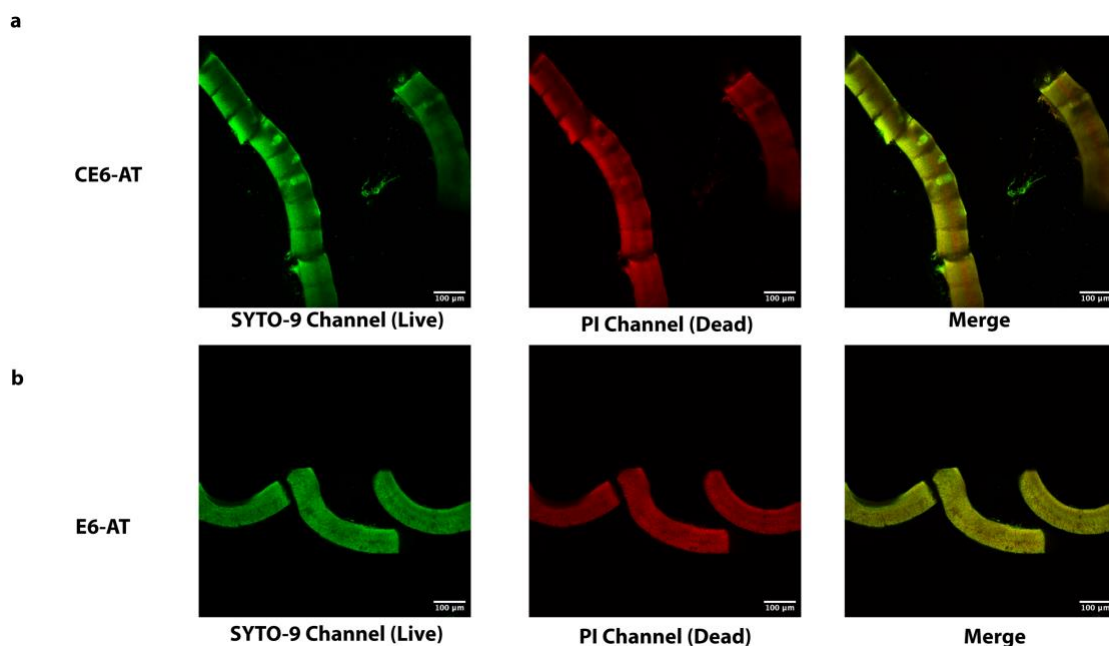


Figure S3.6. Live-dead staining images of CE6-AT and E6-AT films' microtome cross section. **a.** Microtome sections of CE6-AT films stained by Live-dead stains. Green SYTO-9 channel corresponds to distribution of living cells and red PI channel corresponds to dead cells. We find that there are living and dead cells across all thickness. From the merged channel, we find a thin layer about 60 μm to have more dead cells compared to rest of the film. Scale bar, 100 μm . **b.** Microtome sections of CE6-AT films stained by Live-dead stains. Interestingly for E6, both live and dead cells are distributed homogeneously across all thickness. Scale bar, 100 μm .

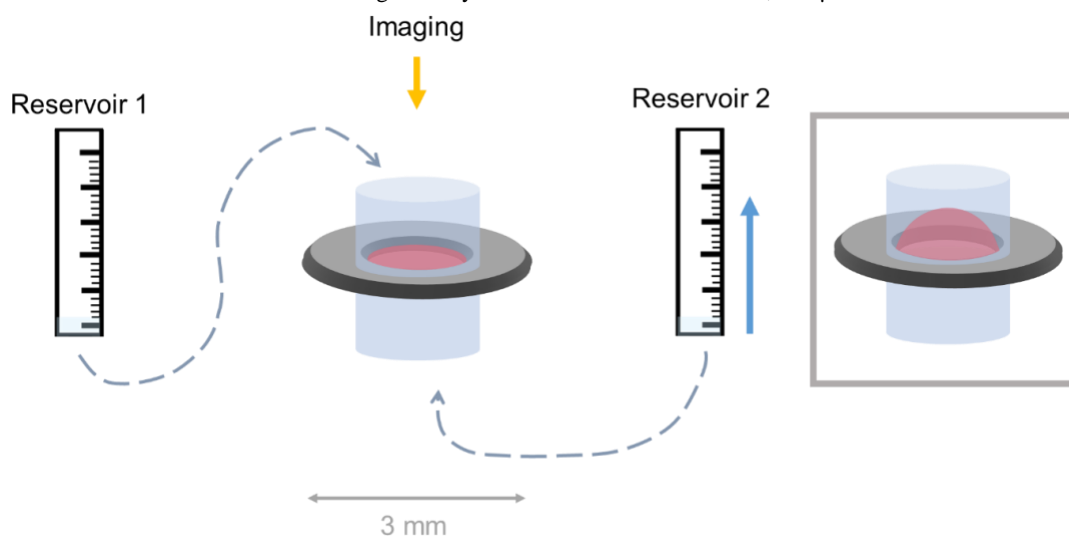


Figure S3.7. Schematic of bulge test process. As fluid height increases in the reservoir connected to the chamber underneath the film, the film "inflates" through central aperture (gray box).

Analyzing stress-strain curve for ramp pressure loading

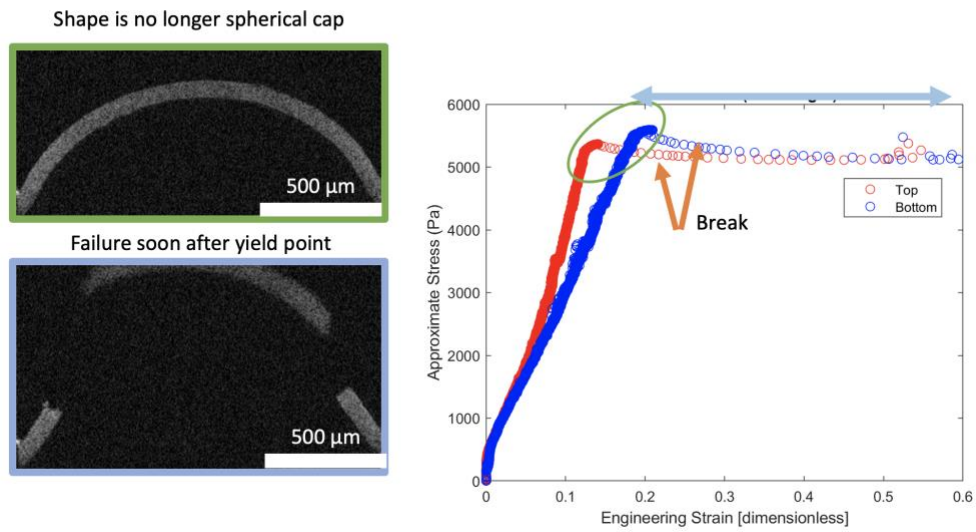


Figure S3.8. Failure of CE6-AT film. This CE6-AT film was accidentally soaked in PBS for 4 hours. The failure happened abruptly. Failure and yielding happened around the same time. The part that failed, detached from the main sample immediately like a stone shot by a slingshot. Video of failure is in the slide attached.

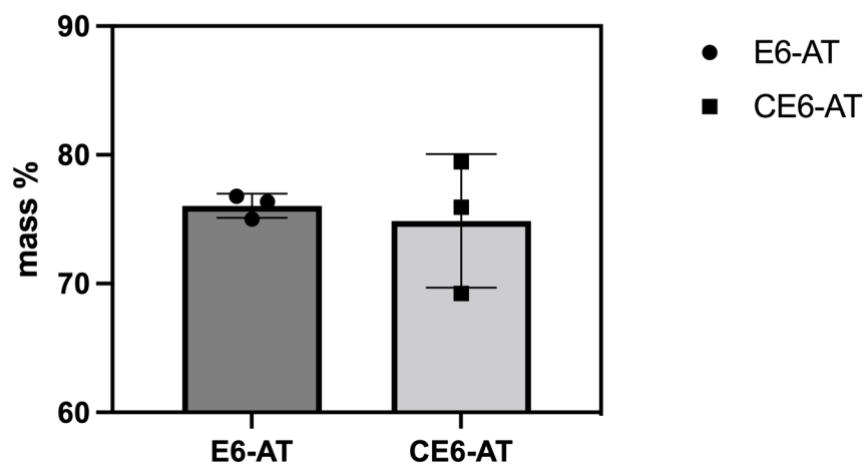


Figure S3.9. Mass percentage of water in the E6-AT and CE6-AT films. Both kinds have about 75% of mass being water. According to literature 1 *E. coli* cell has 74% mass being water.⁴¹ Number of replicates: 3.

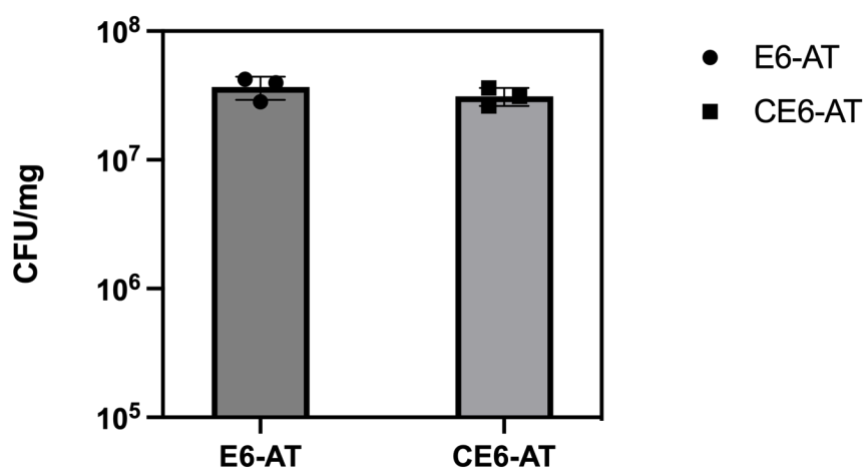


Figure S3.10. Colony forming units of E6-AT and CE6-AT films per unit mass. Both films has CFU around 3×10^7 viable cells per mg of film. Number of replicates: 3.

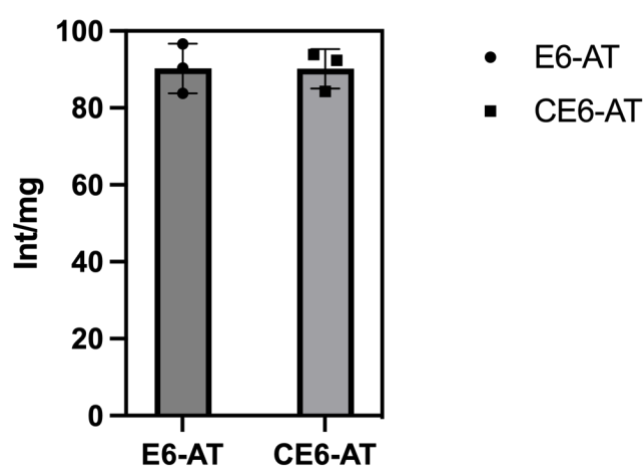


Figure S3.11. Expression level of E6-AT and CE6-AT films per unit mass. Int refers to intensity of band of protein in Western blot image. The intensity of protein band was normalized by mass of films loaded for gel analysis. Number of replicates: 3.

Supplementary Note 3.4: Calculation of CE6-AT numbers per cell using TCEP Reduction.

Using Beer's law,⁴² we measured the absorbance versus concentration for Dylight 633-maleimide at 633 nm as calibration curve.

$$A = \epsilon lc$$

A is absorbance; ϵ is molar extinction coefficient of the molecule; l is light path length; c is concentration of the molecule.

In this case the l is same for all test and the extinction coefficient we get from calibration is $E = \epsilon l$

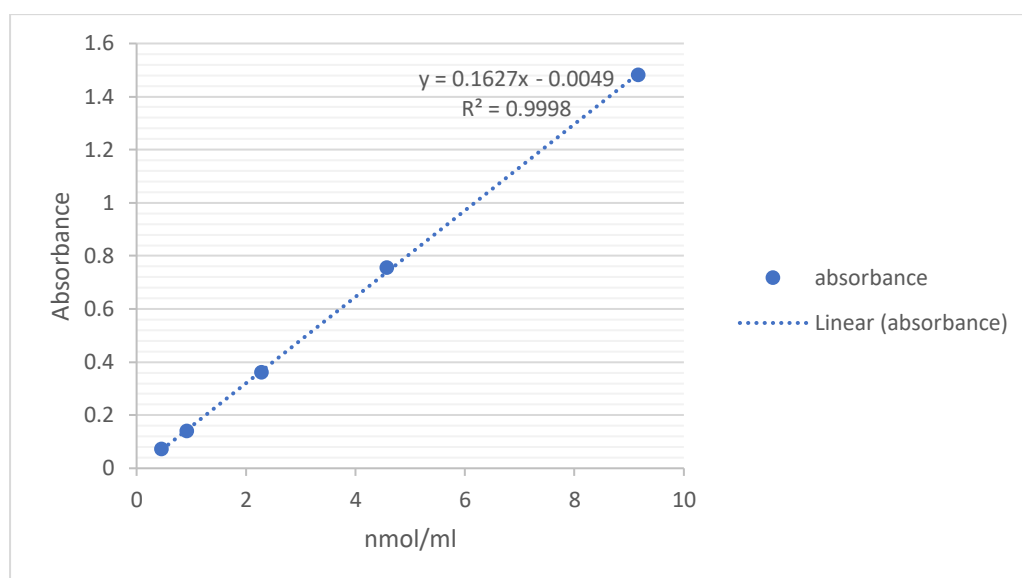


Figure S3.12. Calibration curve for Dylight 633-maleimide at 633 nm.

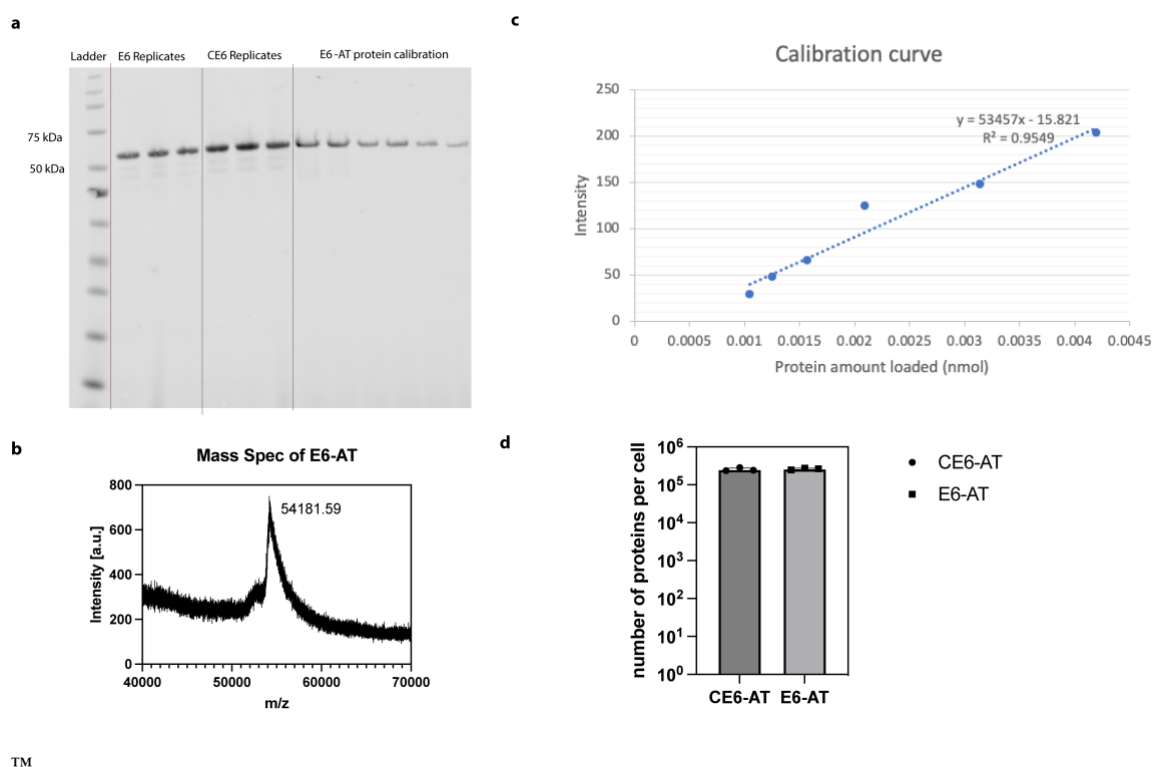
From this calibration curve, we can get molar extinction coefficient ϵ of Dylight 633 maleimide dye equals to $0.1627 \mu\text{M}^{-1} \cdot \text{cm}^{-1}$. We assume the labeling intensity difference Δ between CE6-AT TCEP + and E6-AT TCEP + groups is a result of CE6-AT protein that is reduced by TCEP and labeled by Dylight 633 maleimide dye. By plugging Δ into the calibration curve, we can get the concentration of CE6-AT protein. We then times the dilution times of lysate and assuming the mass of one *E. coli* cell to be 1 pg (10^9 cells per mg of bacterial film) to get number of proteins per cell⁴³.

$$\# \text{ of proteins per cell} = (\Delta/E) * (\text{Dilution times}) / 10^9$$

The value we got for CE6-AT per cell was around $2.5 * 10^5$ proteins per cell.

Supplementary Note 3.5: Calculation of CE6-AT and E6-AT numbers per cell using Quantitative Western Blot.

First we scraped off CE6-AT and E6-AT films of known mass. We then lysed the films in 4% SDS 1xPBS pH 7.4 at 100 °C for 30 min on a thermo shaker (VWR Scientific) at 900 rpm. E6-AT protein were previously purified under denaturing conditions (8 M urea) and using an Anti-His tag resin (Qiagen) and eluted with 20 mM imidazole. A BCA assay kit (Thermo Fisher) was used to measure the concentration of purified E6-AT proteins in 8 M urea, Tris buffer at pH 8.0. The concentration of protein was measured to be 0.76 mg/ml. Buffer exchange for denatured, purified E6-AT to a 10 mM ammonium acetate solution was accomplished with Amicon Ultra diafiltration units (3 kDa MWCO) by repeat centrifugation and wash steps. This protein solution was mixed 1:1 with super-DHB matrix and analyzed by MALDI-TOF to be 54181.59. We then ran a gel with E6-AT proteins with known concentration and 10-fold diluted lysate of E6-AT and CE6-AT films together. The gel was then transferred to iBlot protein transfer apparatus (Invitrogen) and blocked with 5% milk in 0.1% tween-20 in 1x PBS for 1.5 h. Dylight 650 anti-6x His tag antibody at a concentration of 0.1 µg/ml was used to stain the protein band on blot. The blot was imaged by Typhoon Gel Scanner (General Electrics). The image was analyzed by ImageJ software with intensity for bands of E6-AT for calibration. The calibration curve was shown in **Figure S3.13b**. Intensity of bands for E6-AT and CE6-AT lysate was also quantified by ImageJ and the value was plugged back into the calibration curve and protein number per cell can be back calculated. For CE6-AT, we got $2.5 \times 10^5 \pm 2.6 \times 10^4$ proteins per cell; E6-AT has $2.6 \times 10^5 \pm 1.3 \times 10^4$ proteins per cell.



TM

Figure S3.13. Quantitative Western blot analysis. **a**, Western Blot gel image of 3 replicates of E6-AT, 3 replicates of CE6-AT films and calibration loading of purified E6-AT films with known concentration. **b**, Mass spec data of purified E6-AT films using MALDI. **c**, Calibration curve of E6-AT protein with known loading amount. **d**, Number of proteins per cell estimation for CE6-AT and E6-AT proteins.

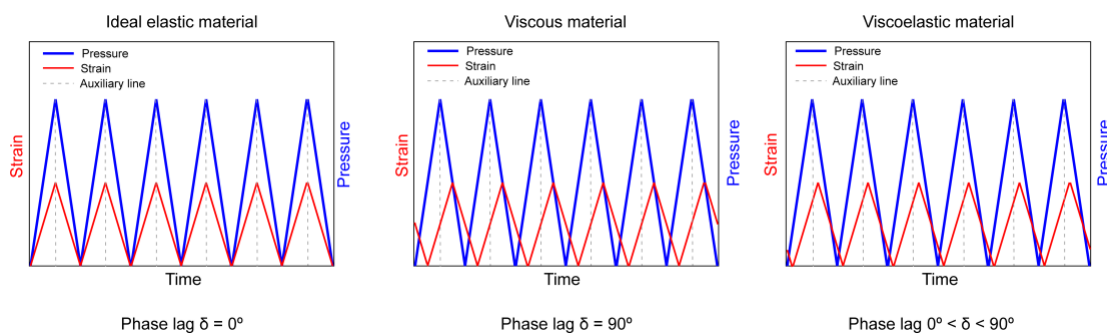


Figure S3.14. Phase relations for elastic, viscous and viscoelastic materials.

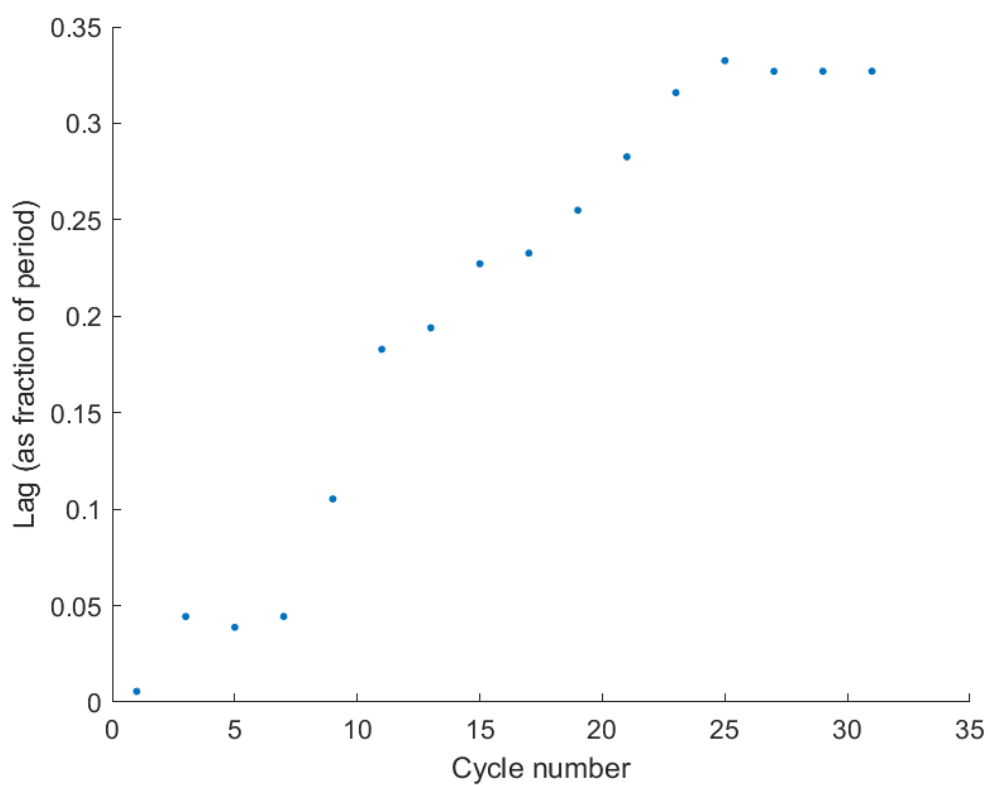


Figure S3.15. Phase lag of E6-AT films.

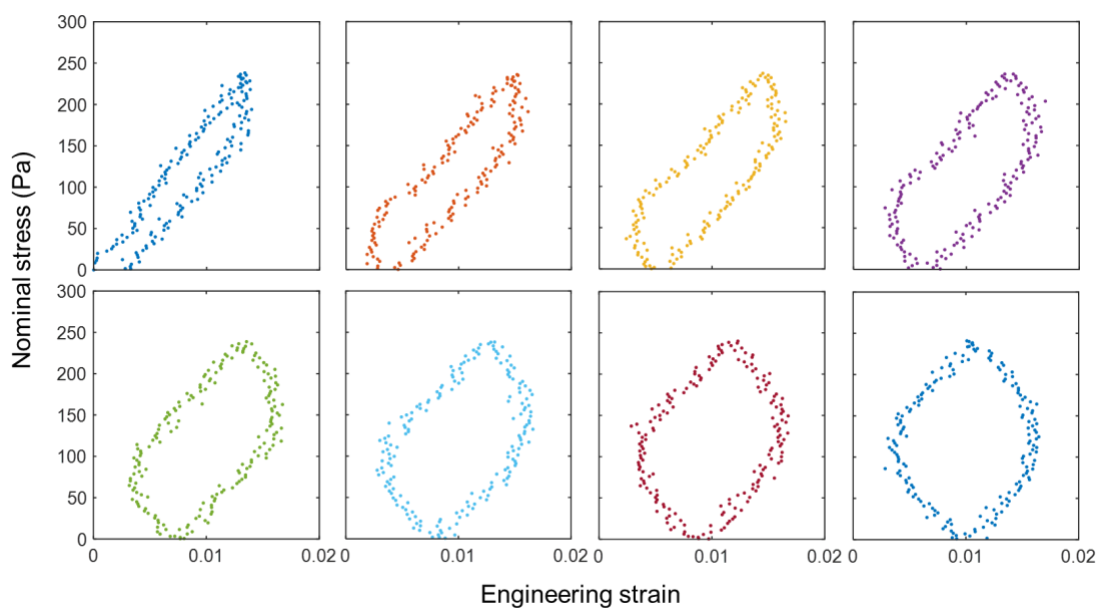


Figure S3.16. First 8 cycles loading and unloading curves of E6-AT films. E6 displays a viscoplastic response at pressures comparable to those used for CE6. The permanent deformation is mostly in the first two cycles; after which the response is viscoelastic.

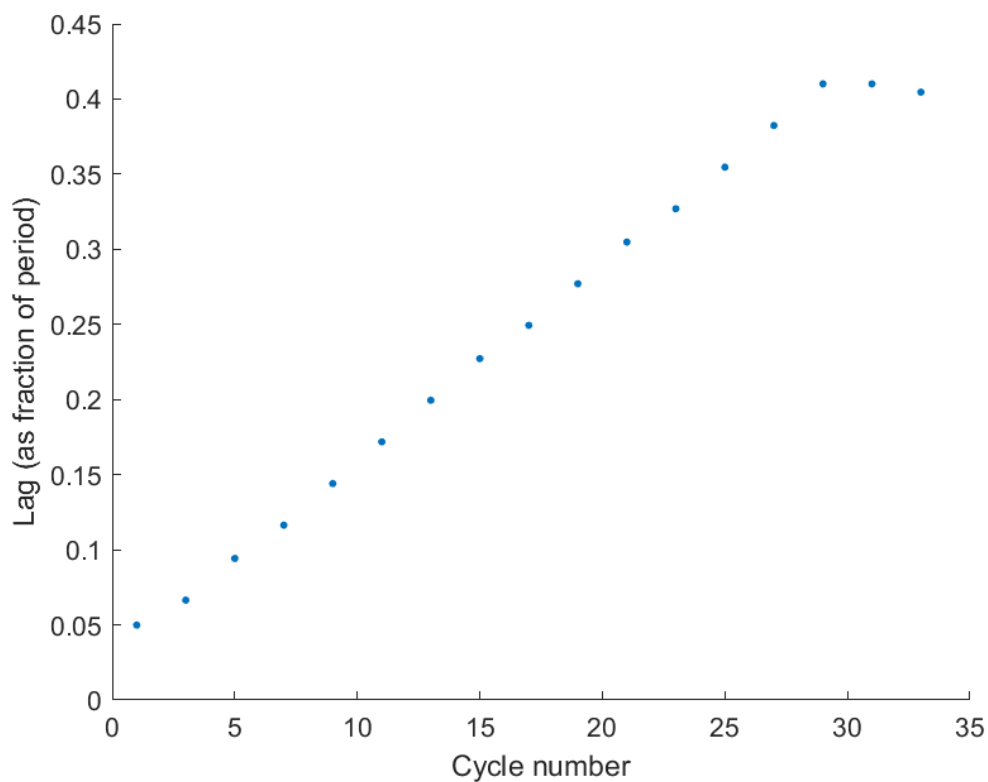


Figure S3.17. Phase lag of CE6-AT films.

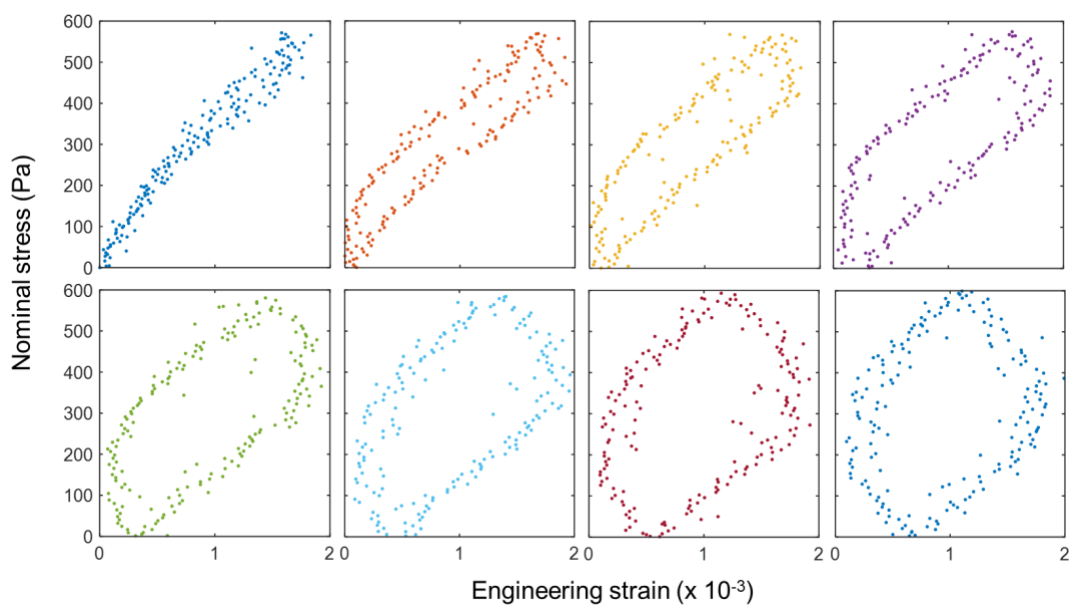


Figure S3.18. First 8 cycles loading and unloading curves of CE6-AT films. CE6 displays an initially almost elastic response (top left), transitioning to a more viscoelastic response indicated by the increasing area between the loading and unloading curves. Engineering strain axes are scaled by 10^3 for clarity.

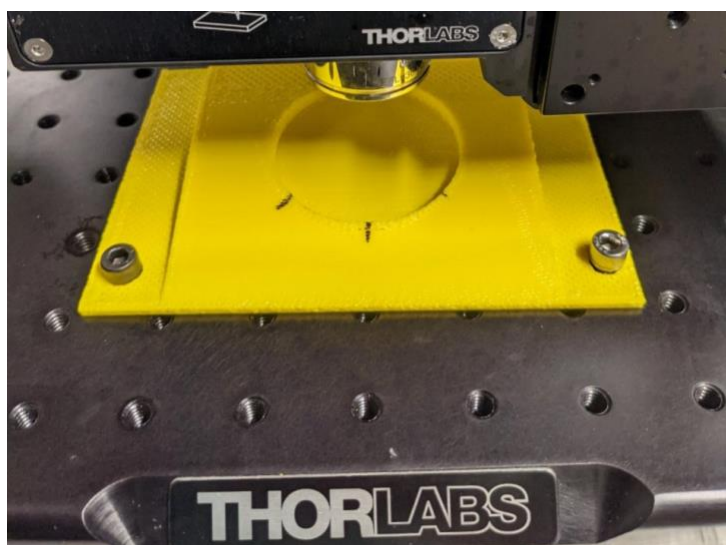


Figure S3.19. Sample holder for *in situ* tracking of bacterial film self-healing.

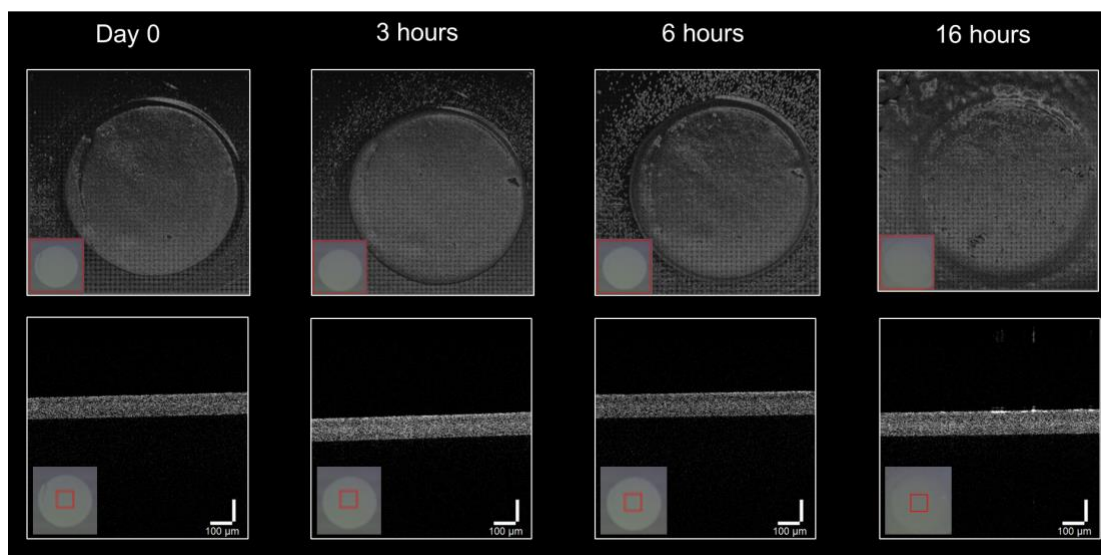


Figure S3.19. OCT scans of CE6-AT control on 2YT plate. Top row – patterned artifact due to software, not biofilm. Scale: top, 4 x 4 mm scan box; bottom, 1 x 1 x 1 mm scan box. Insets are OCT camera images, manually cropped to region being scanned. Red rectangular outline represents scan box (automatic, from ThorImage OCT software).

Table S3.3. Sample statistics for healed biofilms

	Total number of samples	Successfully peeled from agar and loaded (% of total)	Survived initial filling/pressure equilibration (% of total)	Failed within imposed pressures during bulge test (% of tested)
Original (Day 0)	4	4 (100)	4 (100)	0 (0)
Controls (16 hours)	4	4 (100)	4 (100)	2 (50)
Healed (6 hours)	4	3 (75)	0 (0)	-
Healed (12 hours)	6	5 (83)	4 (66)	4 (100)
Healed (16 hours)	7	6 (86)	3 (43)	3 (100)
Healed (24 hours)	10	8 (80)	0 (0)	-

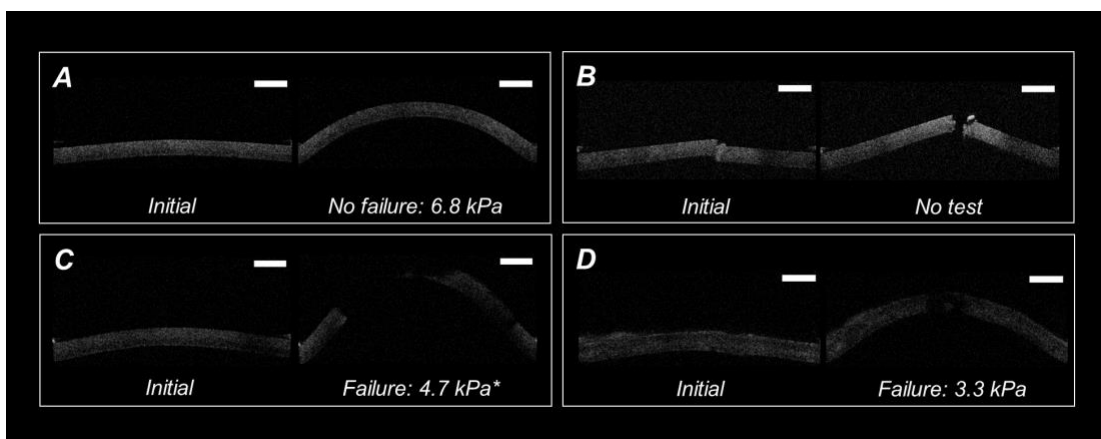


Figure S3.20. OCT scans of CE6-AT films with defect and healed. Original, day 7 CE6-AT films (A) do not fail within the limits of our test. Pictured maximum stress tested: 6.68 kPa. Cut films (B) immediately after injury cannot be tested, as the fluid freely flows through the tear (right). *50% of control films failed; pictured film (C) showed failure at stress: 4.68 kPa. All healed films failed (D); pictured maximum stress tolerated 3.32 kPa. Scale 200 μm .

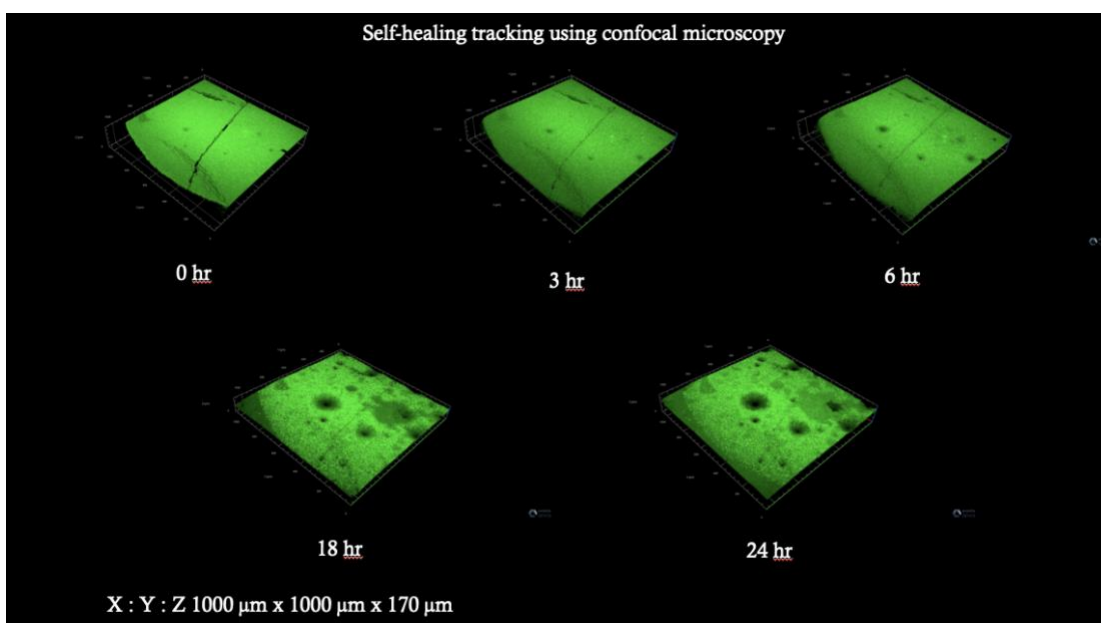


Figure S3.21. Confocal microscopy scanning of mWasabi CE6-AT films during healing process. Time recorded at 0, 3, 6, 18 and 24 hours. Dimensions of 3D rendering: 1000 μm x 1000 μm x 170 μm

Supplementary Note 3.6.A millifluidic device to apply the bulge test to biofilms

Literature on the bulge test has typically focused on its application to metal sheets, polymer films, and biological skin tissue^{44–55}. The delicate nature of biofilms, however, requires a device that applies much smaller pressure differences than these previous use cases. To adapt the bulge test to biofilms, we constructed a custom millifluidic device suitable for imposing Pa-kPa pressure differences across a freely suspended biofilm, equipped with an optical coherence tomography system to quantify the resulting changes in the shape of the biofilm.

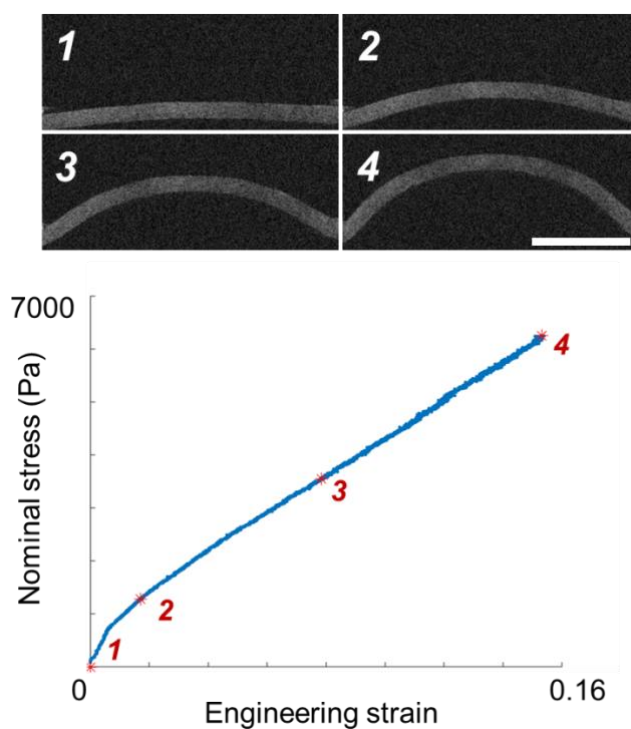


Figure S3.22. Cross sectional OCT images (top, numbered) acquired during the bulge test of a CE6-AT film with subsequent 2D processing and stress-strain curve displayed below. Numbers with asterisks indicate data points corresponding to the images. Scale bar 500 μm . Bacterial film did not fail during experiment.

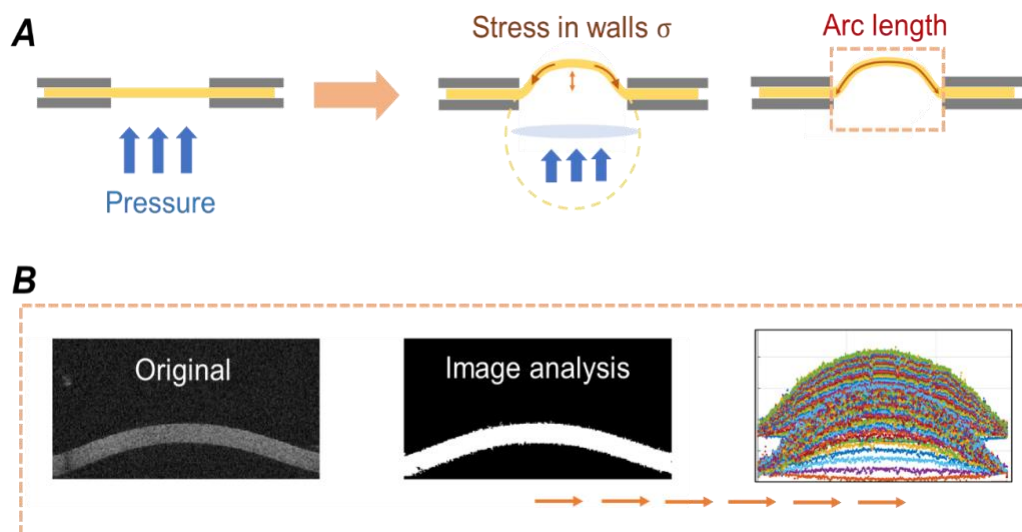


Figure S3.23, A) Spherical cap approximation for stress assumes that deformed film is part of a larger spherical pressure vessel and the stress in the walls of the film balances the applied pressure. Strain is estimated as a difference in the arc length (red arrow) compared to the original (flat) length of the biofilm. B) Image processing scripts binarize and clean up OCT images and detect the top and bottom surfaces of the film over thousands of images (bottom right).

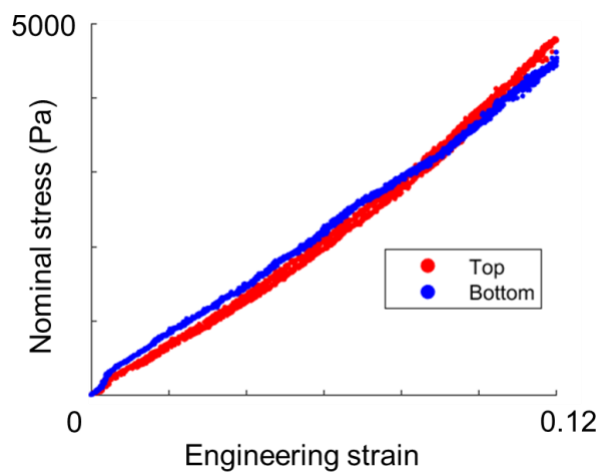


Figure S3.24, We observed minimal discrepancy between stress-strain curves from the top vs. bottom surfaces of the bacterial film.

8. Reference

1. Flemming, H.-C. *et al.* Biofilms: an emergent form of bacterial life. *Nat. Rev. Microbiol.* **14**, 563–575 (2016).
2. Gambino, M. & Cappitelli, F. Mini-review: Biofilm responses to oxidative stress. *Biofouling* **32**, 167–178 (2016).
3. Cheng, K. Y., Ho, G. & Cord-Ruwisch, R. Anodophilic Biofilm Catalyzes Cathodic Oxygen Reduction. *Environ. Sci. Technol.* **44**, 518–525 (2010).
4. Rosche, B., Li, X. Z., Hauer, B., Schmid, A. & Buehler, K. Microbial biofilms: a concept for industrial catalysis? *Trends Biotechnol.* **27**, 636–643 (2009).
5. Vert, M. *et al.* Terminology for biorelated polymers and applications (IUPAC Recommendations 2012). *Pure Appl. Chem.* **84**, 377–410 (2012).
6. Flemming, H.-C. & Wingender, J. The biofilm matrix. *Nat. Rev. Microbiol.* **8**, 623–633 (2010).
7. Flemming, H.-C., Neu, T. R. & Wozniak, D. J. The EPS Matrix: The “House of Biofilm Cells”. *J. Bacteriol.* **189**, 7945–7947 (2007).
8. Gilbert, C. & Ellis, T. Biological Engineered Living Materials: Growing Functional Materials with Genetically Programmable Properties. *ACS Synth. Biol.* **8**, 1–15 (2019).
9. Nguyen, P. Q., Courchesne, N.-M. D., Duraj-Thatte, A., Praveschotinunt, P. & Joshi, N. S. Engineered Living Materials: Prospects and Challenges for Using Biological Systems to Direct the Assembly of Smart Materials. *Adv. Mater.* **30**, 1704847 (2018).
10. Srubar, W. V. Engineered Living Materials: Taxonomies and Emerging Trends. *Trends Biotechnol.* **39**, 574–583 (2021).

11. Chen, A. Y., Zhong, C. & Lu, T. K. Engineering Living Functional Materials. *ACS Synth. Biol.* **4**, 8–11 (2015).
12. Tang, T.-C. *et al.* Materials design by synthetic biology. *Nat. Rev. Mater.* **6**, 332–350 (2021).
13. Chen, A. Y. *et al.* Synthesis and patterning of tunable multiscale materials with engineered cells. *Nat. Mater.* **13**, 515–523 (2014).
14. Zhong, C. *et al.* Strong underwater adhesives made by self-assembling multi-protein nanofibres. *Nat. Nanotechnol.* **9**, 858–866 (2014).
15. Caro-Astorga, J., Walker, K. T., Herrera, N., Lee, K.-Y. & Ellis, T. Bacterial cellulose spheroids as building blocks for 3D and patterned living materials and for regeneration. *Nat. Commun.* **12**, 5027 (2021).
16. Gilbert, C. *et al.* Living materials with programmable functionalities grown from engineered microbial co-cultures. *Nat. Mater.* **20**, 691–700 (2021).
17. González, L. M., Mukhitov, N. & Voigt, C. A. Resilient living materials built by printing bacterial spores. *Nat. Chem. Biol.* **16**, 126–133 (2020).
18. Jo, H. & Sim, S. Programmable Living Materials Constructed with the Dynamic Covalent Interface between Synthetic Polymers and Engineered *B. subtilis*. *ACS Appl. Mater. Interfaces* **14**, 20729–20738 (2022).
19. Nguyen, P. Q., Botyanszki, Z., Tay, P. K. R. & Joshi, N. S. Programmable biofilm-based materials from engineered curli nanofibres. *Nat. Commun.* **5**, 4945 (2014).
20. Huang, J. *et al.* Programmable and printable *Bacillus subtilis* biofilms as engineered living materials. *Nat. Chem. Biol.* **15**, 34–41 (2019).
21. Aswini, K., Gopal, N. O. & Uthandi, S. Optimized culture conditions for bacterial cellulose production by *Acetobacter senegalensis* MA1. *BMC Biotechnol.* **20**, 46 (2020).

22. Lahiri, D. *et al.* Bacterial Cellulose: Production, Characterization, and Application as Antimicrobial Agent. *Int. J. Mol. Sci.* **22**, 12984 (2021).
23. Chen, B. *et al.* Programmable living assembly of materials by bacterial adhesion. *Nat. Chem. Biol.* **18**, 289–294 (2022).
24. Glass, D. S. & Riedel-Kruse, I. H. A Synthetic Bacterial Cell-Cell Adhesion Toolbox for Programming Multicellular Morphologies and Patterns. *Cell* **174**, 649–658.e16 (2018).
25. Molinari, S. *et al.* A de novo matrix for macroscopic living materials from bacteria. *Nat. Commun.* **13**, 5544 (2022).
26. Bharat, T. A. M. *et al.* Structure of the hexagonal surface layer on *Caulobacter crescentus* cells. *Nat. Microbiol.* **2**, 17059 (2017).
27. Jose, J. & Meyer, T. F. The autodisplay story, from discovery to biotechnical and biomedical applications. *Microbiol. Mol. Biol. Rev. MMBR* **71**, 600–619 (2007).
28. Maurer, J., Jose, J. & Meyer, T. F. Autodisplay: one-component system for efficient surface display and release of soluble recombinant proteins from *Escherichia coli*. *J. Bacteriol.* **179**, 794–804 (1997).
29. Schüürmann, J., Quehl, P., Festel, G. & Jose, J. Bacterial whole-cell biocatalysts by surface display of enzymes: toward industrial application. *Appl. Microbiol. Biotechnol.* **98**, 8031–8046 (2014).
30. Wells, T. J. *et al.* EhaA is a novel autotransporter protein of enterohemorrhagic *Escherichia coli* O157:H7 that contributes to adhesion and biofilm formation. *Environ. Microbiol.* **10**, 589–604 (2008).
31. Kozlowski, M. T., Silverman, B. R., Johnstone, C. P. & Tirrell, D. A. Genetically Programmable Microbial Assembly. *ACS Synth. Biol.* **10**, 1351–1359 (2021).

32. Dooling, L. J. & Tirrell, D. A. Engineering the Dynamic Properties of Protein Networks through Sequence Variation. *ACS Cent. Sci.* **2**, 812–819 (2016).
33. Obana, M., Silverman, B. R. & Tirrell, D. A. Protein-Mediated Colloidal Assembly. *J. Am. Chem. Soc.* **139**, 14251–14256 (2017).
34. Rapp, P. B. *et al.* Analysis and Control of Chain Mobility in Protein Hydrogels. *J. Am. Chem. Soc.* **139**, 3796–3804 (2017).
35. Chittur, P. K. A Millifluidic Bulge Test for Multiscale Properties of Engineered Biofilms. (California Institute of Technology, 2023). doi:10.7907/e1yv-mr74.
36. ‘Rule of thumb’ for cell area (surface area) - Bacteria Escherichia coli - BNID 101792.
<https://bionumbers.hms.harvard.edu/bionumber.aspx?id=101792&ver=6&trm=surface+area+of+e+coli+cell&org=>.
37. Ford, M. J., Nomellini, J. F. & Smit, J. S-Layer Anchoring and Localization of an S-Layer-Associated Protease in *Caulobacter crescentus*. *J. Bacteriol.* **189**, 2226–2237 (2007).
38. Walker, S. G., Karunaratne, D. N., Ravenscroft, N. & Smit, J. Characterization of mutants of *Caulobacter crescentus* defective in surface attachment of the paracrystalline surface layer. *J. Bacteriol.* **176**, 6312–6323 (1994).
39. von Kügelgen, A. *et al.* In Situ Structure of an Intact Lipopolysaccharide-Bound Bacterial Surface Layer. *Cell* **180**, 348-358.e15 (2020).
40. Balaev, A. E., Dvoretzki, K. N. & Doubrovski, V. A. Refractive index of escherichia coli cells. **4707**, 253–260 (2002).
41. Kamihira, M., Taniguchi, M. & Kobayashi, T. Sterilization of Microorganisms with Supercritical Carbon Dioxide. *Agric. Biol. Chem.* **51**, 407–412 (1987).

42. The Beer-Lambert Law. *Chemistry LibreTexts*
[https://chem.libretexts.org/Bookshelves/Physical_and_Theoretical_Chemistry_Textbook_Maps/Supplemental_Modules_\(Physical_and_Theoretical_Chemistry\)/Spectroscopy/Electronic_Spectroscopy/Electronic_Spectroscopy_Basics/The_Beer-Lambert_Law](https://chem.libretexts.org/Bookshelves/Physical_and_Theoretical_Chemistry_Textbook_Maps/Supplemental_Modules_(Physical_and_Theoretical_Chemistry)/Spectroscopy/Electronic_Spectroscopy/Electronic_Spectroscopy_Basics/The_Beer-Lambert_Law) (2013).
43. Philips, R. M. & R. » How big is an E. coli cell and what is its mass?
<http://book.bionumbers.org/how-big-is-an-e-coli-cell-and-what-is-its-mass/>.
44. Tsakalakos, T. & Hilliard, J. E. Elastic modulus in composition-modulated copper-nickel foils. *J. Appl. Phys.* **54**, 734–737 (1983).
45. Hsu, F. P. K., Liu, A. M. C., Downs, J., Rigamonti, D. & Humphrey, J. D. A Triplane Video-Based Experimental System for Studying Axisymmetrically Inflated Biomembranes. *IEEE Trans. Biomed. Eng.* **42**, 442–450 (1995).
46. Mohan, D. & Melvin, J. W. Failure properties of passive human aortic tissue. II-Biaxial tension tests. *J. Biomech.* **16**, (1983).
47. Cavinato, C. *et al.* Biaxial loading of arterial tissues with 3D in situ observations of adventitia fibrous microstructure: A method coupling multi-photon confocal microscopy and bulge inflation test. *J. Mech. Behav. Biomed. Mater.* **74**, 488–498 (2017).
48. Midgett, D. E., Quigley, H. A. & Nguyen, T. D. In vivo characterization of the deformation of the human optic nerve head using optical coherence tomography and digital volume correlation. *Acta Biomater.* **96**, 385–399 (2019).
49. Tonge, T. K., Atlan, L. S., Voo, L. M. & Nguyen, T. D. Full-field bulge test for planar anisotropic tissues: Part I-Experimental methods applied to human skin tissue. *Acta Biomater.* **9**, 5913–5925 (2013).

50. Wang, L., Tian, L., Huang, Y., Huang, Y. & Zheng, Y. Assessment of Corneal Biomechanical Properties with Inflation Test Using Optical Coherence Tomography. *Ann. Biomed. Eng.* **46**, 247–256 (2018).
51. Zamprogno, P. *et al.* Mechanical properties of soft biological membranes for organ-on-a-chip assessed by bulge test and AFM. *ACS Biomater. Sci. Eng.* **7**, 2990–2997 (2021).
52. O’Connell, P. A. & McKenna, G. B. Novel nanobubble inflation method for determining the viscoelastic properties of ultrathin polymer films. *Rev. Sci. Instrum.* **78**, 14706 (2007).
53. Turner, J. A., Menary, G. H. & Martin, P. J. Biaxial characterization of poly(ether-ether-ketone) for thermoforming: A comparison between bulge and in-plane biaxial testing. *Polym. Eng. Sci.* **59**, 1853–1865 (2019).
54. Marra, S. P., Kennedy, F. E., Kinkaid, J. N. & Fillinger, M. F. Elastic and rupture properties of porcine aortic tissue measured using inflation testing. *Cardiovasc. Eng.* **6**, 123–131 (2006).
55. Tabata, O., Kawahata, K., Sugiyama, S. & Igarashi, I. Mechanical property measurements of thin films using load-deflection of composite rectangular membranes. *Sens. Actuators* **20**, 135–141 (1989).

Chapter 4

Quantitative Real-Time Analysis of Living Materials by Stimulated Raman Scattering Microscopy

1. Abstract

Composite materials built in part from living organisms have the potential to exhibit useful autonomous, adaptive, and self-healing behavior. The physicochemical, biological, and mechanical properties of such materials can be engineered through genetic manipulation of their living components. Successful development of living materials will require not only new methods for design and preparation, but also new analytical tools that are capable of real-time noninvasive mapping of chemical compositions. Here we establish a strategy based on stimulated Raman scattering microscopy to monitor phosphatase-catalyzed mineralization of engineered bacterial films *in situ*. Real-time label-free imaging elucidates the mineralization process, quantifies both the organic and inorganic components of the material as functions of time, and reveals spatial heterogeneity at multiple scales. In addition, we correlate the mechanical performance of films with the extent of mineralization. This work introduces a promising strategy for quantitatively analyzing living materials, which should contribute to accelerated development of such materials in the future.

2. Introduction

In nature, bacterial cells are often found in complex biofilms, where they interact through cell adhesion, matrix secretion and quorum sensing. Biofilms provide excellent examples of “living materials” in which bacterial survival is enhanced under conditions of environmental stress. Inspired by natural biofilms, several laboratories have reported the development of engineered living materials (ELMs) that contain live cells and polymeric matrices.¹ Genetic manipulation of the constituent cells in ELMs allows control of composition, structure, growth dynamics, and cellular interactions, and provides a powerful tool for design of materials with potential applications in robotics, tissue engineering, drug delivery, etc.¹⁻⁵

To date, our understanding of ELMs has been limited by a dearth of non-destructive analytical methods that can be applied *in situ*.³ Traditional methods such as thermogravimetric analysis (TGA)⁴ lack spatial and temporal resolution. Imaging based on Fourier-transform infrared spectroscopy (FTIR)⁵ has low resolution and sensitivity, and high water background. Secondary ion mass spectrometry (SIMS)^{6,7} and electron microscopy (TEM and SEM)^{8,9} are intrusive, cannot be applied *in situ*, and have low throughput. Fluorescence microscopy offers substantial advantages, but requires labels or stains that can alter sample behavior.^{9,10}

To address these challenges, Raman spectro-microscopy has emerged to target specific vibrational modes and visualize the distribution of selected molecules and structures within living cells and macromolecular scaffolds.¹¹ In particular, nonlinear stimulated Raman scattering (SRS) microscopy (**Fig. 4.1a**) retains the advantages of conventional spontaneous Raman imaging while achieving improved spatial and temporal resolution,

significantly higher sensitivity (below millimolar), faster imaging throughput (up to video rate), and deeper sample penetration (up to $\sim 10^2$ μm).¹²⁻¹⁴ The spectral resolvability of SRS microscopy allows fine structural analysis of target materials, and can reveal changing compositions, bonding conditions, conformations, and details of the extracellular microenvironment.¹⁵ The linear dependence of SRS intensity on target concentration enables highly desirable quantitative analysis.¹⁶ Therefore, SRS imaging presents an ideal combination of features for non-intrusively and quantitatively analyzing the components of ELMs, allowing real-time observation of ELM growth and the investigation of functional connections between the properties of materials and their chemical, structural and morphological characteristics, paving the way for high-throughput materials screening. The fast feedback provided by SRS microscopy also helps form and test hypotheses that can inspire and accelerate imaging-guided design of new ELMs.

Here, we report the use of SRS microscopy to track and quantify phosphatase-catalyzed mineralization of engineered bacterial systems *in situ*. We first established SRS spectral-imaging as an effective tool to benchmark bacterial mineralization levels in both single cells and bacterial films. Applying this tool to ELM design, we tested the hypothesis that the mechanical performance of mineralized biofilms is determined by two factors: (1) the concentration of the inorganic component; and (2) the spatial distribution of the organic (living cells) and inorganic (scaffolds or matrices) components. By combining SRS imaging-analysis and hydraulic bulge tests, we successfully correlated the mechanical performance of the mineralized biofilms with their inorganic-to-organic ratios. We observed that the biofilms exhibit Young's moduli of tens of kPa and can endure relatively large strains (≥ 0.1) at early mineralization

stages, and that moduli and elongation behavior can be tuned through control of the inorganic-to-organic ratio. All these changes were observed within minutes of initiating mineralization. This study illustrates the value of *in situ* SRS imaging in accelerating ELM analysis, design and development.

3. Results and Discussions

3.1 Analysis of alkaline phosphatase (PhoA)-catalyzed calcium phosphate formation by in situ SRS imaging

Scaffolds based on bioceramics such as calcium phosphates are preferred candidates for medical implants.¹⁷ To explore the integration of bioceramics into ELMs, we employed a bacterial mineralization system based on a modified version of the well-known phosphatase PhoA.¹⁸ Three engineered variants of *Escherichia coli* strain DH10B were examined: PhoA, E6/PhoA and Triblock/PhoA. All of them contain a plasmid that carries a gene encoding PhoA under control of an arabinose-inducible promoter, with an N-terminal leader peptide that guides the enzyme to the periplasm (**Fig. 4.1a**, sequence design in **Fig. S4.1**). Two of the variants have an additional plasmid that encodes constitutive expression of a surface display protein (**Fig. 4.1a**, sequence design in **Fig. S4.1**). E6/PhoA's surface protein has six repeats of an Elastin-like peptide (E, 25-aa). Triblock/PhoA's surface protein has three E3 domains spaced by two copies of a 16-aa peptide sequences known to mediate calcium phosphate mineralization.¹⁹ Upon induction, all three variants gain periplasmic phosphatase activity, which converts organic phosphates into inorganic phosphate (**Fig. 4.1b**). When the cells are cultured in buffer supplemented with calcium glycerophosphate (CGP), PhoA converts glycerophosphate to phosphate anion and thereby initiates formation of calcium phosphate minerals (which we designate bio-calcium phosphate,

BCP) (**Fig. 4.1b**). Because PhoA resides in the periplasm, we expect mineralization to be confined primarily to the periplasm and cell surface.

In a typical *in situ* SRS imaging setup for probing PhoA-catalyzed calcium phosphate formation, two spatially and temporally overlapped pulsed laser beams, pump and Stokes, are sent into a confocal-type microscope and focused on the sample (**Fig. 4.1a**, left). When the energy difference between the pump and Stokes laser photons matches the vibrational frequency of target chemical bonds (e.g. the phosphate bonds from BCP, **Fig. 4.1c**), those bonds are efficiently driven from the vibrational ground state to the corresponding vibrational excited state, creating stimulated Raman loss in the pump beam, which is subsequently detected by a photodiode (**Fig. 4.1a, c**). Series of chemical maps can then be efficiently generated by raster-scanning the laser focus throughout the samples in 3D.

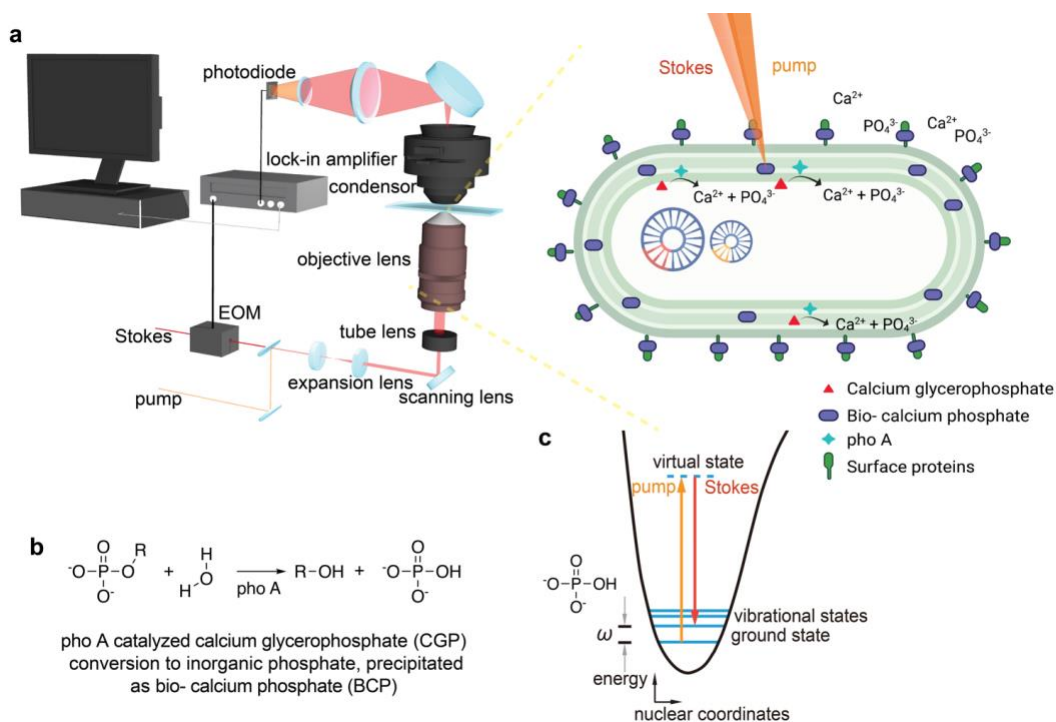


Figure 4.1. Label-free tracking of the engineered *E. coli* bacterial mineralization. **a**, Schematics of the stimulated Raman scattering (SRS) imaging setup and an engineered *E. coli* cell for biomineralization. The *E. coli* cell was engineered to carry two kinds of plasmids. One plasmid carries a gene encoding bacterial phosphatase pho A, an enzyme naturally expressed in periplasm of *E. coli*, that converts organic phosphate into inorganic phosphate anion. The other plasmid carries a gene encoding surface-expressing bacterial protein, which are rich in acidic amino acid residue glutamic acid and peptide sequence known to mediate calcium phosphate mineralization. When the cell was treated with calcium glycerophosphate, the pho A in the periplasm would convert glycerophosphate into phosphate anion and thus initiate mineralization of calcium phosphate. Since surface of the bacterium has protein that binds to calcium cation and calcium diffusion into the cytosol is limited, the mineralization would be spatially controlled at periplasm and cell surface. **b**, Enzyme pho A catalyzed conversion of calcium glycerophosphate (CGP) into bio-calcium phosphate (BCP). Enzyme pho A hydrolyzes the phosphoester bond between the organic group and phosphate, releasing an alcohol and an inorganic phosphate anion. The catalytic nature of pho A ensures rapid generation of phosphate and fast mineralization. **c**, Energy scheme of the phosphate vibrational modes probed by SRS microscopy. The SRS signal is detected when the energy difference between the pump photons and the Stokes photons matches the frequency of the vibrational mode of phosphate (ω).

3.2. Raman characterization and SRS imaging of *E. coli* mineralization

Because the phosphate vibrational frequency varies among common forms of calcium phosphate, we first used spontaneous Raman spectroscopy to identify the Raman signals characteristic of BCP (**Fig. 4.2a**, blue): the most distinctive band is at 961 cm^{-1} , which we assign to the ν_1 symmetric stretching mode of PO_4^{3-} (BCP- ν_1 - PO_4^{3-}).^{20,21} This band is also observed for hydroxyapatite (HA, **Fig. 4.2a**, green), suggesting structural similarity between BCP and HA. In contrast, β -tricalcium phosphate (β -TCP,

Fig. 4.2a, magenta), another form of calcium phosphate widely used in bioceramic implants, presents its own unique spectrum with clear splitting in the frequency region of the PO_4^{3-} symmetric stretching. The peaks at 949 cm^{-1} and 970 cm^{-1} reflect significant differences in the intratetrahedral P-O bond lengths for different nonequivalent PO_4^{3-} ions of the β -TCP structure.²¹ These results indicate that the mineral precipitated through the action of PhoA is a carbonate-free non-stoichiometric HA rather than β -TCP, consistent with previous reports.¹⁸ The fact that the ν_1 symmetric stretching mode of PO_4^{3-} is absent from the spectrum of the substrate CGP (CGP, **Fig. 4.2a**, red) enables clear distinction between substrate (CGP) and product (BCP) in the course of SRS imaging and tracking of the mineralization process.

We next obtained the SRS hyper-spectrum from a BCP sample (**Fig. 4.2b**) and verified that the characteristic SRS band at 961 cm^{-1} could be detected. We then employed SRS microscopy to capture the spatial distribution of BCP- ν_1 - PO_4^{3-} (denoted as phosphate, 961 cm^{-1}) in live *E. coli* cells subjected to mineralization conditions (**Fig. 4.2c**). Consistent with our expectation that mineralization should occur near the periplasm and cell surface, SRS images of mineralized bacteria revealed clear core-shell structures associated with individual cells, indicating that each cell is wrapped in a mesh of calcium phosphate (**Fig. 4.2c**). These results are consistent with scanning electron microscopy (SEM) and transmission electron microscopy (TEM) images of the corresponding samples (**Fig. 4.2d-e**). Notably fluorescence microscopy images (**Fig. S4.2**) of calcein-stained samples suffer from high background and non-specific staining, which precluded quantitative analysis.

Once a standard workflow for SRS imaging of mineralized bacterial films was established, we undertook *in situ* time-lapse tracking of the *E. coli* mineralization process. We first demonstrated tracking at the single cell level by analysis of *E. coli* liquid cultures. Cells were suspended in a nutrient-free HEPES buffer (pH=7.4) containing CGP as substrate and diluted to an appropriate optical density (details in Materials and Methods). Time-lapse images of single cells over the course of 2 h of mineralization showed an increase in the phosphate-channel SRS intensity (**Fig. 4.2f**) with cell-to-cell heterogeneity in the extent of mineralization (**Fig. 4.2g**), showing a difference up to 50% at early stages. By taking advantage of the proportionality between the SRS signal intensity and the concentration of BCP, we determined that the amount of phosphate deposited could triple or quadruple between 30 and 120 min of mineralization (**Fig. 4.2g**). After 2 h, the mineralization process slows, indicating that it is close to completion. To our knowledge, this is the first report of visualization of such rapid mineralization in a label-free and non-destructive way in a bacterial system.

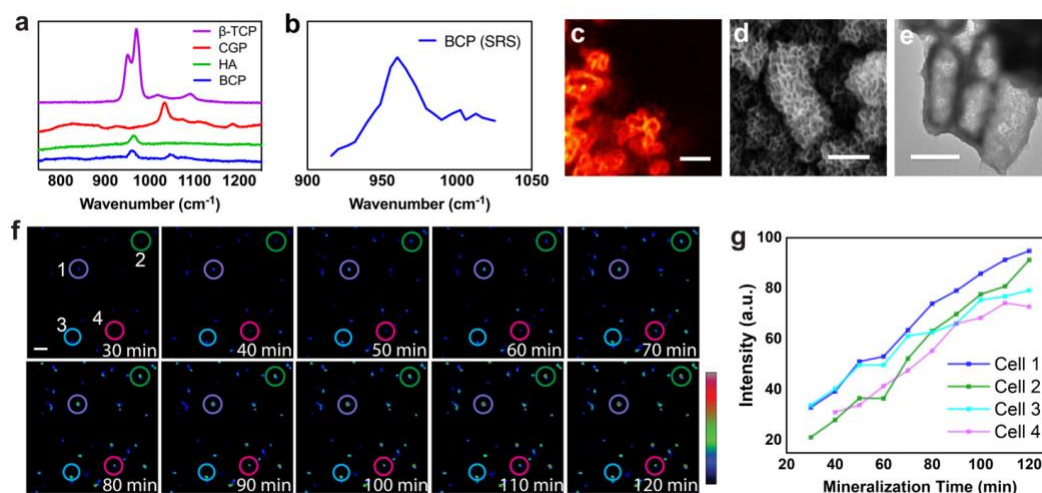


Figure 4.2. SRS imaging and real-time tracking of *pho A* catalyzed mineralization in *E. coli* cells. **a**, Spontaneous Raman spectra of the various forms of phosphates: the organic precursor calcium glycerophosphate (CGP, red), β -tricalcium phosphate (β -TCP, purple), hydroxyapatite (HA, green), and bio- calcium phosphate formed by bacterial mineralization (BCP, blue). The spectra indicated that structurally the mineralization product BCP resembled HA among all common forms of inorganic phosphates. **b**, The SRS spectrum of BCP showing the characteristic phosphate peak at 961 cm^{-1} . **c**, an SRS image showing the phosphate formed on the surface of mineralized bacterial cells, exhibiting similar hollow structures seen in the TEM image. Scale bar, $5\text{ }\mu\text{m}$. **d-e**, SEM (**d**) and TEM (**e**) images showing mineralized bacterial cells expressing *pho A* in the periplasm are enwrapped in a mesh of calcium phosphate minerals. Scale bars, $2\text{ }\mu\text{m}$ (**d**) and $1\text{ }\mu\text{m}$ (**e**). **f**, *In-situ* phosphate-channel SRS images of a liquid culture of *E. coli* cells during mineralization within 2 hours, showing the real-time accumulation of inorganic phosphate at single-cell level. Scale bar: $5\text{ }\mu\text{m}$. **g**, Phosphate-channel SRS intensity of arbitrarily selected four *E. coli* cells (as circled in **f**) showing an increasing trend with cell-to-cell heterogeneity.

3.3. Real-time SRS imaging of mineralization in bacterial films

To prepare bacterial films for mineralization, overnight *E. coli* cultures in Luria-Bertani (LB) media were dropped on polycarbonate membrane filters with $0.2\text{ }\mu\text{m}$ diameter pores and vacuum filtered. Filters were transferred to fresh LB agar plates containing suitable antibiotics daily for six days to allow proliferation and constitutive expression of surface-displayed proteins and then moved to LB agar plates with suitable antibiotics and 0.1% L-arabinose for one day to induce expression of PhoA. The bacterial films and supporting filters were then immersed in mineralization buffer containing CGP for periods of a few hours to 24 h. Detailed procedures used for bacterial film growth and mineralization can be found in Materials and Methods. After 24 h, mineralized films

were stiff and tough enough to be peeled off their filter supports for imaging and analysis (**Fig. 4.3a**, **Fig. S4.3**).

SRS images of mineralized bacterial films recorded at 961 cm^{-1} (phosphate, **Fig. 4.3c**) and at 2940 cm^{-1} (CH_3 , **Fig. 4.3d**), and fluorescence images of calcein-stained films (**Fig. 4.3b**) showed co-localization of phosphate ions, *E. coli* cells and calcium ions, respectively, confirming the utility of SRS imaging of mineralized samples. It is worth noting that 961 cm^{-1} signals in SRS images of calcein-stained samples were much weaker than those derived from unstained samples (**Fig. 4.3c** vs **Fig. 4.3e** at 105 min). This difference was due to a competing reaction during fluorescence staining: dissolution of inorganic phosphate occurs as the calcein-AM dye chelates calcium cations and replaces the phosphate anions. This effect was also evident in images of isolated cells (**Fig. S4.4**), illustrating the value of imaging methods that do not rely on stains.

To visualize the dynamics of mineralization in bacterial films by SRS, *E. coli* films were grown and induced as above, then transferred to a sealed imaging chamber and immersed in mineralization buffer (**Fig. 4.3a(3)**). Time-lapse SRS images were recorded every 10 min with an acquisition time of 8.6 s/frame in the phosphate channel (961 cm^{-1}) (**Fig. 4.3e**). A clear increase in the phosphate intensity indicated a rapid rise in the mineralization level over the course of 105 min (**Fig. 4.3f**, intensities recorded from the areas circled in yellow in **Fig. 4.3e** to avoid intensity heterogeneity from the edge to the center of the film). The rate of mineralization is remarkably high in comparison to previous reports in which mineral deposition occurred over periods ranging from days to weeks. (10, 18, 19)

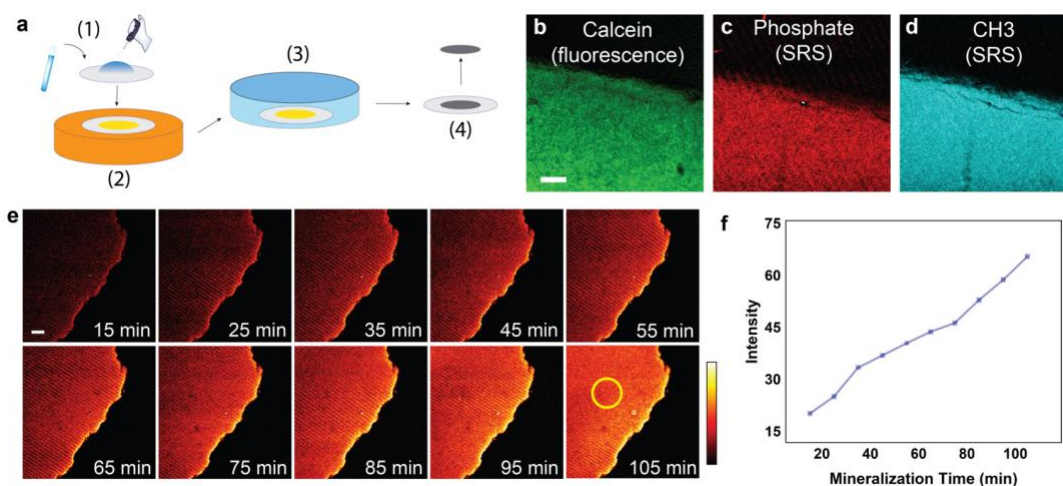


Figure 4.3. SRS imaging and real-time tracking of *E. coli* bacterial film mineralization. **a**, Preparation of a typical bacterial film (growth and mineralization). (1) Overnight *E. coli* culture inoculated in LB media was dropped on polycarbonate membrane filter with 0.2 μm diameter pores and vacuum filtrated. (2) The membrane filter carrying bacteria was transferred to LB agar plate containing suitable antibiotics and inducer and grew for several days to allow surface-display protein and *pho A* to express. (3) The mature film on polycarbonate filter would be immersed in mineralization buffer containing calcium glycerophosphate from few hours to one day. (4) The mineralized film, being hard and self-standing, can be peeled from polycarbonate filter for imaging and analysis. **b-d**, Microscopy images of a typical mineralized *E. coli* biofilm: fluorescence image, calcein stained (**b**), SRS image, phosphate channel (**c**), and SRS image, CH_3 channel (**d**). Scale bar, 25 μm . **e**, *In-situ* phosphate-channel SRS images of a typical *E. coli* biofilm during mineralization within 105 minutes, showing the real-time accumulation of inorganic phosphate in films. Scale bar, 20 μm . **f**, Phosphate-channel SRS intensity of an arbitrarily selected region during mineralization in the *E. coli* biofilm.

3.4. Morphology of mineralized biofilms

SRS microscopy allows the recording of time-lapse images of phosphate deposition even in the early stages of bacterial mineralization, owing to its high sensitivity and good temporal resolution. In addition, the fine spatial resolution of SRS microscopy provides insight into the morphological characteristics of mineralized films and the relations between structure and properties. With that objective in mind, we first benchmarked the morphology of unmineralized films by label-free imaging in the organic channel (**Fig. 4.4a-b**, CH_3 , different cross-section views). We then prepared mineralized films based on *E. coli* strains that displayed different cell-surface proteins that we anticipated would modulate mineral deposition and mechanical properties.

Inspired by previous work of Prieto *et al* (19), we examined the role of cell-surface polypeptides in controlling the structures and properties of mineralized bacterial films. We prepared three types of *E. coli* cells (shown schematically in **Fig. 4.4c**): (i) one free of surface-displayed polypeptides (PhoA, described above), (ii) a second that displays E6 peptides (E6/PhoA), and (iii) a third with surface expressed triblock peptides (triblock/PhoA). The E6 peptide contains six 25-residue elastin-like repeats (**Table S4.2**) (5) and facilitates intercellular adhesion. When bacterial cells display E6 at the surface, they aggregate, forming clusters and precipitating out of the culture medium. They also form cohesive soft films due to intercellular adhesion. The E6 peptides contain glutamic acid residues that can bind to Ca^{2+} and serve as potential nucleation sites for calcium phosphate. The triblock peptide also contains nucleation sequences known to facilitate calcium phosphate mineralization (19). Compared with E6, the triblock peptide appears to cause weaker intercellular adhesion. Films grown from bacterial cells that displayed the triblock peptide exhibited reduced mechanical strength and were less cohesive than E6 films since triblock peptide doesn't tend to self-associate compared to E6 and doesn't generate aggregates as strongly as E6 in planktonic culture. (**Fig. S4.5**). Parallel 3D volume SRS images of both the organic component (cells, CH_3 channel, **Fig. 4.4d/g/j**) and the inorganic component (calcium phosphate, phosphate channel, **Fig. 4.4e/h/k**) were acquired for bacterial film samples from all three constructs. Excellent spatial co-localization was seen for cells and deposited phosphate materials. Cross-sectional views are presented in **Fig. 4.4f/i/l**.

We found clear differences in film morphology among the three engineered strains. The PhoA strain (**Fig. 4.4d-f**) yielded sparse distributions of both cells and phosphate materials, with spatially detached cells arrayed across the film. The triblock/PhoA

construct (**Fig. 4.4j-l**) exhibited a different type of heterogeneity. Larger blocks of materials, apparently formed by small aggregates of cell/phosphate hybrid structures, made the film heterogeneous and coarse in texture, especially near the surface, where roughness was observed ubiquitously. In contrast, in the E6/PhoA (**Fig. 4.4g-i**) construct, cells and phosphate were distributed more homogeneously. We believe that in this case E6 proteins displayed at the cell surface act as intercellular adhesives that bind the cells, forming a compact and dense structure, which was maintained during the mineralization process. SEM images (**Fig. S4.6**) and calcium-dependent fluorescence images (**Fig. S4.7**) yielded similar results, confirming the morphological differences among the three types of films. We also found that the surface protein influenced cell viability within the film during late-stage mineralization (**Fig. S4.8**, characterized as colony forming units (CFUs) per unit area). Unmineralized films of PhoA, E6/PhoA and triblock/PhoA started at 10^6 CFU/mm²; this value remained nearly unchanged during the first hour of mineralization. After 1 h, however, the CFU per unit area started to decline slowly for all three types of films. After 2 h, E6/PhoA samples contained roughly 10^5 CFU/mm² with a minor decrease of cell viability, while triblock/PhoA samples dropped to 10^4 CFU/mm², signaling a more substantial loss of viability.

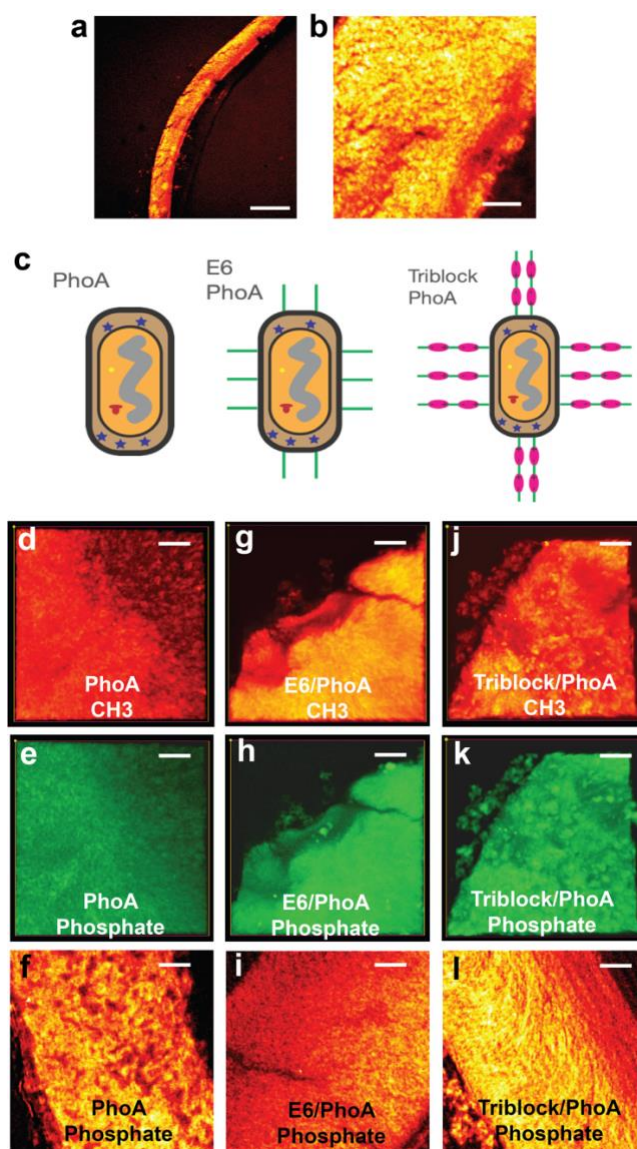


Figure 4.4. SRS images of *E. coli* biofilms with different surface protein constructions. **a-b**, Cross-sectional views of a typical unmineralized *E. coli* biofilm at different magnifications. **c**, Three types of engineered *E. coli* cells with different surface constructions: bare surface type (PhoA), with surface expressed E6 peptides (E6/PhoA) and with surface expressed Triblock peptides (Triblock/PhoA). Detailed sequence information of E6 and Triblock peptides are included in supplementary data. **d-f**, SRS images of a PhoA-type *E. coli* biofilm: CH₃ channel, axial-view of 3D volume image (d), phosphate channel, axial-view of 3D volume image (e) and phosphate channel, cross-sectional view (f). The PhoA-type *E. coli* biofilms exhibit heterogeneous spatial distribution of organic and inorganic materials, showing individual cells clearly. **g-i**, SRS images of a E6/PhoA-type *E. coli* biofilm: CH₃ channel (g), phosphate channel (h) and phosphate channel, cross-sectional view (i). The E6/PhoA-type *E. coli* biofilms exhibit more homogeneous spatial distribution of phosphate. **j-l**, SRS images of a Triblock/PhoA-type *E. coli* biofilm: CH₃ channel (j), phosphate channel (k) and phosphate channel, cross-sectional view (l). The Triblock/PhoA-type *E. coli* biofilms exhibit heterogeneous spatial distribution of organic and inorganic components with clear surface roughness. Scale bars: **a**, 100 μm ; **b, d-l**, 10 μm .

3.5 Correlating biofilm mechanical properties with phosphate levels quantified by SRS

A central objective of this work was to explore the role of mineralization in increasing the stiffness of engineered bacterial films. The morphological differences observed by SRS microscopy led us to anticipate a range of mechanical properties in the three bacterial strains described in the preceding section. We noticed immediately, when handling biofilms at different stages of mineralization, that there were readily discernible differences in mechanical properties among the strains. We then undertook a systematic study of mechanical behavior as a function of the extent of mineralization, in which we performed parallel SRS imaging and hydraulic bulge testing experiments on film samples exposed to mineralization conditions for periods of time ranging from 20 to 120 min.

We used the molar phosphate/CH ratio in each sample determined by SRS imaging to characterize the extent of mineralization. These molar ratios could be achieved by calculations based on the SRS intensities in the phosphate and CH channels, and the known Raman cross sections of phosphate P-O bond and C-H bond vibrations (details in **Supplementary Note 4.4** and **Table S4.3**).

Films were mounted in a fluidic device and subjected to a bulge/inflation test; deformation was recorded by optical coherence tomography (OCT) imaging (**Fig. S4.9**, details in **Supplementary Note 4.4**). True stress- true strain curves were constructed for each film assuming membrane deformation. Young's modulus was calculated using the initial linear portion of each curve (**Fig. 4.5a-c**, middle column, and **Fig. S4.10**).

Notably, the E6/PhoA construct (**Fig. 4.5b**) exhibited marked increases in stiffness as mineralization proceeded; unmineralized E6/PhoA films were soft, exhibiting Young's moduli of tens of kilopascals (kPa). Upon initial mineralization (20-30 min) the Young's modulus increased by as much as to two orders of magnitude. Films exposed to mineralization conditions for less than 40 min exhibited yielding behavior and eventual film failure, behavior that was absent at longer mineralization times within the limits of stress imposed by our tests. Compared to the free PhoA (**Fig. 4.5a**) and the triblock/PhoA constructs (**Fig. 4.5c**), E6/PhoA biofilms (**Fig. 4.5b**) exhibited a 4- to 5-fold enhancement in Young's modulus (**Fig. 4.5a-c**, right column). Notably, SRS quantification showed that marked changes in the mechanical behavior of E6/PhoA films required only modest levels of mineralization. For example, after only 20 min of mineralization, the molar ratio of phosphate/CH was less than 10% for biofilms with the PhoA and E6/PhoA constructs; nevertheless, the Young's moduli of the films increased from the kPa level to the MPa level, indicating at least a 100-fold increase in stiffness. The result suggests that even a relatively small change in the inorganic matrix content can change the mechanical properties of biofilms dramatically (**Fig. 4.5d**).

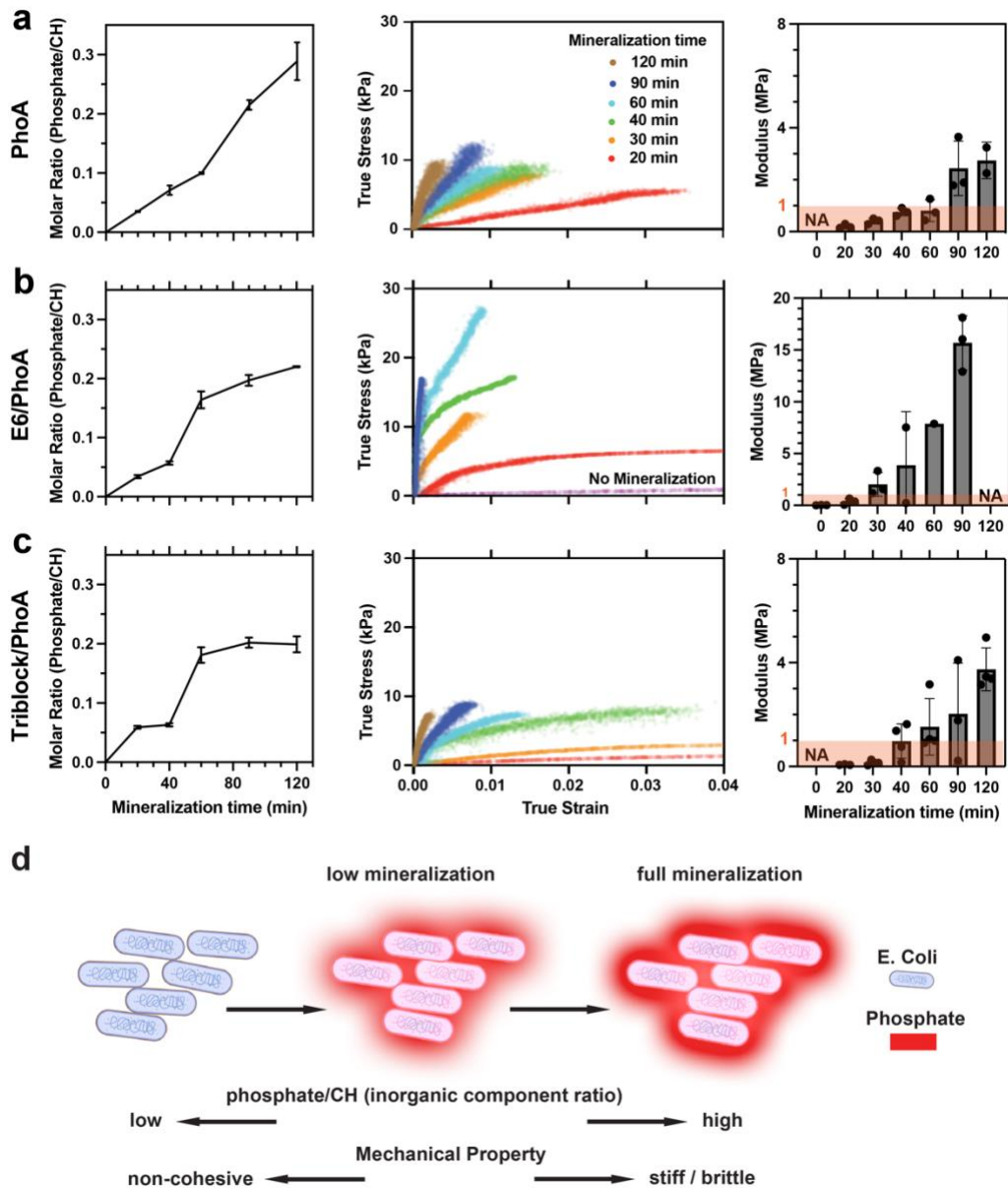


Figure 4.5. Inorganic phosphate levels and mechanical properties of *E. coli* biofilms during mineralization. a-c, Parallel studies on three types of biofilms, based on PhoA (a), E6/PhoA (b), and the Triblock/PhoA (c) constructs, during 2-hour mineralization, showing increasing molar ratios of phosphate/CH (left column), clear transitions in stress-strain relations (center column), and moduli calculated from the stress-strain data (right column). PhoA and Triblock/PhoA films transitioned from non-cohesive at 0 min to cohesive during the mineralization process, while E6/PhoA films transitioned from cohesive soft yielding films into stiff non-yielding films in the end. After 2 hrs of mineralization E6/PhoA films became stiff and brittle, which cannot be picked up. Therefore, the data point at 120 min was not achievable. Moduli of the biofilms during mineralization increased while exhibiting larger variances. d, Proposed schematics showing the relations between phosphate level and mechanical properties of the biofilms according to the observations from handling the films.

4. Conclusions

In this report, we demonstrate the utility of SRS microscopy for quantitative investigation of engineered living materials, specifically for *in situ* tracking of rapid mineralization of bacterial systems. By correlating quantitative SRS imaging and mechanical testing data, we have gained new insight into the structural origins of the mechanical behavior of mineralized bacterial films, exhibiting an imaging-guided design strategy of engineered living materials. In quest of an optimally performing *E. coli* - calcium phosphate hybrid film, we found especially striking increases in the moduli of films bearing the E6 surface protein even at modest levels of mineralization (less than 10% in terms of the phosphate-to-CH molar ratio). This molar ratio of around 10% represents a sweet spot of mineralization level that led to a mechanically superior hybrid biomaterial. We also discovered that different surface proteins yielded different mineralization morphologies, which exhibited different mechanical behaviors at comparable mineralization levels. More generally, we illustrate the value of combining microscale morphological information, quantitative chemical imaging, and mechanical testing in the analysis and design of engineered living materials.

5. Materials and Methods

Bacterial Strains. All mineralization experiments were conducted in *E. coli* strain DH10B (Invitrogen, Carlsbad, CA). Details of reagents, cloning and protein expression experiments can be found in **Table S4.1** and **Supplementary Notes 4.1-2**.

Preparation of Bacterial Films. Individual colonies harvested from LB plates were grown overnight to stationary phase in liquid LB medium supplemented with 100 mg/L ampicillin and 25 mg/L chloramphenicol to maintain plasmid stability. The resulting cultures were then diluted to an optical density at 600 nm (OD₆₀₀) of approximately 0.8. Diluted cultures were loaded on UV-sterilized track-etched polycarbonate filters (Nuclepore Whatman, 0.2 µm pore size) mounted in vacuum filter units (Nalgene Rapid-flow Thermo-Fisher). For 2.5 cm diameter polycarbonate filters, 200 µL culture volumes were loaded; 2 mL volumes were loaded on 4.7 cm diameter filters. After filtration was complete, filters were transferred to fresh LB plates. Bacterial films were grown in a 37 °C incubator. Filters were moved to fresh LB agar plates containing suitable antibiotics every day for 6 days. On the seventh day the filters (and supported biofilms) were moved to a special LB plate containing 100 mg/L L-arabinose (Sigma-Aldrich) for 1 day to induce expression of PhoA.

Mineralization of Planktonic Bacterial Cultures. Overnight *E. coli* cultures were diluted 100-fold and grown to OD₆₀₀ of 0.4–0.6 prior to induction with 0.1% L-arabinose. Expression was allowed to proceed for 90 min, after which the culture was centrifuged and resuspended in 20 mM HEPES buffer (pH 7.4) containing 10 mM calcium glycerophosphate. The detailed buffer recipe is documented in **Supplementary Note 4.3**. Mineralization was allowed to proceed for at least 1 h under

shaking at 250 rpm until cells precipitated as white clusters. Clusters were resuspended and a 3 μ L aliquot of resuspended mineralized cells was transferred to a plastic chamber (120 μ m depth, Thermo-Fisher) sandwiched between a glass slide and a cover slip for Raman microscopy.

***In situ* imaging of Mineralization of Planktonic Bacterial Cultures.** Overnight cultures of *E. coli* were diluted 100-fold and grown to OD₆₀₀ of 0.4–0.6 prior to induction with 0.1% L-arabinose. Expression was allowed to proceed for 90 min, after which the culture was centrifuged and resuspended in 20 mM HEPES buffer (pH 7.4) containing 40 mM calcium glycerophosphate. A 3 μ L volume of resuspended cells was immediately pipetted into a 120 μ m thick plastic chamber (Thermo-Fisher) sandwiched between a glass slide and a cover slip coated with poly-L-lysine (Neuvitro Corporation) for Raman microscopy. No shaking was involved in this mineralization experiment. The experiments were performed under static conditions.

Full Mineralization of Bacterial Films. Bacterial films were prepared as described in the above sections and transferred on their polycarbonate filters to a 6-well plate (Falcon) with each well filled with 5 mL of 20 mM HEPES buffer (pH 7.4) containing 10 mM calcium glycerophosphate. Four 3 mm diameter glass beads were placed at the edge of each polycarbonate filter to keep the films flat during the mineralization process. To achieve full mineralization, films remained in mineralization buffer for 24 h.

Microtomy of Fully-Mineralized Bacterial Films. Fully-mineralized films were removed from the mineralization buffer, washed with 5 mL of 20 mM HEPES buffer for 5 min and then cut with a 6 mm diameter biopsy punch (Miltex). The circular section

of film was embedded in Tissue-Tek® resin (Sakura) and frozen at - 20 °C overnight. The frozen piece was microtomed at – 20 °C with each section of 50 µm thickness. Microtomed sections were placed either on glass slides (for Raman microscopy) or on Al stubs (for SEM imaging).

Time-Dependent Mineralization of Bacterial Films. Bacterial films were prepared as described in the above sections. Films prepared on 4.7 cm diameter polycarbonate filters were cut with a razor blade into seven pieces of nearly identical size. One piece was used as an unmineralized control sample. Other pieces were transferred to 6-well plates (Falcon) with each well filled with 5 mL of 20 mM HEPES buffer (pH 7.4) containing 30 mM calcium glycerophosphate. At time points of 20, 30, 40, 60, 90 and 120 mins, pieces of film were removed from mineralization buffer and placed in another 6-well plate with each well containing 5 mL 20 mM HEPES buffer to stop mineralization. These samples were used to determine mechanical properties and extent of mineralization by bulge testing and quantitative Raman microscopy, respectively.

Spontaneous Raman Spectroscopy Spontaneous Raman spectra were acquired using an upright confocal Raman spectrometer (Horiba Raman microscope; Xplora plus). A 532 nm YAG laser is used to illuminate the sample with a power of 12 mW on sample through a 100×, N.A. 0.9 objective (MPLAN N; Olympus). Raman shift ranges from 690 to 1300 cm^{-1} was acquired to cover the Raman peaks of interest (characteristic of Phosphate species). Data acquisition was performed with 10 s integration by the LabSpec6 software. Spontaneous Raman spectra were organized and presented by Excel and GraphPad, respectively.

Stimulated Raman Scattering (SRS) Spectroscopy and Microscopy. A picoEmerald laser system (Applied Physics & Electronics) was used as the light source for SRS microscopy. This system produces 1.8 ps pump (tunable from 770 nm – 990 nm, bandwidth 0.5 nm, spectral bandwidth $\sim 7 \text{ cm}^{-1}$) and Stokes (1031.2 nm, spectral bandwidth 10 cm^{-1}) beams with 80 MHz repetition rate. The Stokes beam is modulated at 20 MHz by an internal electro-optic modulator. The spatially and temporally overlapped pump and Stokes beams are introduced into an inverted multiphoton laser scanning microscope (FV3000, Olympus), and then focused onto the sample by a 25X water objective (XLPLN25XWMP, 1.05 N.A., Olympus) for imaging. Transmitted pump and Stokes beams are collected by a high N.A. condenser lens (oil immersion, 1.4 N.A., Olympus) and pass through a bandpass filter (893/209 BrightLine, 25 mm, Semrock) to filter out the Stokes beam. A large area ($10 \times 10 \text{ mm}$) Si photodiode (S3590-09, Hamamatsu) is used to measure the pump beam intensity. A 64 V reverse-bias DC voltage is applied on the photodiode to increase saturation threshold and reduce response time. The output current is terminated by a $50\text{-}\Omega$ terminator and pre-filtered by a 19.2-23.6-MHz bandpass filter (BBP-21.4+, Mini-Circuits) to reduce laser and scanning noise. The signal is then demodulated by a lock-in amplifier (SR844, Stanford Research Systems) at the modulation frequency. The in-phase X output is fed back to the Olympus IO interface box (FV30-ANALOG) of the microscope. Image acquisition speed is limited by the $30 \text{ }\mu\text{s}$ time constant set for the lock-in amplifier. Correspondingly, we use an $80 \text{ }\mu\text{s}$ pixel dwell time, which gives a speed of 21s per frame for a 512-by-512-pixel field of view. The pump laser is tuned to 938.3 nm for imaging the phosphate vibrational mode at 961 cm^{-1} . Laser powers on sample are measured to be 30 mW for the pump beam and 200 mW for modulated Stokes beam. 16-bit grey scale images are acquired by Olympus Fluoview 3000 software. Volumetric

images were acquired by collecting a z-stack with a step size of 1 micron in the z-direction. SRS spectra were acquired by fixing the stokes beam at 1031.2 nm and scanning the pump beam through the designated wavelength range point by point. SRS spectra were processed and presented by Excel and GraphPad.

Sample Mounting and Imaging. Cell or biofilm samples were kept in HEPES buffer for imaging. Grace Bio-Labs SecureSeal™ spacers with appropriate opening sizes were used as spacers between microscope slides (1 mm, VWR) and coverslips (12 mm, #1.5, Fisher). Confocal images were obtained by the Olympus FluoView™ FV3000 confocal microscope with the SRS setup described above.

Bulge Test and Mechanical Characterization. A millifluidic device was constructed using laser cut acrylic sheets to adapt the bulge test to the Pa-kPa pressures needed to deform the biofilms. The final device construct consisted of a sealed central chamber housing the biofilm sample as a 3 mm diameter disk, sandwiched between two washer-shaped supports. Each face of the sample was exposed to a chamber filled with HEPES buffer whose hydrostatic pressure could be independently controlled. Thus, by applying different hydrostatic pressures to the top and bottom faces of the biofilm, the film could be “inflated” through the washer aperture into a dome-like shape. Hydrostatic pressures were applied across the film by varying the height of HEPES in two separate reservoirs connected to external ports in the device. The reservoirs themselves were 60 ml syringes of known internal diameter (BD Scientific, ID = 26.72 mm, cross sectional area 5.61 cm²). Thus, the addition of 858 μ l of HEPES buffer increased the reservoir level by 1.53 mm, which increased the hydrostatic pressure on the corresponding face of the sample by 15.0 Pa (density assumed constant at 1 g/ml). Prior to mechanical

testing, a bacterial film with its polycarbonate support was submerged in HEPES buffer and a 3 mm dia. biopsy punch (Integra Biosciences) was used to gently make a circular cut through the bacterial film but not the polycarbonate. The sample support disk (copper TEM disk, 1.5 mm diameter circular aperture, 3.05 mm outer diameter, thickness 25 μm , Ted Pella) was then slid in between the bacterial film and polycarbonate and used to gently separate the film from the polycarbonate. Once the edge of the film was freed, the film freely floated away from the polycarbonate and could be loaded into the device. The device channels were then filled with HEPES and the syringe reservoirs attached via luer slip connectors threaded into the device ports. A syringe pump (KD Scientific) was used to add HEPES buffer to the reservoir connected to the bottom face of the biofilm at a flow rate of 70 ml/min with a final volume of 55 ml. The biofilm deformation was imaged using optical coherence tomography (OCT, Thorlabs, GAN210 base unit: 930 nm central wavelength, 6 μm axial resolution. OCTP-900 scan head, OCT-LK3-BB scan lens: 36 mm FL, 8 μm lateral resolution). A-Scan/Line Rate was 36 kHz (acquisition time = 19 ms). Diagram illustration of the bulge test device and mechanical properties analysis are included in **Figure S4.9** and **Supplementary Note 4.5**.

Image Processing and Data Analysis. Image color-coding, intensity profiling and intensity normalizations of the z-stacks were done by ImageJ. Intensity normalization of the z-stacks was done in ImageJ. 3D rendering of z-stacks was done in either ImageJ or Olympus cellSens. Data plotting and analysis, including spectral plots and Gaussian fitting were performed in OriginLab and Prism (GraphPad).

Fluorescence Imaging. The fluorescence images of processed samples with fluorescent labels were obtained with a 25X, 1.05 N.A. water-immersion objective with the Olympus Fluoview system. Single-photon confocal laser scanning imaging was performed with a 488-nm laser (Coherent OBIS), and in Calcein-AM Channel ($\lambda_{ex}/\lambda_{em}$: 495/515 nm). The images were visualized and analyzed with Fiji or Imaris Viewer.

Statistics and Reproducibility. For all imaging experiments yielding the micrographs reported herein, at least three independent experiments were repeated with similar results.

6. Acknowledgements.

Hanwei Liu and Dr. Chenxi Qian conceived and designed the experiments under the supervision of Professors David Tirrell and Wei Lu. Hanwei Liu was responsible for all the cell experiments, most of the sample preparation, parts of microscopy imaging and all mineralization experiments. Dr. Chenxi Qian was responsible for parts of the biofilm preparation and performed all SRS imaging and analysis. Dr. Priya Chittur performed all experiments related to the biofilm mechanical property and analysis under the supervision of Professor Julia Kornfield. Rahuljeet Chadha and Dr. Yuxing Yao performed parts of the SRS and EM imaging, respectively. The manuscript from which this chapter was adapted was written with Dr. Chenxi Qian in which Hanwei Liu and Chenxi Qian shared equal contribution and was edited by Professors David Tirrell, Lu Wei and Julia Kornfield.

7. Supporting Information.

Supplementary Note 4.1: Reagents and suppliers

Restriction enzymes, ligase, and Q5 DNA polymerase were purchased from New England Biolabs (Beverly, MA). DNA oligos and G-blocks were purchased from Integrated DNA Technologies (Coralville, IA).

Supplementary Note 4.2: Plasmid subcloning

Recombinant fusion proteins were produced by standard recombinant DNA technology. *E. coli* strain DH10B was used for all cloning steps and material preparation.

Genes encoding the autotransporter protein along with elastin solubility/stability tags have been previously cloned by our group into modified pQE-80L plasmids.²²

G-blocks encoding PhoA without its natural leader peptide were ordered with 5' BamHI and 3' HindIII sites. G-blocks were digested with BamHI and HindIII and inserted into a similarly digested pQE-Empty plasmid containing pelB leader peptide described in previous work²² to make a pelB-PhoA construct that directs PhoA to the periplasm. Using Gibson assembly, the pelB-PhoA construct was placed under control of the araBAD promoter in pBAD33.

pX-E6 containing six 25-residue elastin-like-peptide repeats reported in previous work²² was digested with BamHI and XhoI and inserted into a similarly digested pAT-Empty vector to make pAT-E6. The T5 promoter of the plasmid drives constitutive expression of protein E6-AT.

pX-ST encoding the SpyTag peptide was mutated into pX-N encoding nucleation peptide SN15 (N)²³ by PCR. Recursive ligation²⁴ was used to assemble pX-triblock peptide from pX-N and pX-E3. pX-triblock was digested with BamHI and XhoI and inserted into a similarly digested pAT-Empty vector to make pAT-triblock. The T5 promoter of the plasmid drives constitutive expression of protein triblock-AT.

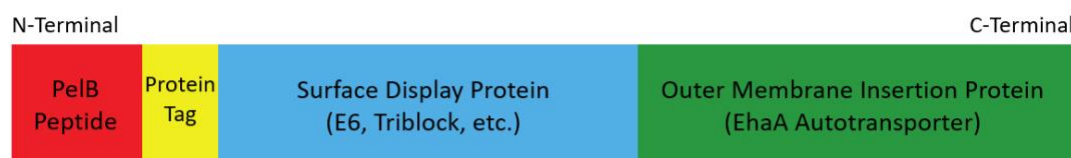
The sequence of all constructs were sequenced and confirmed by Laragen Inc. (Culver City, CA)

Supplementary Note 4.3: Buffer recipe

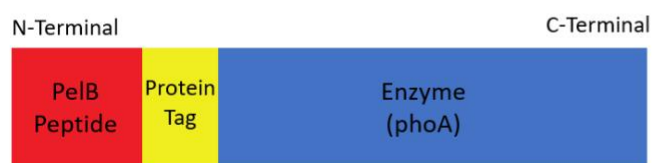
The 20 mM HEPES buffer used in this work doesn't contain any PO_4^{3-} . The buffer contains 20 mM HEPES, 115 mM NaCl, and 1.2 mM MgCl_2 buffered at pH 7.4. The mineralization buffer contains calcium glycerophosphate at concentrations ranging from 10 mM to 60 mM.

Table S4.1: Plasmids used in this study

Name	Backbone/origin/promoter	Purpose
pQE-Empty	pQE80l/colE1/T5	Empty plasmid for cloning and ampicillin resistance
pelB-PhoA	pQE80l/colE1/T5	Constitutive expression of PhoA in periplasm
pBAD-PhoA	pBAD33/p15a/araBAD	Arabinose-inducible expression of PhoA in periplasm
pAT-E6	pQE80l/colE1/T5	Constitutive expression of E6-AT protein on cell surface
pAT-Triblock	pQE80l/colE1/T5	Constitutive expression of triblock-AT surface displayed nucleation peptide
pAT-Empty	pQE80l/colE1/T5	Cloning of autotransporter fusion proteins
pX-E6	pQE80l/colE1/T5	Cloning of pAT-E6
pX-E3	pQE80l/colE1/T5	Cloning of pAT-triblock
pX-ST	pQE80l/colE1/T5	Cloning of pAT-triblock
pX-N	pQE80l/colE1/T5	Cloning of pAT-triblock



Autotransporter Fusion protein



Periplasm enzyme

Fig. S4.1. Protein sequence design of autotransporter fusion protein and periplasmic enzyme. The N-terminal pelB leader peptide directs the translated protein into the periplasm of *E. coli* and is then cleaved from the protein. The C-terminal autotransporter sequence is recognized and inserted into the outer membrane of *E. coli* while the N-terminal part is displayed at the cell surface. PhoA is transported to the periplasm. (Corresponding color code was applied to **Table S2**.)

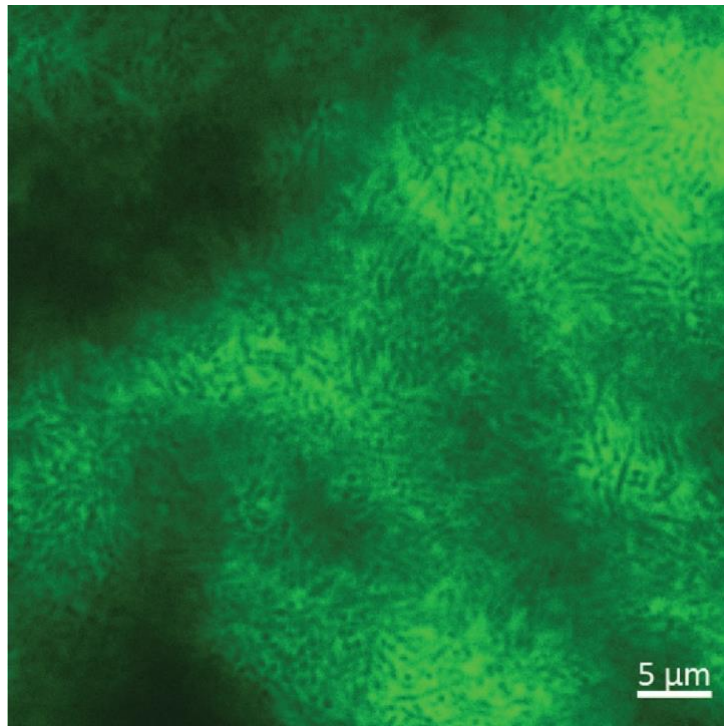


Fig. S4.2. Fluorescence microscopy image of 7 days old (1 day induction with 0.1% arabinose for PhoA expression) PhoA bacterial film expressing periplasmic PhoA after 24 hrs of mineralization in 10 mM CGP, stained by the calcium binding dye calcein. The cell interior is not stained by calcein, consistent with mineralization outside the inner membrane of bacterium. Calcein binds to calcium cation and becomes fluorescent once binds to calcium, meaning that it binds non-specifically and cannot distinguish between BCP and other molecules that contains calcium. Scale bar, 5 μm .

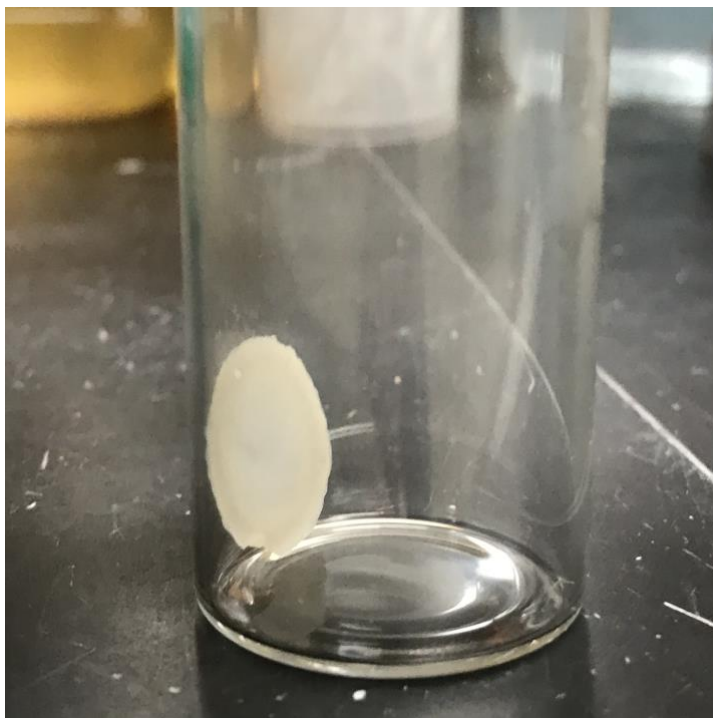


Fig. S4.3. A Triblock/PhoA bacterial film after 24 hrs of mineralization in 10 mM CGP, stiff and self-standing in a 20 mL scintillation vial, already removed from its polycarbonate filter for imaging and analysis. Diameter of the film is around 2 cm.

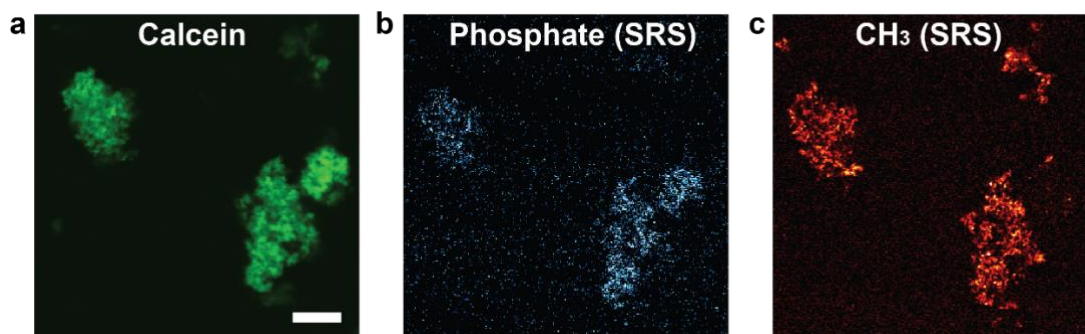


Fig. S4.4. *E. coli* cell liquid culture fully mineralized and stained by calcein (calcium tracker) and imaged by fluorescence (**a**, calcein) and SRS microscopy (**b**, phosphate channel and **c**, CH₃ channel). The phosphate channel showed weak SRS signal compared to unstained samples because phosphate anions were displaced by the calcein-AM dye which chelates calcium ions. Scale bars, 25 μm .

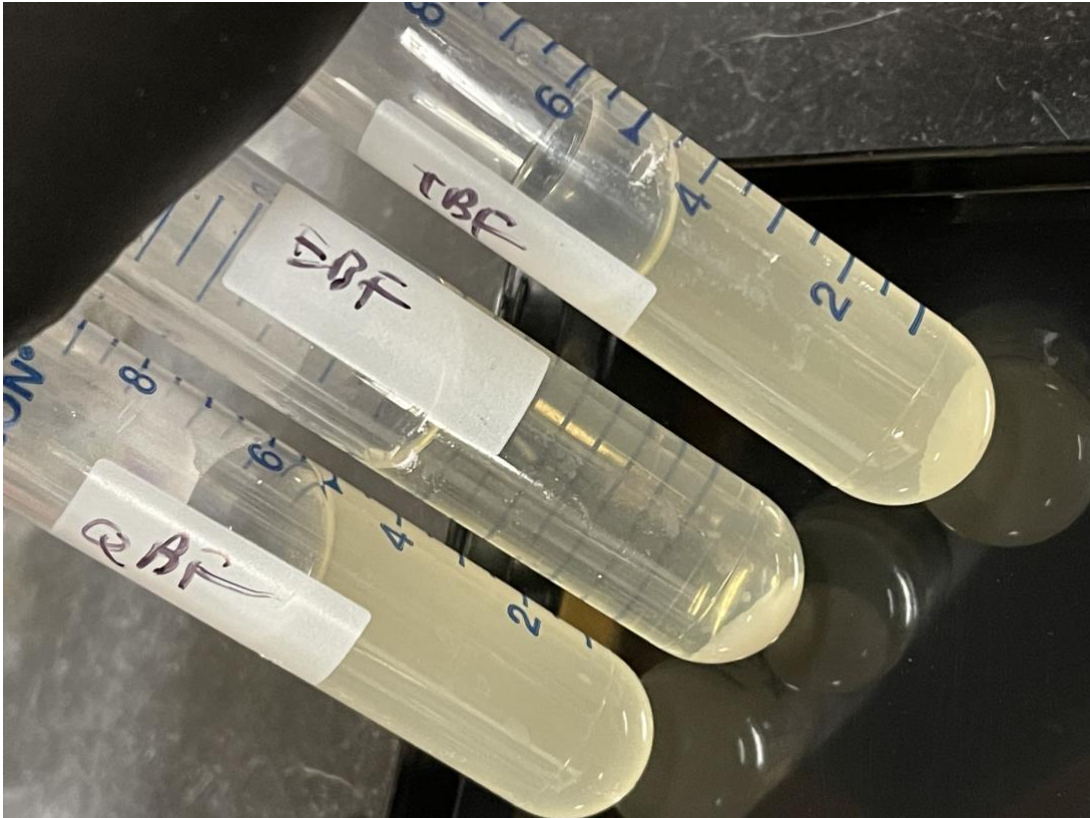


Fig. S4.5. Images of PhoA, E6/PhoA and triblock/PhoA cultures. Left bottom tube contains a PhoA culture. Without surface protein expression, the PhoA culture stays turbid and cells are freely floating. The middle tube is an E6/PhoA culture. E6 increases intercellular adhesion, causing cells to aggregate and precipitate, settling to the bottom of the tube. Top right tube is triblock/PhoA. Many cells are still suspended in the culture, but some precipitate and settle to the tube bottom.

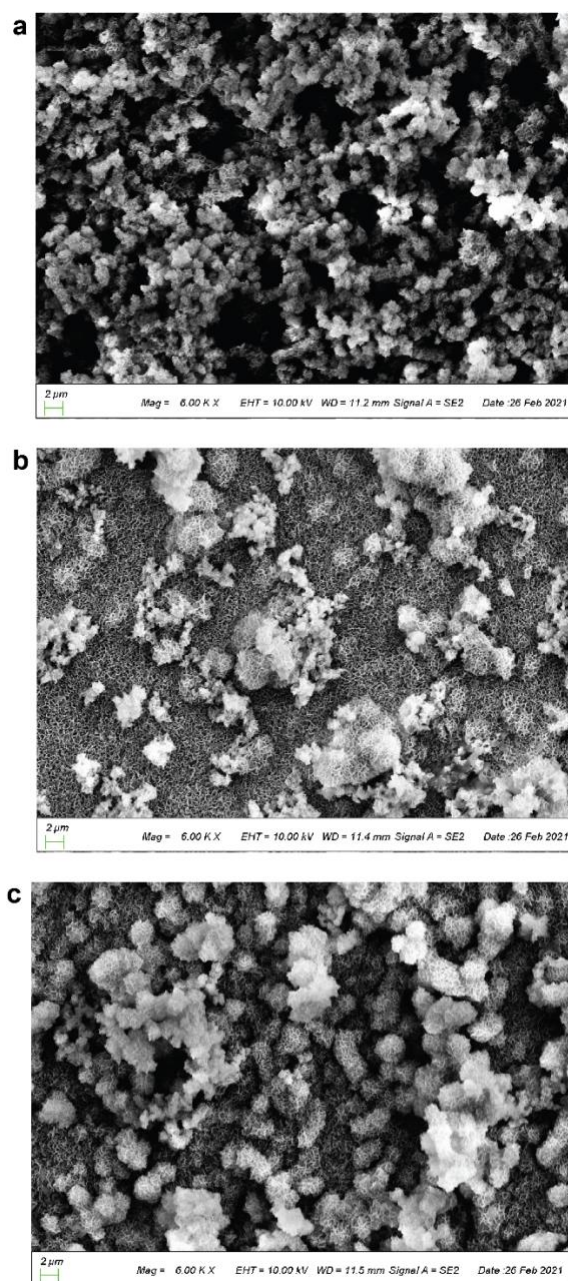


Fig. S4.6. SEM images of three types of 7 days old (1 day induction with 0.1% arabinose for PhoA expression) engineered *E. coli* films with different surface protein constructs after 24 hrs of mineralization in 10 mM CGP: **a**, no surface-displayed peptide (PhoA); **b**, with surface-displayed E6 peptides (E6/PhoA); **c**, with surface-displayed triblock peptides (Triblock/PhoA). Scale bars, 2 μm.

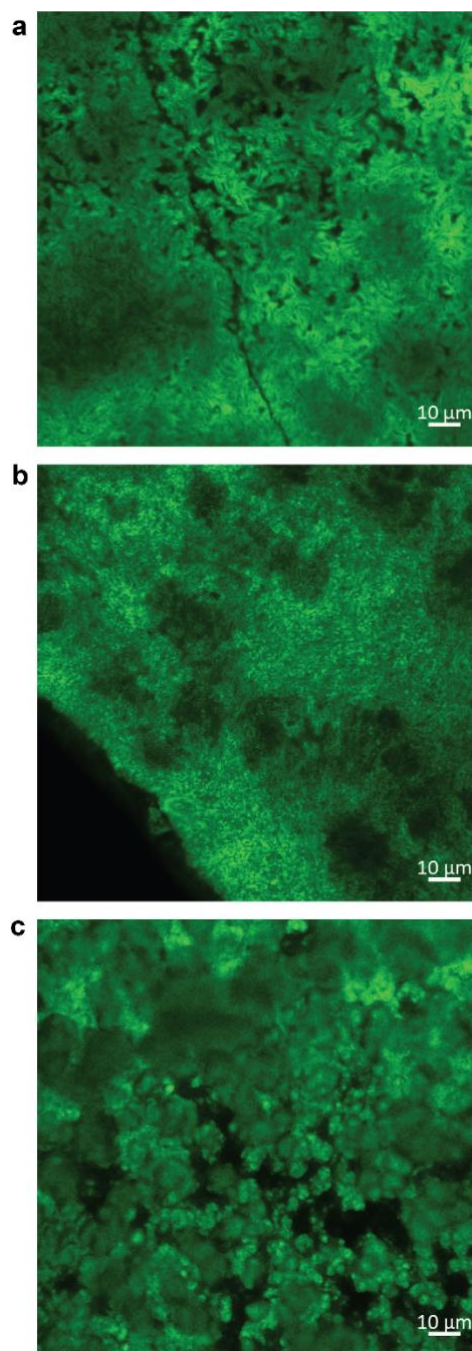


Fig. S4.7. Calcium-tracking fluorescence images of three types of 7 days old (1 day induction with 0.1% arabinose for PhoA expression) engineered *E. coli* films with different surface protein constructs after 24 hrs of mineralization in 10 mM CGP: **a**, no surface-displayed peptide (PhoA); **b**, with surface-displayed E6 peptides (E6/PhoA); **c**, with surface-displayed triblock peptides (Triblock/PhoA). Scale bars, 10 μm.

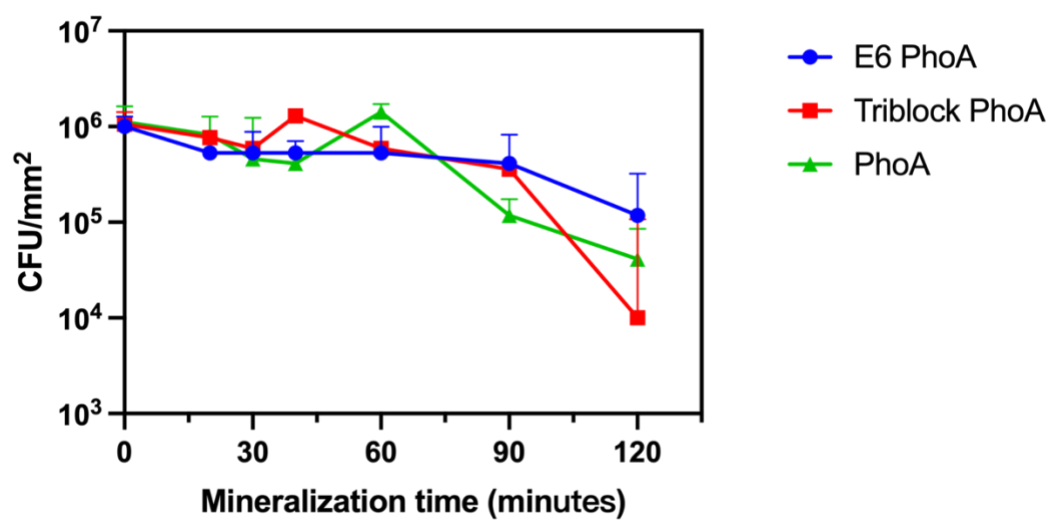


Fig. S4.8. Colony-forming units (CFU) per unit area of the three types of films examined in this work. Little change in viability was observed during the first hour of mineralization. Relative large decrease in viability was observed after 90 min of mineralization. Triblock/PhoA has least viability across all three constructs after 2 h of mineralization.

Supplementary Notes 4.4: Raman cross section data for quantification of phosphate/CH (molar ratio)

To get the phosphate/CH ratio in each sample from SRS imaging data, we used the SRS intensity of both the phosphate and CH channels, as well as the known Raman cross sections of phosphate P-O bond and C-H bond vibrations (**Table S4.3**).

$$\frac{\text{Phosphate}}{\text{CH}} \text{ molar ratio} = \frac{\frac{I_{\text{Phosphate}}}{\sigma_{\text{Phosphate}}}}{\frac{I_{\text{CH}}}{\sigma_{\text{CH}}}}$$

I: SRS intensity; σ : Raman cross section (**Table S4.3**)

Table S4.3: Reported Raman cross sections of phosphate and C-H bond vibrations^{25,26}

Target	Raman Cross Section (cm ⁻²)
Phosphate	8.10E-30
CH	1.00E-29

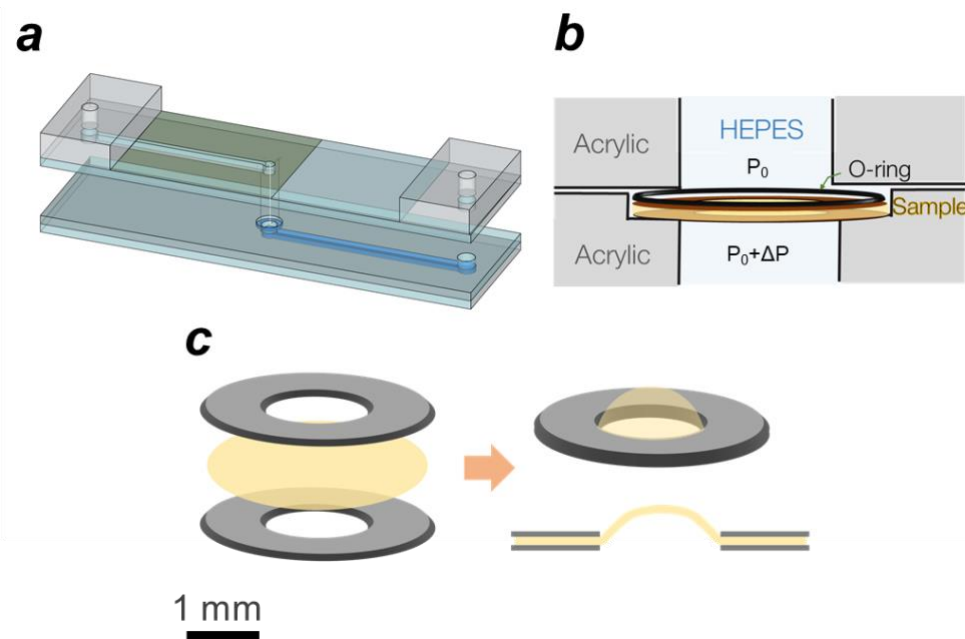


Fig. S4.9. **a**, Schematic of bulge test device, fabricated as two parts that are separated to load a sample in the central chamber at the center of the device. When sealed, each external port connects, via a channel, to a reservoir of fluid that is used to control pressure on the top or bottom face of the sample respectively (reservoirs not shown). Gray layers are acrylic; green thin layer is cover slip glass; layers are bonded using epoxy. Horizontal channels are longer than shown. **b**, Schematic diagram of central chamber. Bacterial film sample is supported by two washer-shaped disks. A thin O-ring seals this “sandwich” to the top half of the device. **c**, Schematic showing a disk of bacterial film sample clamped between two washer-shaped supports; when the supports and specimen are loaded in the central chamber and $p_{\text{bottom face}} > p_{\text{top face}}$, the bacterial film bulges upward (right).

Supplementary Notes 4.5: Mechanical property obtained by bulge/inflation tests

Mechanical properties of the biofilms were estimated using a bulge/inflation test, a method that has been used extensively in the characterization of sheet metals, polymers, and some biological tissues.²⁷⁻³⁸ A millifluidic device was constructed using laser cut acrylic sheets to adapt the bulge test to the Pa-kPa pressures needed to deform the biofilms. The final device construct consisted of a sealed central chamber housing the biofilm sample as a 3 mm diameter disk, sandwiched between two washer-shaped supports (**Fig. S4.9a, b**).

Analysis

Analysis protocols: Biofilm thickness ranged from 55-120 μm with a majority of films under 80 μm in thickness. Thus, the ratio of aperture diameter to film thickness ranged from 12.5 to 27.2. Flexural stiffness was neglected and only membrane stresses and strains were considered. Analysis of 2D images further required the spherical cap assumption: that there is equibiaxial stress and strain everywhere in the film and that the bulge radius of curvature is the same in both radial and circumferential directions – these assumptions are generally only satisfied at the center of the film and fail near the clamped edge where the circumferential strain vanishes.

Analysis of 2D images: 2D OCT datasets were exported as tiff files and cropped using ImageJ. The resulting images were processed with in-house MATLAB scripts: the images were binarized; the top and bottom surfaces of the film were automatically detected and fit to fourth degree polynomials which were then used to estimate arc

lengths of the top and bottom surfaces of the film. The arc lengths were used to calculate true strain ϵ averaged over the top and bottom surfaces of the biofilm.

True stress was calculated with the equation for stress in a thin-walled spherical pressure vessel:

$$\sigma = \frac{PR}{2t}$$

Where σ is film stress, P is the applied pressure, R is bulge radius of curvature, and t is instantaneous film thickness. Further, $R = \sqrt{a^2 + h^2}$ where a is radius of aperture of the support disk and h is deflected height of the center of the film, directly measurable by OCT. Young's modulus was estimated using the initial linear regime of each stress-strain trace.

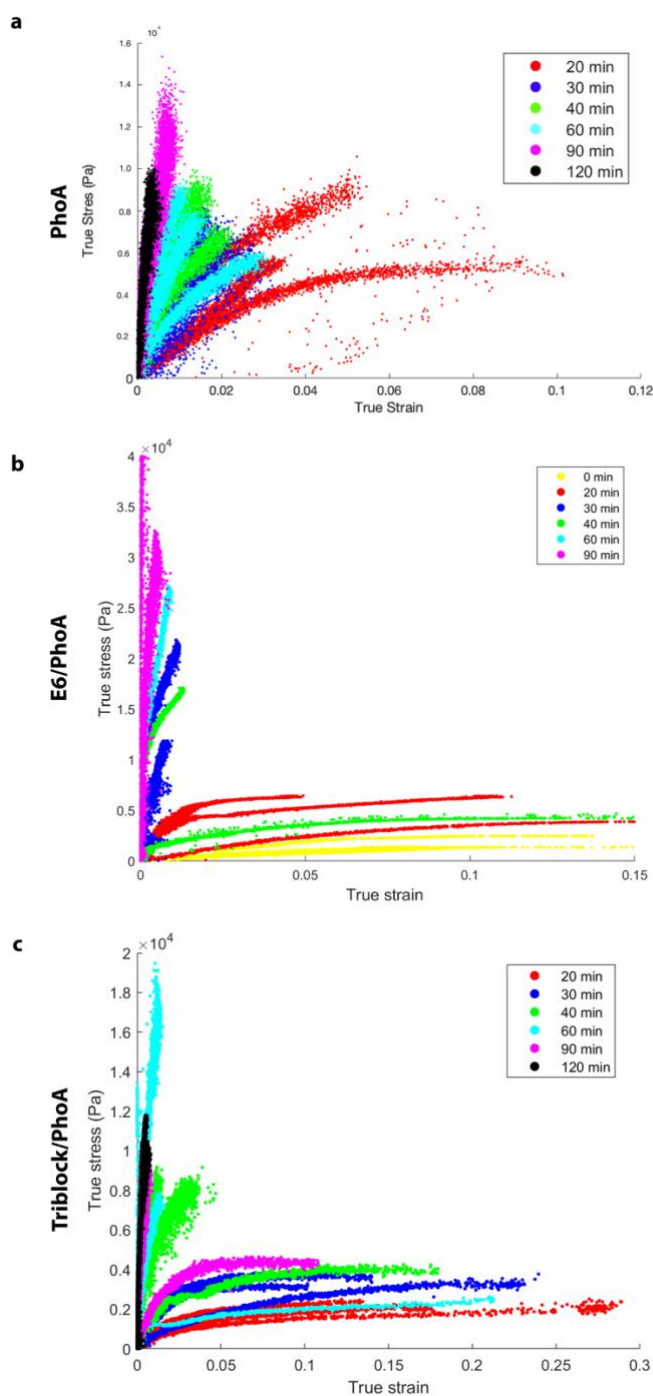


Fig. S4.10. **a**, True stress vs. true strain curves of all 7 days old PhoA films mineralized at different time points. Number of replicates for each time point: 20 min, $n = 3$; 30 min, $n = 3$; 40 min, $n = 3$; 60 min, $n = 3$; 90 min, $n = 3$; 120 min, $n = 2$. **b**, True stress vs. true strain curves of all 7 days old E6/PhoA films mineralized at different time points. Number of replicates for each time point: 0 min, $n = 3$; 20 min, $n = 3$; 30 min, $n = 3$; 40 min, $n = 2$; 60 min, $n = 1$; 90 min, $n = 3$. **c**, True stress vs. true strain curves of all 7 days old Triblock/PhoA films mineralized at different time points. Number of replicates for each time point: 20 min, $n = 3$; 30 min, $n = 3$; 40 min, $n = 4$; 60 min, $n = 4$; 90 min, $n = 3$; 120 min, $n = 4$.

8. References

1. A. Rodrigo-Navarro, S. Sankaran, M. J. Dalby, A. del Campo, M. Salmeron-Sanchez, Engineered living biomaterials. *Nat. Rev. Mater.* **6**, 1175–1190 (2021).
2. A. D. Lantada, J. G. Korvink, M. Islam, Taxonomy for engineered living materials. *Cell Reports Phys. Sci.* **3**, 100807 (2022).
3. W. V Srubar, Engineered Living Materials: Taxonomies and Emerging Trends. *Trends Biotechnol.* **39**, 574–583 (2021).
4. A. M. Duraj-Thatte, A. Manjula-Basavanna, N.-M. D. Courchesne, G. I. Cannici, A. Sánchez-Ferrer, B. P. Frank, L. van't Hag, S. K. Cotts, D. H. Fairbrother, R. Mezzenga, Water-processable, biodegradable and coatable aquaplastic from engineered biofilms. *Nat. Chem. Biol.* **17**, 732–738 (2021).
5. S. Guo, E. Dubuc, Y. Rave, M. Verhagen, S. A. E. Twisk, T. van der Hek, G. J. M. Oerlemans, M. C. M. van den Oetelaar, L. S. van Hazendonk, M. Brüls, Engineered living materials based on adhesin-mediated trapping of programmable cells. *ACS Synth. Biol.* **9**, 475–485 (2020).
6. X. Hua, M. J. Marshall, Y. Xiong, X. Ma, Y. Zhou, A. E. Tucker, Z. Zhu, S. Liu, X.-Y. Yu, Two-dimensional and three-dimensional dynamic imaging of live biofilms in a microchannel by time-of-flight secondary ion mass spectrometry. *Biomicrofluidics.* **9**, 31101 (2015).
7. Y. Ding, Y. Zhou, J. Yao, C. Szymanski, J. Fredrickson, L. Shi, B. Cao, Z. Zhu, X.-Y. Yu, In situ molecular imaging of the biofilm and its matrix. *Anal. Chem.* **88**, 11244–11252 (2016).
8. B. An, Y. Wang, X. Jiang, C. Ma, M. Mimee, F. Moser, K. Li, X. Wang, T.-C. Tang, Y. Huang, Programming living glue systems to perform autonomous mechanical repairs. *Matter.* **3**, 2080–2092 (2020).

9. J. Huang, S. Liu, C. Zhang, X. Wang, J. Pu, F. Ba, S. Xue, H. Ye, T. Zhao, K. Li, Programmable and printable *Bacillus subtilis* biofilms as engineered living materials. *Nat. Chem. Biol.* **15**, 34–41 (2019).
10. Y. Wang, B. An, B. Xue, J. Pu, X. Zhang, Y. Huang, Y. Yu, Y. Cao, C. Zhong, Living materials fabricated via gradient mineralization of light-inducible biofilms. *Nat. Chem. Biol.* **17**, 351–359 (2021).
11. W. Min, C. W. Freudiger, S. Lu, X. S. Xie, Coherent Nonlinear Optical Imaging: Beyond Fluorescence Microscopy. *Annu. Rev. Phys. Chem.* (2011), doi:10.1146/annurev.physchem.012809.103512.
12. C. W. Freudiger, W. Min, B. G. Saar, S. Lu, G. R. Holtom, C. He, J. C. Tsai, J. X. Kang, X. S. Xie, Label-free biomedical imaging with high sensitivity by stimulated raman scattering microscopy. *Science* (80-.). (2008), doi:10.1126/science.1165758.
13. L. Wei, F. Hu, Y. Shen, Z. Chen, Y. Yu, C. C. Lin, M. C. Wang, W. Min, Live-cell imaging of alkyne-tagged small biomolecules by stimulated Raman scattering. *Nat. Methods* (2014), doi:10.1038/nmeth.2878.
14. K. T. Schiessl, F. Hu, W. Min, L. E. P. Dietrich, J. Jo, S. Z. Nazia, B. Wang, A. Price-whelan, Phenazine production promotes antibiotic. *Nat. Commun.* **10**, 1–10 (2019).
15. K. Miao, L. Wei, Live-Cell Imaging and Quantification of PolyQ Aggregates by Stimulated Raman Scattering of Selective Deuterium Labeling. *ACS Cent. Sci.* **6**, 478–486 (2020).
16. Q. Cheng, L. Wei, Z. Liu, N. Ni, Z. Sang, B. Zhu, W. Xu, M. Chen, Y. Miao, L. Q. Chen, W. Min, Y. Yang, Operando and three-dimensional visualization of anion depletion and lithium growth by stimulated Raman scattering microscopy.

- Nat. Commun.* **9**, 1–10 (2018).
17. R. Bhatt, M. Jaffe, A. S. Narang, S. H. S. Boddu, Eds. (Springer International Publishing, Cham, 2015; https://doi.org/10.1007/978-3-319-20206-8_11), pp. 311–348.
 18. K. L. Rogers, J. Cosmidis, K. Benzerara, F. Guyot, F. Skouri-panet, Calcium-Phosphate Biomineralization Induced by Alkaline Phosphatase Activity in *Escherichia coli* : Localization , Kinetics , and Potential Signatures in the Fossil Record. *Front. Geosci.* **3**, 1–20 (2015).
 19. S. Prieto, A. Shkilnyy, C. Rumplach, A. Ribeiro, F. J. Arias, J. C. Rodríguez-cabello, A. Taubert, Biomimetic Calcium Phosphate Mineralization with Multifunctional Elastin-Like Recombinamers. *Biomacromolecules*, 1480–1486 (2011).
 20. P. N. de Aza, C. Santos, A. Pazo, S. de Aza, R. Cuscó, L. Artús, Vibrational Properties of Calcium Phosphate Compounds. 1. Raman Spectrum of β -Tricalcium Phosphate. *Chem. Mater.* **9**, 912–915 (1997).
 21. P. N. de Aza, F. Guitián, C. Santos, S. de Aza, R. Cuscó, L. Artús, Vibrational Properties of Calcium Phosphate Compounds. 2. Comparison between Hydroxyapatite and β -Tricalcium Phosphate. *Chem. Mater.* **9**, 916–922 (1997).
 22. M. T. Kozlowski, B. R. Silverman, C. P. Johnstone, D. A. Tirrell, Genetically Programmable Microbial Assembly. *ACS Synthetic Biology*, *10*(6), 1351–1359. (2021).
 23. S. Prieto, A. Shkilnyy, C. Rumplach, A. Ribeiro, F. J. Arias, J. C. Rodríguez-cabello, A. Taubert, Biomimetic Calcium Phosphate Mineralization with Multifunctional Elastin-Like Recombinamers. *Biomacromolecules*, 1480–1486 (2011).

24. P. B. Rapp, A. K. Omar, B. R. Silverman, Z.-G. Wang, D. A. Tirrell, Analysis and Control of Chain Mobility in Protein Hydrogels, *Journal of the American Chemical Society*, **140** (43), 14185–14194 (2018).
25. S. G. Demos, R. N. Raman, S. T. Yang, R. A. Negres, K. I. Schaffers, M. A. Henesian, Measurement of the Raman scattering cross section of the breathing mode in KDP and DKDP crystals. *Opt. Express*. **19**, 21050–21059 (2011).
26. T. E. Acosta-Maeda, A. K. Misra, J. N. Porter, D. E. Bates, S. K. Sharma, Remote Raman Efficiencies and Cross-Sections of Organic and Inorganic Chemicals. *Appl. Spectrosc.* **71**, 1025–1038 (2016).
27. Tsakalakos, T. & Hilliard, J. E. Elastic modulus in composition-modulated copper-nickel foils. *J. Appl. Phys.* **54**, 734–737 (1983).
28. Hsu, F. P. K., Liu, A. M. C., Downs, J., Rigamonti, D. & Humphrey, J. D. A Triplane Video-Based Experimental System for Studying Axisymmetrically Inflated Biomembranes. *IEEE Trans. Biomed. Eng.* **42**, 442–450 (1995).
29. Mohan, D. & Melvin, J. W. Failure properties of passive human aortic tissue. II-Biaxial tension tests. *J. Biomech.* **16**, (1983).
30. Cavinato, C. *et al.* Biaxial loading of arterial tissues with 3D in situ observations of adventitia fibrous microstructure: A method coupling multi-photon confocal microscopy and bulge inflation test. *J. Mech. Behav. Biomed. Mater.* **74**, 488–498 (2017).
31. Midgett, D. E., Quigley, H. A. & Nguyen, T. D. In vivo characterization of the deformation of the human optic nerve head using optical coherence tomography and digital volume correlation. *Acta Biomater.* **96**, 385–399 (2019).
32. Tonge, T. K., Atlan, L. S., Voo, L. M. & Nguyen, T. D. Full-field bulge test for planar anisotropic tissues: Part I-Experimental methods applied to human skin

- tissue. *Acta Biomater.* **9**, 5913–5925 (2013).
33. Wang, L., Tian, L., Huang, Y., Huang, Y. & Zheng, Y. Assessment of Corneal Biomechanical Properties with Inflation Test Using Optical Coherence Tomography. *Ann. Biomed. Eng.* **46**, 247–256 (2018).
 34. Zamprogno, P. *et al.* Mechanical properties of soft biological membranes for organ-on-a-chip assessed by bulge test and AFM. *ACS Biomater. Sci. Eng.* **7**, 2990–2997 (2021).
 35. O’Connell, P. A. & McKenna, G. B. Novel nanobubble inflation method for determining the viscoelastic properties of ultrathin polymer films. *Rev. Sci. Instrum.* **78**, 14706 (2007).
 36. Turner, J. A., Menary, G. H. & Martin, P. J. Biaxial characterization of poly(ether-ether-ketone) for thermoforming: A comparison between bulge and in-plane biaxial testing. *Polym. Eng. Sci.* **59**, 1853–1865 (2019).
 37. Marra, S. P., Kennedy, F. E., Kinkaid, J. N. & Fillinger, M. F. Elastic and rupture properties of porcine aortic tissue measured using inflation testing. *Cardiovasc. Eng.* **6**, 123–131 (2006).
 38. Tabata, O., Kawahata, K., Sugiyama, S. & Igarashi, I. Mechanical property measurements of thin films using load-deflection of composite rectangular membranes. *Sensors and Actuators* **20**, 135–141 (1989).

Chapter 5

Matrix Production by Bacterial Enzymes and Peptide Surface Display

1. Abstract

In this chapter, we demonstrate that an engineered ascorbate peroxidase enzyme (Apex2) can be fused with the EhaA autotransporter and remain capable of performing oxidative polymerization of aniline into polyaniline (PANI) when displayed at the cell surface. Apex2 catalyzed formation of PANI was confirmed by UV-Vis spectroscopy and transmission electron microscopy (TEM). These results suggested that living bacteria can be engineered to catalyze synthetic polymer production. Secondly, a peptide known to mediate silica deposition was fused with an elastin-like-peptide linker and successfully displayed at the bacterial surface using the EhaA autotransporter system. Different peptides expressed at the cell surface induced silica deposition with drastically different morphologies as observed by scanning electron microscopy (SEM). β -peptide induced formation of wire-like silica while R5 peptide induced formation of silica without well-defined morphological features. The viability of the cells was not affected greatly by silica deposition, as the colony forming units per mm² remained on the order of 10⁶ before and after biomineralization. These results suggest that we can manipulate morphologies of silica by genetically programming bacterial cells to surface display multiple kinds of peptides, and that cell viability can be preserved in the deposition process.

2. Introduction

In natural biofilms, bacteria secrete polymeric matrices mainly made of proteins or polysaccharides to help them attached to surfaces, survive environmental stress and gain advantage over other microorganisms.¹⁻⁵ To produce these polymeric materials, bacteria must actively take up the monomers of proteins and polysaccharides (amino acids and sugars) from the environment and then, using an energy consuming synthesis and secretion pathways, transport the produced polymers into the environment (**Fig 5.1a**).^{6,7} This process requires molecules to diffuse into the cell, and then undergo chemical conversion and secretion. It is tempting to consider performing polymerization to form matrix directly at the surface of the bacterium. Enzymes or peptides with catalytic functions would then be in direct contact with reactive species such that active uptake into the cell is no longer needed (**Fig 5.2b**).

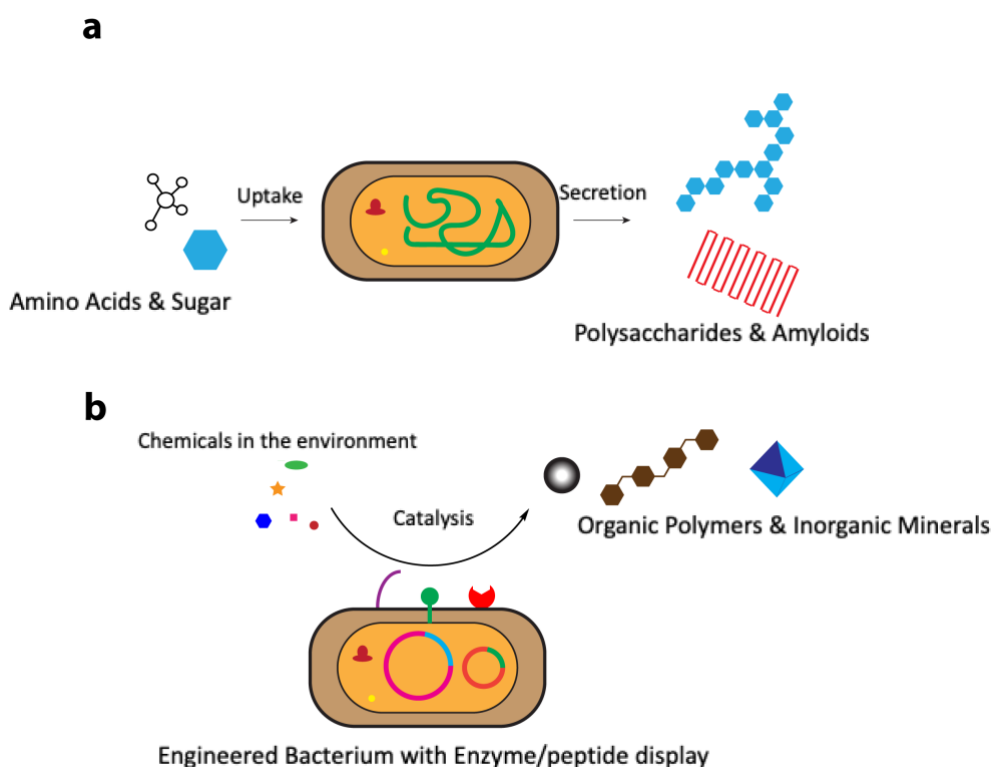


Figure 5.1. Natural and unnatural strategies to synthesize extracellular matrix **a**, Matrix production process in natural biofilm. **b**, Cell surface matrix synthesis using engineered bacterium.

Recently, some research laboratories have utilized the natural bacterial capacity for extracellular electron transfer (EET)⁸⁻¹⁰ to catalyze reactions and produce polymers.^{11,12} *Shewanella oneidensis* is among the most extensively examined organisms; its EET complex structure has been solved¹³ and because it has the capability to reduce heavy metals¹⁴ it is a promising candidate for environmental remediation.¹⁵ Recently, the EET complex of *S. oneidensis* was engineered into *E. coli* to create systems that can sense multiple environmental contaminants.¹⁶ This implies that even model organisms like *E. coli* can tolerate protein complexes containing multiple metal-containing heme centers from other species. Decorating *E. coli* with a relative small heme-containing enzyme derived from another organism is plausible.

Diatoms are unicellular microalgae that have intricate and beautiful cell walls composed of silica whose shape, structure and morphologies are strictly controlled genetically.¹⁷⁻¹⁹ Silica has diverse morphologies and can be tuned to have different degrees of porosity²⁰⁻²² (different surface area). Silica can be used as an antibacterial reagent when doped with antibacterial metals like silver.^{23,24} The porous nature of silica, however, also makes it a potential protective coating for bacteria. When coated with silica, cells can still contact nutrients in the environment. The genetic tunability and vast morphologies as shown in the case of diatoms also suggest that it is possible for us to find silica with suitable morphology and porosity as bacterial coating through genetic manipulation.

3. Results and discussion

5.1 Surface displayed Apex2 enzyme can catalyze oxidative formation of polyaniline (PANI)

Apex2 is an engineered ascorbate peroxidase from soy bean cytosol (**Fig 5.2**).^{25,26} Apex2 acts on a wide range of substrates and has many applications in electron microscopy²⁷, spatial proteomics²⁸ and transcriptomics.²⁹ Recently interest in using Apex2 in materials research has grown. Liu et.al reported that Apex2 can be used to catalyze oxidative deposition of the conductive polymer polyaniline in neural tissues and affect neural functions.³⁰ Another article reported that Apex2, when fused with *B. subtilis* spore coating proteins, remained functional and retained 84% of its original activity after recycled for 10 times from spores that performed reactions.³¹ Inspired by this work, we attempted to fuse Apex2 to our autotransporter surface display system. The specific method and cloning details can be found in **Supplementary Note 5.1**. A construct of Apex2-AT encoded in pQE80 plasmid was made and transformed into DH10B cells to drive constitutive expression. An overnight culture was diluted to OD₆₀₀ ~0.9 and 1 ml of the diluted culture was sedimented in a centrifuge at 5000 x g for 10 min. The clear supernatant was discarded and 5 ml of monomer solution containing 1:1 ratio of aniline and *N*-phenylenediamine both at 0.5 mM concentration, 0.1 mM H₂O₂ in 1xPBS buffer buffered at pH 7.4 was added into the culture tube (**Fig 5.2b**). Once the pink monomer solution (**Fig 5.2c left**) was in contact with the pellet, the color immediately changed to green (**Fig 5.2c middle**). The pellet was resuspended by pipetting and the culture tube containing the reaction mixture was placed in a shaking incubator at 250 rpm, 37 °C for 1.5 h. After 30 min, the reaction mixture turned purple (**Fig 5.2c left**). After 1.5 h, cells were spun down to yield a black pellet. The supernatant was collected and UV-Vis spectrum was taken by Cary50 UV-Vis

Spectrophotometer (Varian) as shown in **Fig 5.2d**. Comparing with the original monomer solution, the supernatant after reaction has a characteristic peak shoulder around 570 nm to 590 nm (**Fig 5.2 d, arrow**). According to previous work using Apex2 in neuron culture,³⁰ this peak should correspond to low molecular weight polyaniline (PANI). The color change was not observed for cells without Apex2-AT surface expression. The pelleted cells for both Apex2-AT expressing and Apex2-AT-free cells after reaction were washed three times with 5 ml of water and collected and imaged on a **TF30ST (FEI, now Thermo Fisher)** transmission electron microscope (TEM). As shown in **Fig 5.2e**, there are dark fibrous matrix materials surrounding the Apex2-AT expressing cells but not the control (Apex2-AT non-expressing) cells. It's worth noting that control cells appear darker than normal *E. coli* cells. This might be because there are *E. coli* peroxidases like Ccp³² that can react with hydrogen peroxide and produce a small amount of PANI in the cytosol or periplasm. These results suggest that Apex2 has been successfully fused with the autotransporter and remains functional when displayed. More broadly, the Apex2-AT construct is a prototypical system that demonstrates polymerization at the bacterial cell surface through engineered enzyme display.

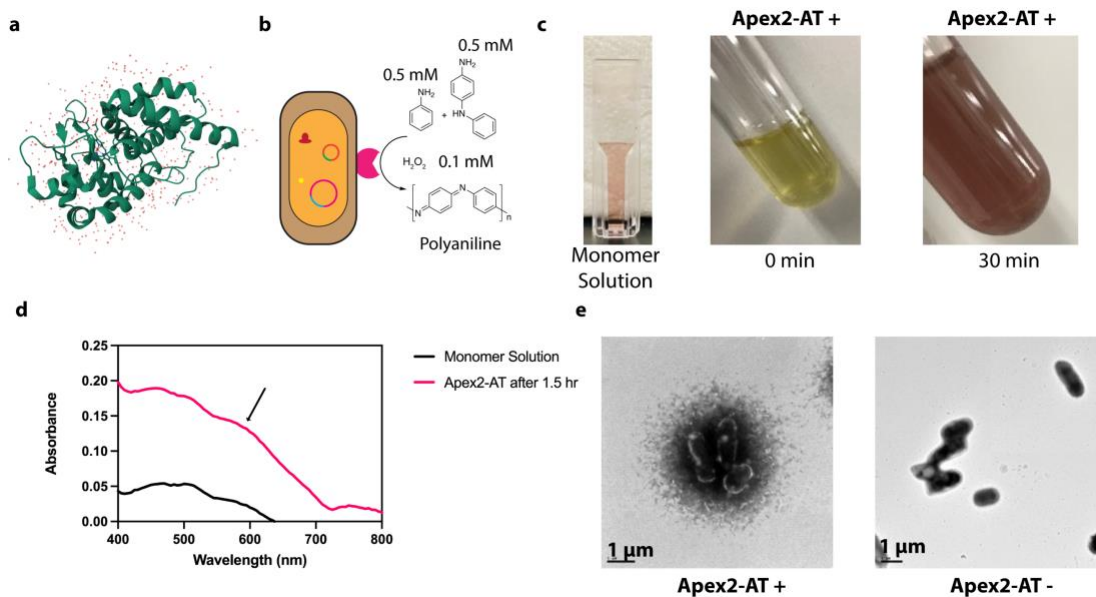


Figure 5.2. Apex2-AT surface display in *E. coli* catalyzes oxidative deposition of PANI **a**, Crystal structure of ascorbate peroxidase from soy bean cytosol. PDB id: 1OAG **b**, Schematic of Apex2-AT-displaying *E. coli* catalyzing oxidative formation of polyaniline. **c**, Left: Image of original monomer solution. Middle: color of reaction mixture when Apex2-AT expressing cell pellet was mixed with monomer solution with H_2O_2 added. Right: color of reaction mixture after 30 min. **d**, UV-vis spectra of monomer solution and supernatant of reaction mixture 1.5 h after reaction. **e**, Left: TEM images of Apex2-AT expressing cells after treatment with monomer solution and H_2O_2 for 0.5 h; Right: TEM images of Apex2-AT free cells (control) after treatment with monomer solution and H_2O_2 for 0.5 h.

5.2 Surface displayed peptide can control morphology of deposited silica and silica deposition does not affect viability of the film.

One well studied diatom peptide that can mediate silica precipitation is R5 peptide with amino acid sequence of “SSKKSGSYSGSKGSKRRIL”.³³ R5 peptide when treated with silicic acid or tetramethyl orthosilicate, catalyzes deposition of amorphous silica particles.^{34–36} A recent publication demonstrated that R5 can be fused with engineered proteins like curli fibrils and facilitate formation of silica-protein-polysaccharide composite materials.³⁴ Another interesting peptide system that can mediate silica deposition was reported using lysine-leucine (KL) peptides.³⁷ These peptides contain only lysine and leucine, but sequence variation causes secondary structure differences in these peptide. Peptides with different secondary structures caused silica deposited around them to have different morphologies. Among all secondary structures, β -sheet form KL peptide generates wire-like silica, while other forms generates either spherical

or rod-shaped silica.³⁷ Inspired by these systems, we placed R5 and β peptides into our surface-display system. A spacer of six 25-amino acid elastin-like-peptide repeats (E6) was placed between the silica precipitation peptide and the autotransporter domain. We placed the resulting R5E6-AT and β E6-AT constructs in pQE80 plasmids and transformed these plasmids into DH10B cells for constitutive expression. We used previously described suction coating and bacterial film culturing methods in Chapter 2 to grow R5E6-AT and β E6-AT bacterial films on polycarbonate filters. After bacterial films were grown for 7 days, they were immersed in 20 mM Na₂SiO₃ in 1 x PBS buffered at pH 7.4 for 24 h (**Fig 5.3a**) to allow silica deposition on the bacterial film surface. After 24 h, films were removed from the buffer and sampled for CFU per unit area by punching a 6-mm diameter circular region. Most bacteria remained viable after silica deposition as shown by the observation that CFU per unit area remains at the same order of magnitude compared to the original film (before mineralization) as shown in **Fig 5.3b**. Films were frozen at -80 °C overnight and then lyophilized. The lyophilized sample were imaged on a 1550VP (Zeiss) scanning electron microscope. SEM images of R5E6-AT films showed that a crust of silica was formed on top of the bacterial film (**Fig 5.3c**). Silica deposited on β E6-AT films, however, forms a fibrous network on top of the bacterial film. At higher magnification, we can see what appear to be cells entrapped in the wire-like silica (**Fig 5.3d**). Rich Si elementary contents in these materials were confirmed by energy dispersive spectroscopy (EDS), with results shown in **Fig S5.1&2, Table S5.3&4**. These results show that we can genetically manipulate the morphology of silica using engineered living bacteria with surface peptide display.

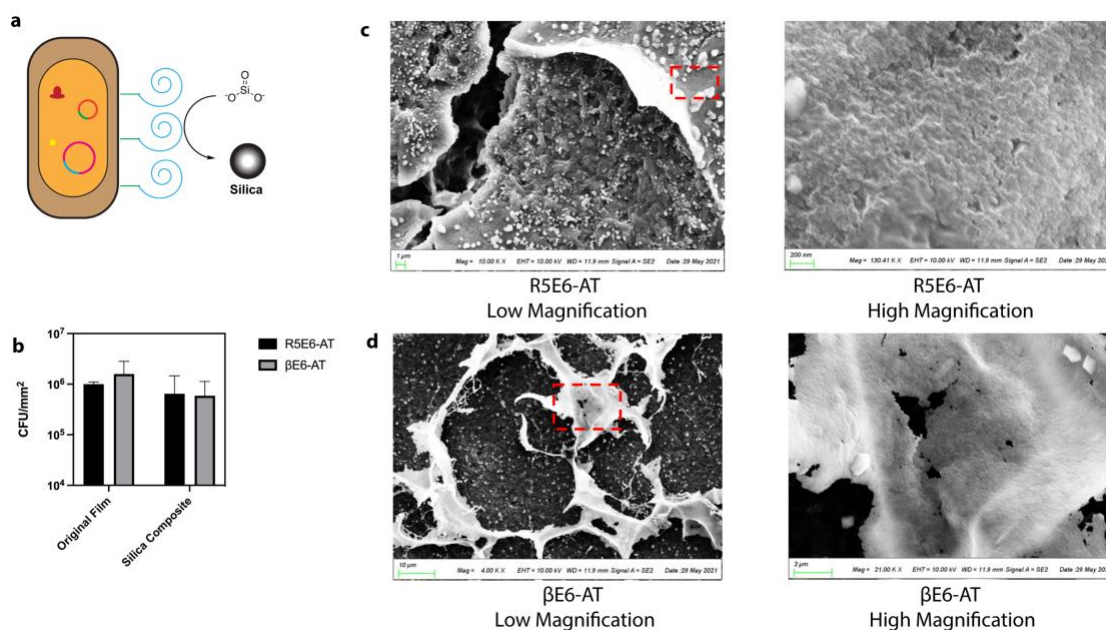


Figure 5.3. R5 and β peptide surface display in *E. coli* causes deposition of silica with different morphologies
a, Schematic of peptide displaying *E. coli* catalyzing silica deposition. **b**, CFU per unit for R5E6-AT films and β E6-AT films before and after silica deposition. **c**, Left: Low magnification SEM image of R5E6-AT films after silica deposition. Scale bar. 1 μm ; Right: High magnification image of silica deposit in red dashed rectangle of low magnification image. Scale bar, 200 nm. **d**, Left: Low magnification SEM image of β E6-AT films after silica deposition. Scale bar. 10 μm ; Right: High magnification image of silica deposit in red dashed rectangle of low magnification image. Scale bar, 2 μm .

4. Conclusion

In this work, we showed that the Apex2 peroxidase remains functional when fused with EhaA autotransporter and can catalyze oxidative deposition of polyaniline (PANI). This result suggests that displaying functional enzymes to catalyze polymeric matrix formation at cell surface is plausible. Bacterial films made of cells displaying peptide that can catalyze deposition of silica with different morphologies were treated with sodium silicate. The resulting silica deposited on the bacterial film surface have morphologies that depend on the peptide displayed. The viability of the bacteria was not substantially affected by silica deposition. This result implies that silica can be a candidate for genetically programmable protective coating for probiotic bacteria.

5. Materials and Methods

Bacterial Strains. All experiments were conducted in *E. coli* strain DH10B (Invitrogen, Carlsbad, CA). Details of reagents, cloning and protein expression experiments can be found in **Table S5.1** and **Supplementary Notes 5.1-2**.

Preparation of Bacterial Films. Individual colonies harvested from LB plates were grown overnight to stationary phase in liquid LB medium supplemented with 100 mg/L ampicillin to maintain plasmid stability. The resulting cultures were then diluted to an optical density at 600 nm (OD₆₀₀) of approximately 0.8. Diluted cultures were loaded on UV-sterilized track-etched polycarbonate filters (Nuclepore Whatman, 0.2 μm pore size) mounted in vacuum filter units (Nalgene Rapid-flow Thermo-Fisher). For 2.5 cm diameter polycarbonate filters, 200 μL culture volumes were loaded and vacuum filtered. After filtration was complete, filters were transferred to fresh LB plates. Bacterial films were grown in a 37 °C incubator. Filters were moved to fresh LB agar plates containing suitable antibiotics every day for 7 days to allow film maturation.

6. Acknowledgements

Hanwei Liu conceived and designed the experiments under the supervision of Professor David A. Tirrell. Hanwei Liu was responsible for all the genetic engineering experiments, bacterial film growth, sample preparation and imaging. SEM microscopy was done at Caltech Geological and Planetary Science division's analytical facility. Dr. Yuxing Yao performed the TEM microscopy.

7. Supporting information

Supplementary Note 5.1: Reagents and suppliers

Restriction enzymes, ligase, and Q5 DNA polymerase were purchased from New England Biolabs (Beverly, MA). DNA oligos and G-blocks were purchased from Integrated DNA Technologies (Coralville, IA).

Supplementary Note 5.2: Plasmid subcloning

Recombinant fusion proteins were produced by standard recombinant DNA technology. DH10B *E. coli* were used for all cloning steps and material preparation.

Genes encoding autotransporter protein along with elastin solubility/stability tags have been previously cloned by our group into modified pQE-80L plasmids.³⁸

The pAT-Apex2 plasmid was created by ordering G-Block containing Apex2 sequence containing 5' BamHI and 3' XhoI restriction sites. The G-Block was digested by BamHI and XhoI restriction enzymes and ligated with a BamHI and XhoI digested pAT-E6 vector to make pAT-Apex2 plasmid.

pAT-R5E6 and pAT- β E6 were made by first mutating pX-ST using site directed mutagenesis by using designed primer containing new peptide sequence binding to the original plasmid and later PCR amplified.³⁹ pX-ST was converted into pX-R5 and pX- β . pX-R5 and pX- β were digested with XhoI and HindIII and an E6 insert cut with SalI and HindIII was ligated with the digested vector. pX-R5E6 and pX- β E6 were then digested by BamHI and XhoI and pasted into a pAT-E6 vector digested by digested by BamHI and XhoI to make pAT-R5E6, pAT- β E6. The sequence of all constructs were sequenced and confirmed by Laragen Inc. (Culver City, CA)

Supplementary Note 5.3: Buffer recipe

The 1x PBS buffers used in this work was purchased from ThermoFisher Scientific containing 155 mM NaCl, 1 mM KH_2PO_4 and 3 mM Na_2HPO_4 buffered at pH 7.4.

Table S5.1: Plasmids used in this study

Name	Backbone/origin/promoter	Purpose
pAT-E6	pQE80l/colE1/T5	Cloning of pAT-Apex2, pAT-R5E6 and pAT- β E6
pX-ST	pQE80l/colE1/T5	Cloning of pAT-R5E6 and pAT- β E6
pX-E6	pQE80l/colE1/T5	Cloning of pAT-R5E6 and pAT- β E6
pAT-Apex2	pQE80l/colE1/T5	Constitutive expression of Apex2-AT protein on cell surface
pX-R5	pQE80l/colE1/T5	Cloning of pAT-R5E6
pX- β	pQE80l/colE1/T5	Cloning of pAT- β E6
pX-R5E6	pQE80l/colE1/T5	Cloning of pAT-R5E6
pX- β E6	pQE80l/colE1/T5	Cloning of pAT- β E6
pAT-R5E6	pQE80l/colE1/T5	Constitutive expression of R5E6-AT protein on cell surface
pAT- β E6	pQE80l/colE1/T5	Constitutive expression of β E6-AT protein on cell surface

Table S 5.2: Proteins used in this study

Protein	Sequence
Apex2-AT	<p>MKYLLPTAAAGLLLLAAQPA MAMRGS HHHHHH GSVD GKS Y</p> <p>PTVSADYQDAVEKAKKKLRGFIAEKRCAPLMLRLAFHSAGTF</p> <p>DKGTKTGGPFGTIKHPAELAHSANGLDIAVRILLEPLKAEFPI</p> <p>LSYADFYQLAGVVAVEVTGGPKVPFHPGREDKPEPPPEGRLP</p> <p>DPTKGS DHLRDVFGKAMGLTDQDIVALSGGHTIGAAHKERSG</p> <p>FEGPWTSNPLIFDNSYFTELLS GEKEGLLQLPSDKALLSDPVFR</p> <p>PLVDKYAADEDAFFADYAEAHQKLSSELGFADALE TPTPGPDL</p> <p>NVDNDLRPEAGSYIANLAAANTMFTTRLHERLGNTYYTDMV</p> <p>TGEQKQTTMWMRHEGGH NKWRD GSGQLKTQSNRYVLQLG</p> <p>GDVAQWSQNGSDRWHVGMAGYGNSDSKTISSRTGYRAKA</p> <p>SVNGYSTGLYATWYADDES RNGAYLDSWAQYSWFDNTVKG</p> <p>DDLQSESYKSKGFTASLEAGYKHKLAEFNGSQGTRNEWYVQ</p> <p>PQAQVTWMGVKADKHRESNGTLVHSNGDGNVQTRLGVKT</p> <p>WLKSHHKMDDGKSREFQPFVEVNWLHNSKDFSTSM DGVSVT</p> <p>QDGARNIAEIKTGVEGQLNANLNVWGNVGVQVADRGYNDT</p> <p>SAMVGIKWQF</p>
R5E6-AT	<p>MKYLLPTAAAGLLLLAAQPA MAMRGS HHHHHH GSVD SSKK</p> <p>SGSYSGSKGSKRRILD VPGAGVPGAGVPGEGVPGAGVPGAG</p> <p>VPGAGVPGAGVPGEGVPGAGVPGAGVPGAGVPGAGVPGEG</p> <p>VPGAGVPGAGLDVPGAGVPGAGVPGEGVPGAGVPGAGVPG</p> <p>AGVPGAGVPGEGVPGAGVPGAGVPGAGVPGAGVPGAGVPGEGVPG</p>

	<p>AGVPGAGLETPTPGPDNLVDNDRPEAGSYIANLAAANTMFT</p> <p>TRLHERLGNTYYTDMVTGEQKQTTMWMRHEGGHMKWRDG</p> <p>SGQLKTQSNRYVLQLGGDVAQWSQNGSDRWHVGVMAAGYG</p> <p>NSDSKTISSRTGYRAKASVNGYSTGLYATWYADDES RNGAY</p> <p>LDSWAQYSWFDNTVKGDDLQSESYKSKGFTASLEAGYKHKL</p> <p>AEFNGSQGTRNEWYVQPQAQVTWIMGVKADKHRESNGTLVH</p> <p>SNGDGNVQTRLGVKTWLKSHHKMDDGKSREFQPFVEVNWL</p> <p>HNSKDFSTSMGVSVTQDGARNIAEIKTGVEGQLNANLNVW</p> <p>GNVGVQVADRGYNDTSAMVGIKWQF</p>
βE6-AT	<p>MKYLLPTAAAGLLLLAAQPA MAMRGS HHHHHH GSVD LKLLK</p> <p>LKLLKLLKLLKLLD VPGAGVPGAGVPGEGVPGAGVPGAGVPG</p> <p>AGVPGAGVPGEGVPGAGVPGAGVPGAGVPGAGVPGEGVPG</p> <p>AGVPGAGLDVPGAGVPGAGVPGEGVPGAGVPGAGVPGAGV</p> <p>PGAGVPGEGVPGAGVPGAGVPGAGVPGAGVPGEGVPGAGV</p> <p>GAGLETPTPGPDNLVDNDRPEAGSYIANLAAANTMFTTRLH</p> <p>ERLGNTYYTDMVTGEQKQTTMWMRHEGGHMKWRDGSQQL</p> <p>KTQSNRYVLQLGGDVAQWSQNGSDRWHVGVMAAGYGNSDS</p> <p>KTISSRTGYRAKASVNGYSTGLYATWYADDES RNGAYLDSW</p> <p>AQYSWFDNTVKGDDLQSESYKSKGFTASLEAGYKHKLAEFN</p> <p>GSQGTRNEWYVQPQAQVTWIMGVKADKHRESNGTLVHSNG</p> <p>DGNVQTRLGVKTWLKSHHKMDDGKSREFQPFVEVNWLHNS</p> <p>KDFSTSMGVSVTQDGARNIAEIKTGVEGQLNANLNVWGNV</p> <p>GVQVADRGYNDTSAMVGIKWQF</p>

Figure S5.1. R5E6-AT Silica EDS result

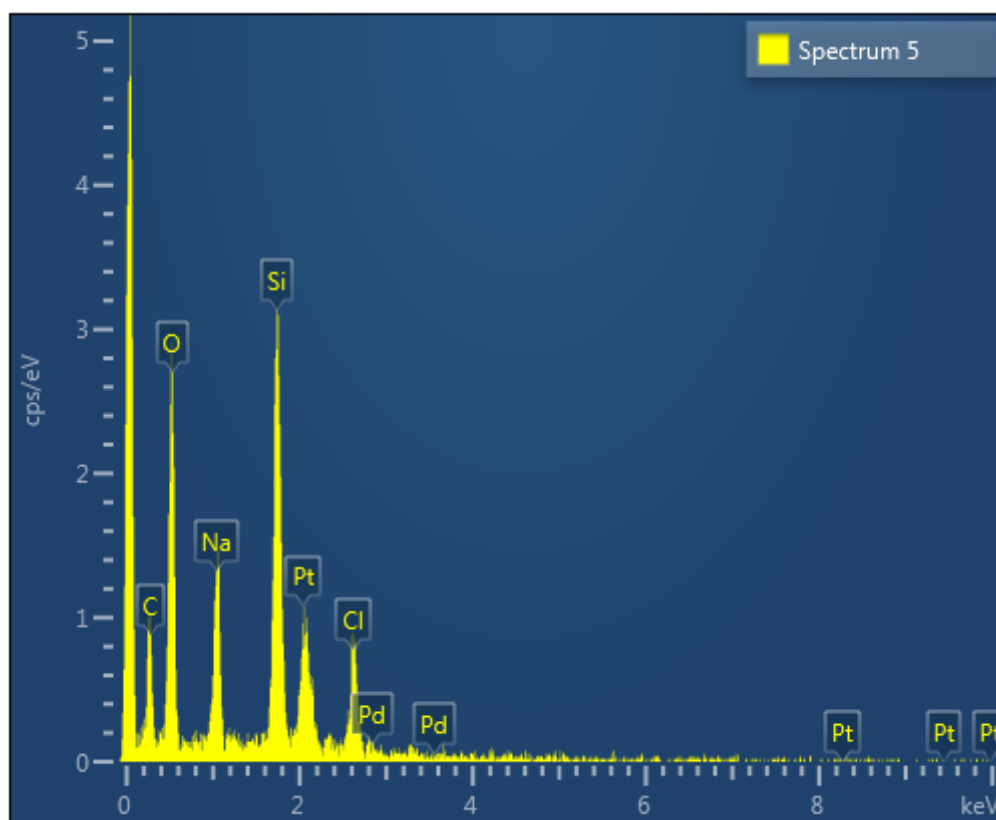
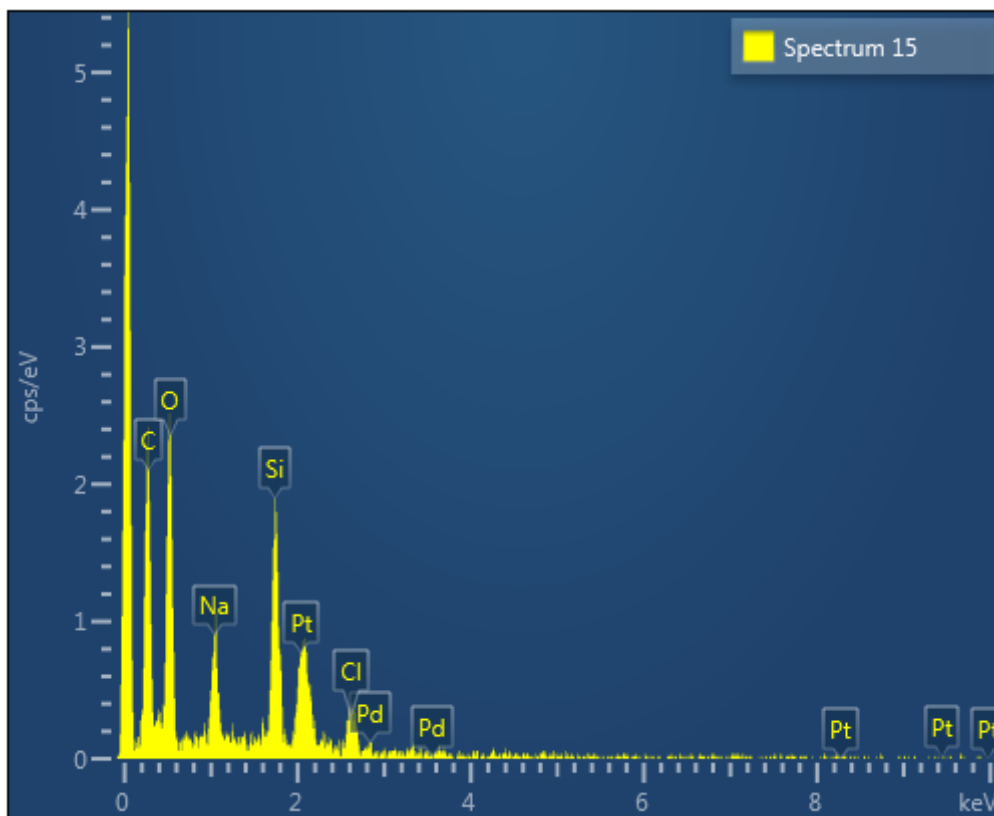


Table S5.3. R5E6-AT Silica EDS result

Element	Line Type	Apparent Concentration	k Ratio	Atomic %	Standard Label	Factory Standard	Standard Calibration Date
C	K series	0.08	0.00081	50.09	C Vit	Yes	
O	K series	0.30	0.00100	28.78	SiO2	Yes	
Na	K series	0.11	0.00045	5.33	Albite	Yes	
Si	K series	0.18	0.00146	11.41	SiO2	Yes	
Cl	K series	0.08	0.00067	4.38	NaCl	Yes	
Total:				100.00			

Figure S5.2. β E6-AT Silica EDS resultTable S5.4. β E6-AT Silica EDS result

Element	Line Type	Apparent Concentration	k Ratio	Wt %	Wt% Sigma	Atomic %	Standard Label	Factory Standard	Standard Calibration Date
C	K series	0.14	0.00136	0.37	0.09	59.84	C Vit	Yes	
O	K series	0.27	0.00090	0.23	0.01	27.62	SiO2	Yes	
Na	K series	0.07	0.00028	0.04	0.00	3.50	Albite	Yes	
Si	K series	0.11	0.00085	0.10	0.01	6.96	SiO2	Yes	
Cl	K series	0.04	0.00031	0.04	0.01	2.08	NaCl	Yes	
Total:				0.77		100.00			

8. Reference

1. Beech, I. B. & Sunner, J. Biocorrosion: towards understanding interactions between biofilms and metals. *Curr. Opin. Biotechnol.* **15**, 181–186 (2004).
2. Flemming, H.-C. & Wingender, J. The biofilm matrix. *Nat. Rev. Microbiol.* **8**, 623–633 (2010).
3. Gambino, M. & Cappitelli, F. Mini-review: Biofilm responses to oxidative stress. *Biofouling* **32**, 167–178 (2016).
4. Flemming, H.-C., Neu, T. R. & Wozniak, D. J. The EPS Matrix: The “House of Biofilm Cells”. *J. Bacteriol.* **189**, 7945–7947 (2007).
5. Flemming, H.-C. *et al.* Biofilms: an emergent form of bacterial life. *Nat. Rev. Microbiol.* **14**, 563–575 (2016).
6. Barnhart, M. M. & Chapman, M. R. Curli Biogenesis and Function. *Annu. Rev. Microbiol.* **60**, 131–147 (2006).
7. Mishra, S. *et al.* Biochemistry, Synthesis, and Applications of Bacterial Cellulose: A Review. *Front. Bioeng. Biotechnol.* **10**, (2022).
8. Zou, L., Zhu, F., Long, Z. & Huang, Y. Bacterial extracellular electron transfer: a powerful route to the green biosynthesis of inorganic nanomaterials for multifunctional applications. *J. Nanobiotechnology* **19**, 120 (2021).
9. Tanaka, K. *et al.* Extracellular Electron Transfer via Outer Membrane Cytochromes in a Methanotrophic Bacterium *Methylococcus capsulatus* (Bath). *Front. Microbiol.* **9**, (2018).
10. Shi, L. *et al.* Extracellular electron transfer mechanisms between microorganisms and minerals. *Nat. Rev. Microbiol.* **14**, 651–662 (2016).

11. Partipilo, G., Graham, A. J., Belardi, B. & Keitz, B. K. Extracellular Electron Transfer Enables Cellular Control of Cu(I)-Catalyzed Alkyne–Azide Cycloaddition. *ACS Cent. Sci.* **8**, 246–257 (2022).
12. Fan, G., Dundas, C. M., Graham, A. J., Lynd, N. A. & Keitz, B. K. *Shewanella oneidensis* as a living electrode for controlled radical polymerization. *Proc. Natl. Acad. Sci.* **115**, 4559–4564 (2018).
13. Edwards, M. J., White, G. F., Butt, J. N., Richardson, D. J. & Clarke, T. A. The Crystal Structure of a Biological Insulated Transmembrane Molecular Wire. *Cell* **181**, 665–673.e10 (2020).
14. Wiatrowski, H. A., Ward, P. M. & Barkay, T. Novel Reduction of Mercury(II) by Mercury-Sensitive Dissimilatory Metal Reducing Bacteria. *Environ. Sci. Technol.* **40**, 6690–6696 (2006).
15. Karbelkar, A. A., Reynolds, E. E., Ahlmark, R. & Furst, A. L. A Microbial Electrochemical Technology to Detect and Degrade Organophosphate Pesticides. *ACS Cent. Sci.* **7**, 1718–1727 (2021).
16. Atkinson, J. T. *et al.* Real-time bioelectronic sensing of environmental contaminants. *Nature* **611**, 548–553 (2022).
17. Hildebrand, M., Lerch, S. J. L. & Shrestha, R. P. Understanding Diatom Cell Wall Silicification—Moving Forward. *Front. Mar. Sci.* **5**, (2018).
18. Mayzel, B., Aram, L., Varsano, N., Wolf, S. G. & Gal, A. Structural evidence for extracellular silica formation by diatoms. *Nat. Commun.* **12**, 4639 (2021).
19. N, K. & N, P. Diatoms—from cell wall biogenesis to nanotechnology. *Annu. Rev. Genet.* **42**, (2008).
20. An, L. *et al.* Nanoengineering Porous Silica for Thermal Management. *ACS Appl. Nano Mater.* **5**, 2655–2663 (2022).

21. Xi, Y., Liangying, Z. & Sasa, W. Pore size and pore-size distribution control of porous silica. *Sens. Actuators B Chem.* **25**, 347–352 (1995).
22. Mesoporous Silica - an overview | ScienceDirect Topics. <https://www.sciencedirect.com/topics/materials-science/mesoporous-silica>.
23. Takeda, E., Xu, W., Terakawa, M. & Niidome, T. Tailored Structure and Antibacterial Properties of Silica-Coated Silver Nanoplates by Pulsed Laser Irradiation. *ACS Omega* **7**, 7251–7256 (2022).
24. Tian, B. & Liu, Y. Antibacterial applications and safety issues of silica-based materials: A review. *Int. J. Appl. Ceram. Technol.* **18**, 289–301 (2021).
25. Han, Y. *et al.* Directed Evolution of Split APEX2 Peroxidase. *ACS Chem. Biol.* **14**, 619–635 (2019).
26. Sharp, K. H., Mewies, M., Moody, P. C. E. & Raven, E. L. Crystal structure of the ascorbate peroxidase–ascorbate complex. *Nat. Struct. Mol. Biol.* **10**, 303–307 (2003).
27. Martell, J. D., Deerinck, T. J., Lam, S. S., Ellisman, M. H. & Ting, A. Y. Electron microscopy using the genetically encoded APEX2 tag in cultured mammalian cells. *Nat. Protoc.* **12**, 1792–1816 (2017).
28. Hung, V. *et al.* Spatially resolved proteomic mapping in living cells with the engineered peroxidase APEX2. *Nat. Protoc.* **11**, 456–475 (2016).
29. Fazal, F. M. *et al.* Atlas of Subcellular RNA Localization Revealed by APEX-Seq. *Cell* **178**, 473–490.e26 (2019).
30. Liu, J. *et al.* Genetically targeted chemical assembly of functional materials in living cells, tissues, and animals. *Science* **367**, 1372–1376 (2020).

31. Hui, Y., Cui, Z. & Sim, S. Stress-Tolerant, Recyclable, and Renewable Biocatalyst Platform Enabled by Engineered Bacterial Spores. *ACS Synth. Biol.* **11**, 2857–2868 (2022).
32. Khademian, M. & Imlay, J. A. Escherichia coli cytochrome c peroxidase is a respiratory oxidase that enables the use of hydrogen peroxide as a terminal electron acceptor. *Proc. Natl. Acad. Sci. U. S. A.* **114**, E6922–E6931 (2017).
33. Lechner, C. C. & Becker, C. F. W. A sequence-function analysis of the silica precipitating silaffin R5 peptide. *J. Pept. Sci. Off. Publ. Eur. Pept. Soc.* **20**, 152–158 (2014).
34. Li, K. *et al.* Diatom-inspired multiscale mineralization of patterned protein–polysaccharide complex structures. *Natl. Sci. Rev.* **8**, nwaa191 (2020).
35. Roeters, S. J. *et al.* Backbone Structure of Diatom Silaffin Peptide R5 in Biosilica Determined by Combining Solid-State NMR with Theoretical Sum-Frequency Generation Spectra. *J. Phys. Chem. Lett.* **12**, 9657–9661 (2021).
36. Lutz, H. *et al.* The Structure of the Diatom Silaffin Peptide R5 within Freestanding Two-Dimensional Biosilica Sheets. *Angew. Chem. Int. Ed Engl.* **56**, 8277–8280 (2017).
37. Baio, J. E. *et al.* Diatom Mimics: Directing the Formation of Biosilica Nanoparticles by Controlled Folding of Lysine-Leucine Peptides. *J. Am. Chem. Soc.* **136**, 15134–15137 (2014).
38. Kozlowski, M. T., Silverman, B. R., Johnstone, C. P. & Tirrell, D. A. Genetically Programmable Microbial Assembly. *ACS Synth. Biol.* **10**, 1351–1359 (2021).
39. Site-Directed Mutagenesis | NEB. <https://www.neb.com/applications/cloning-and-synthetic-biology/site-directed-mutagenesis->

landing?gclid=Cj0KCQjwrfymBhCTARIsADXTabnrBObyZZ6k2NPKg54wmm
0qy3YCFe2H1y6lA4bTVo-C6JhhRRgwwTlaAjfVEALw_wcB.

Chapter 6

Future Directions

1. Abstract

In this chapter we propose future directions for protein-mediated bacterial assembly-based engineered living materials. Following the work reported in Chapters 2 and 3, we propose to improve the mechanical properties of living bacterial films by two means: i). introducing multiple cysteine sites into surface-displayed proteins to achieve non-yielding films or ii). growing E6 and CE6 cells together to form double-network films with greater toughness and stretchability. Inspired by the work reported in Chapter 4, we propose to optimize mineralization and associated mechanical properties by controlling the nature of the surface-displayed protein, the phosphatase expression level, the substrate concentration, and the reaction time. One important result not presented in the previous chapters of this thesis is the surface hydrophobicity of SpyTag-displaying bacterial films. This result suggests that we can control the surface properties of bacterial films through engineering surface-displayed proteins that behave as artificial hydrophobins.

2. Future Directions

6.1. *Improving mechanical properties of bacterial films*

In Chapter 3, we demonstrated that putting a single cysteine at the N-terminus of a displayed elastin-like protein changed the mechanical properties of the living bacterial film drastically, with Young's modulus increased three-fold and a transition from soft, yielding films into stiff, non-yielding materials. However, both E6 and CE6 films are difficult to handle as cm-scale samples to be tested for mechanical strength. E6 films yield at about 1.1 times their original length and deform plastically, making it hard to peel cm-scale pieces of films off their polycarbonate filters. In contrast, CE6 films exhibited brittle failure when we tried to peel large pieces off the filter. These problems motivate the design of new protein constructs and culture methods that can generate resilient, tough, stretchable bacterial films. We aim to generate bacterial films that can stretch to at least 2-5 times their original length, return to original length upon unloading and exhibit toughness between 100 and 1000 J/m², which is comparable to tough, stretchable hydrogels¹.

Covalent crosslinks like disulfide bonds can increase the Young's modulus of bacterial films. CE6 films with cell-surface disulfide bonds have Young's moduli around 44.0 ± 5.6 kPa, approximately three times that of E6 films, which is 14 ± 2.1 kPa (**Fig 3.2e**). When the disulfide bonds were reduced by TCEP for 0.5 hr, the Young's moduli decreased drastically to at least 1/3 of the original Young's moduli without reduction. These results imply that the number of covalent crosslinks between the cells determines the elasticity of the bacterial film. In the current CE6 system, two CE6 proteins from two adjacent cells form one disulfide crosslink. If we can increase the number of cysteines per displayed protein, more than one covalent crosslink can be formed and

thus increase the strength of intercellular adhesion. Stronger intercellular adhesion should cause the bacterial film to exhibit larger Young's moduli.

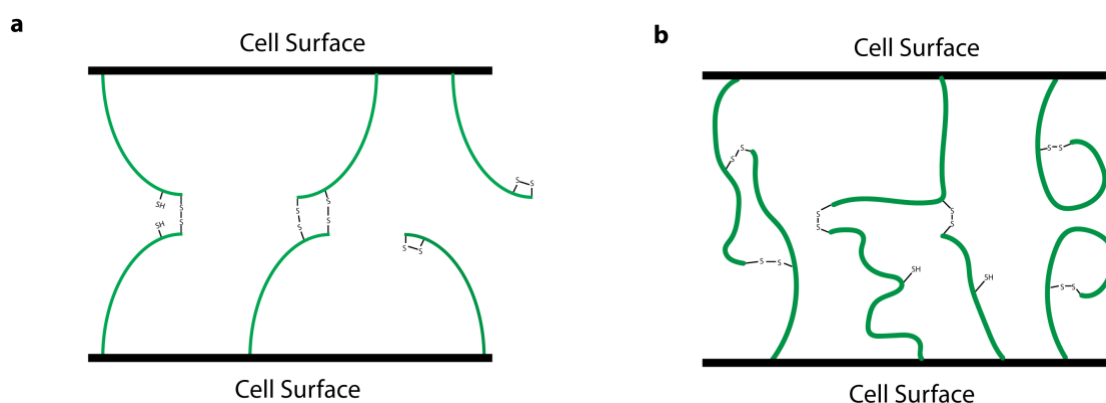


Figure 6.1. Schemes of intercellular adhesion with 2 cysteines per displayed protein. **a**, Schematic of putting 2 cysteines at the N-terminal end of the displayed protein. Possible crosslinking scenarios are shown. **b**, Schematic of putting one cysteine at the N-terminal end of the protein and putting another in the middle of the displayed protein. Possible intercellular crosslinking scenarios are shown.

Two cysteines per displayed protein are shown as an example in **Fig 6.1**. One approach is to put both cysteines at the N-terminus of the displayed protein (**Fig 6.1a**). In this case, when two proteins from adjacent cells react with each other, we can either get one crosslink per two proteins (left image) or two crosslinks per two proteins (middle image). The more double crosslinks formed the stronger the adhesion between cells will be, resulting a stiffer bacterial film. Another approach, inspired by previous work in the Tirrell laboratory using SpyTag-SpyCatcher chemistry to generate protein hydrogels², would put one cysteine at the N-terminus of the displayed protein and the other cysteine in the middle. As shown in **Fig 6.1b**, in the left image, two proteins may react with one another, forming two disulfide bonds. Since the two cysteines are well separated, the N-terminal cysteine can react either with the N-terminal cysteine or the internal cysteine. The flexibility of reaction between different sites of cysteines can potentially result a crosslinked network of multiple proteins between two cells. Taking the middle image in **Fig 6.1b** as an example, the protein on the top cell can react with two proteins from the bottom cell. The exposed cysteines in the middle parts of proteins

in the bottom cell can react with other proteins on the top cell, resulting a network of crosslinked protein. It would be interesting to explore the relationship between the number and location of cysteines in the engineered proteins, and mechanical behavior of bacterial films.

The biggest challenge for the approach of putting more than one cysteines in the displayed peptide is difficulty of cloning. Site-directed PCR mutagenesis is challenging for the surface-display system we are using due to high GC content (> 60%) of the pelB leader peptide and elastin-like peptide sequence. Based on calculations from NEB base changer website, the annealing temperatures of primers for direct site mutagenesis of putting cysteine directly ahead of the elastin-like peptide or directly after the pelB peptide are above 72 °C, which can't be used for PCR amplification. This is the reason why we put the cysteine behind the 6 x His tag (**Table S3.2**) and mutated the pAT-ST (**Table S3.3**) first to contain a cysteine and then pasted in the E6 insert to make the pAT-CE6 construct. To put two cysteines near the N-terminus of the displayed elastin, we would follow the same protocol for making CE6-AT but we would put a series of "GS" spacers^{6,7} of different length between the two cysteine residues. The reason for doing this is to reduce the chance of disulfide formation between two cysteine residues when they are adjacent to each other.

Increasing the density of crosslinks between the cells might have adverse effect on stretchability and toughness of the film. Because there are more covalent crosslinks between the cells, the cells would adhere more tightly to each other. To make bacterial films tough and stretchable, energy dissipation strategies have to be incorporated into the bacterial films.

To solve this problem, it is wise to look into other fields for inspiration. One good example is highly stretchable and tough hydrogel¹. In such hydrogels made of double networks, a covalently crosslinked polyacrylamide network provides network rigidity, while the calcium alginate network can unzip during the stretching process and efficiently dissipate the energy, preventing polyacrylamide network from breaking. When the load is removed, the calcium alginate ionic crosslink can be reformed, and since the polyacrylamide network remains intact during the stretching process, the hydrogel goes back to the original shape, making the hydrogel resilient. Interestingly, polyacrylamide gels and calcium alginate gels themselves are not resilient and highly stretchable. Polyacrylamide gels are non-yielding and brittle³, while calcium alginate gels are soft and rupture when stretched to about 1.2 times their original length^{1,4}. Interestingly, E6 films yield when bulged to about 1.1 times their original lengths and rupture between 1.1 to 1.3 times their original length (**Fig 3.2d**). It is tempting to consider that bacterial films made of mixed CE6 and E6 cells would become tough, resilient and stretchable compared to both CE6 and E6 films alone. In order to grow a film made of both CE6 and E6 cells, E6 and CE6 culture will be mixed before coating onto the polycarbonate filter, with ratio between E6 and CE6 cell numbers controlled by both optical density and volume ratio between two kinds of culture.

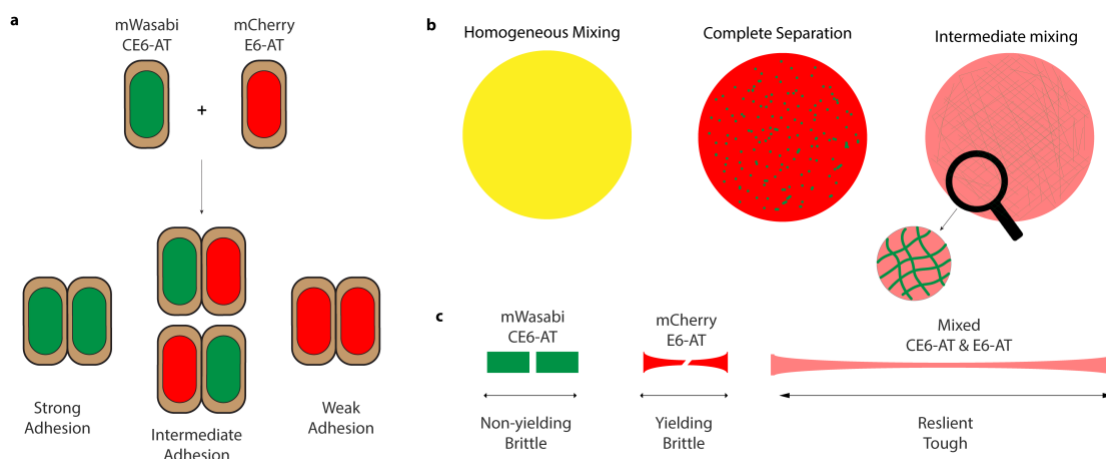


Figure 6.2. Schemes of mixing E6 and CE6 displaying cells to generate tough and resilient bacterial films. a, Schematic of different types of adhesion between mWasabi CE6-AT cells and mCherry E6-AT cells. **b,** Schematics of bacterial films' morphology when of CE6 and E6 expressing cells are mixed together. Left, homogeneous mixing of CE6 and E6 cells. Middle, complete separation between CE6 and E6 cells. Right, E6 and CE6 cells mixed in a way that CE6 cells from network and E6 cells forms matrix entrapping CE6 network. **c,** Schematics of stretching tests for CE6 films, E6 films and mixed films.

As shown in **Fig 6.2a**, when E6 and CE6 displaying cells are mixed together, 3 kinds of interactions are possible: strong covalent adhesion between CE6 cells, weak adhesion between E6 cells, and interactions between E6 and CE6 cells. We color coded CE6 cells green, representing mWasabi expression, and E6 cells red, representing mCherry expression. For E6 and CE6 protein interaction, since there is no cysteine in the E6 protein to form disulfide bonds, the strength of E6-CE6 protein interaction should be similar to that of E6-E6 protein. However, there might be some other proteins with exposed cysteine residues⁵ on the cell surface, which can react with cysteines in CE6 proteins and forming intercellular covalent crosslinks. Regarding this possibility, the interaction strength between CE6 and E6 cells should be much smaller than that between CE6 cells but a bit larger than that between E6 cells. In an ideal situation (**Fig 6.2b** left panel), the red-colored E6 and green-colored CE6 cells grow at the same rate and mix homogeneously causing the film to look yellow. When E6 and CE6 cells were mixed homogeneously, E6-CE6 protein interaction would be the most abundant type of intercellular interactions, making the mixed film's mechanical properties more

similar to that of E6 film instead of CE6 film. Such scenario is not likely to happen because cells of same kind are still adjacent to each other after each division. There will always be a CE6 cell adjacent to another CE6 cell. Another situation we would like to avoid is shown in the middle panel of **Fig 6.2b**, in which complete phase separation between CE6 and E6 cells happens, similar to what happened between SpyTag-E6 and SpyCatcher displaying cells as shown in **Fig 2.5**. In the case of the SpyTag-SpyCatcher system, SpyTag displaying cells are self-associative while SpyCatcher cells are not, resulting in SpyTag displaying cells forming disconnected “islands” in the “sea” of SpyCatcher displaying cells. In the case of E6 and CE6, since covalent interactions between CE6 cells are stronger than E6-CE6 interactions and E6-E6 interaction, it’s likely that CE6 cells might form clumps or islands in the film. However, compared to SpyCatcher, E6 is self-associative and can also adhere to CE6 cells through interactions between unstructured elastin domains, making complete spatial separation between CE6 and E6 cells unlikely. To form a bacterial film with mechanical properties like those of a stretchable and tough hydrogel, we propose that CE6 should form an interconnected covalent network and E6 cells should be well-dispersed in the film and wrapping the CE6 cells as shown in the enlarged region of the right panel of **Fig 6.2b**. We suggest that when such mixed films are stretched, the E6 cells will dissipate energy by sliding past one another and the CE6 cells’ covalent network will maintain the shape of the film, allowing the bacterial film to stretch upon loading and maintain its shape when the stretching force is removed (**Fig 6.2c**, right panel). In this cell-mixing approach, the major challenge is to have bacterial films growing into few hundred micrometers of thickness that films can be clamped and loaded onto a material testing machine for tensile strength and stretchability measurements.

6.2. Finding the “sweet-spot” for bacterial mineralization

In chapter 4, we discussed using stimulated Raman scattering microscopy in characterizing mineralization of living bacterial films *in situ*. Though we achieved quantification of the ratio between organic and inorganic species without destructive or intrusive treatment during mineralization, we were not able to determine the optimal degree of mineralization that makes mineralized bacterial films both stiff and tough. After 2 hours of mineralization as shown in **Fig 4.5**, all three kinds of films (PhoA, E6/PhoA and Triblock/PhoA) had Young’s moduli over 1 MPa, with E6/PhoA reaching more than 10 MPa, which is 1000 times larger than the non-mineralized E6/PhoA films. However, all these mineralized films were too brittle to be handled and break easily once transferred to the bulge test device. When looking into earlier time points, for example 20 minutes and 30 minutes, we found that Triblock/E6 films can endure strain up to between 0.25 and 0.30 (**Fig S4.10**), which is even larger than the strains borne by the non-mineralized E6/PhoA film (maximum strain 0.15). These results suggest that there might be a “sweet-spot” for mineralization where mineralized films would have both enhanced stiffness and toughness.

To find this ideal degree of mineralization, we need to control multiple factors. For example, although we induced all the films with the same concentration of inducer, temperature and time, variability in phosphatase expression from one film to another is inevitable. This limitation requires us to quantify the expression level of the phosphatase. One way to do this is to lyse the film and measure the expression level by Western blot, which is destructive. Since the Raman microscope we are using is also capable of doing fluorescence imaging, we can put a fluorescent protein gene downstream of the phosphatase gene under the same inducible promoter, such that

fluorescence intensity measured by the microscope can be used as an indicator of phosphatase expression level. Using this method, we can quantify both phosphatase expression level and degree of mineralization non-destructively. We would also like to slow down the rate of mineralization so that we characterize more samples with different degrees of mineralization. To achieve this goal, we can either lower the concentration of organic phosphate or reduce the inducer concentration and induction time. We can also reduce the promoter strength to lower the expression level of the phosphatase and eventually slow down the mineralization process.

In Chapter 4, the PhoA enzyme was tethered to a PelB leader peptide and expressed in the periplasm such that the conversion of organic phosphate to inorganic phosphate would occur in the periplasmic space of *E. coli*. It would be interesting to explore if the location of phosphatase expression would have an effect on mineralization morphology of calcium phosphate, mechanical properties of mineralized films, mineralization kinetics and cell viability. Currently, we have constructs of PhoA that are expressed in the cytosol and in the periplasm. PhoA fused to the autotransporter protein was shown to be highly cytotoxic and could not be displayed on the cell surface. This problem requires us to identify pairs of phosphatases and surface-display proteins that can result in efficient display of phosphatases at the cell surface.

6.3. Developing artificial hydrophobin

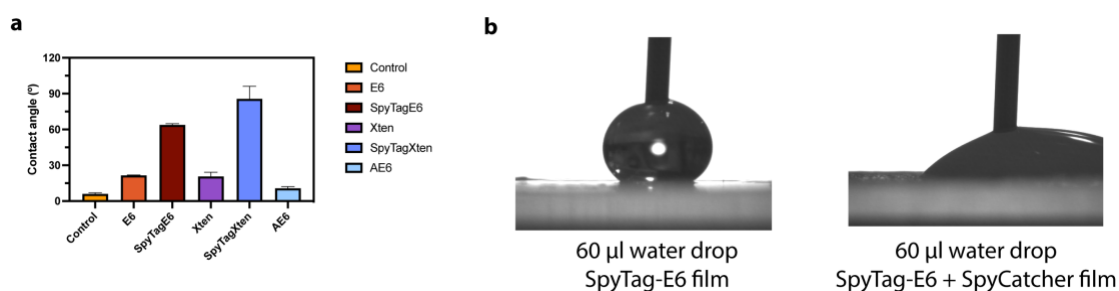


Figure 6.3. Contact angle data of water droplets on direct bacterial films' surface. **A**, Contact angle data of 5 µl water droplets on different bacterial films' surface. Number of replicates equals 3. **B**, Image of a 60 µl water droplet on SpyTag-E6 expressing film (left image) and a 60 µl water droplet on SpyTag-E6 and SpyCatcher expressing film (right image).

In nature, some bacteria, for example, *Bacillus subtilis*, can form biofilms with hydrophobic surfaces by secreting the hydrophobin BslA.^{8,9} These hydrophobic biofilms are more resistant to antibiotics and can withstand dehydration.¹⁰ BslA has been studied extensively in the past decade as a model hydrophobin¹¹ and can potentially be used as a stabilizer in food industry.¹²

Interestingly, I noticed that when PBS buffers were dropped onto bacterial films expressing SpyTag-E6 proteins, the buffer droplets remained spherical on the surface of the bacterial film rather than spreading out as observed on other types of bacterial films. This made me wonder if SpyTag expression increased the hydrophobicity of the bacterial film surface. To test my hypothesis, I used a goniometer to measure the static contact angles of 5 µl volume water droplets on bacterial films with different cell surface displayed proteins. Static contact angle is the most popular method to analyze a surface's wettability, with contact angle between 0° and 90° as hydrophilic and greater than 90° as hydrophobic¹³. As shown in **Fig 6.3a**, the control films without surface protein expression had contact angles smaller than 5° on average, meaning the water immediately spreads out on the surface and the bacterial film surface is hydrophilic. SpyTagE6 expressing films, however, had average contact angle greater than 60°,

suggesting the surface is more hydrophobic compared to the control. To rule out the possibility that elastin-like-peptide (ELP) linkers are playing the major role in increasing surface hydrophobicity, contact angles on E6 expressing films were measured to be around 25°, much smaller than that of SpyTagE6. To make sure that increased hydrophobicity of bacterial surface is not a coincidence, we tethered SpyTag to another unstructured protein linker Xten,¹⁴ and the contact angle measurement showed similar pattern, in which SpyTagXten expressing films had average contact angle close to 90° and Xten-only films had average contact angle of around 25°. We also measured contact angle of AE6 (see chapter 2, section 2.3), an alpha-helical coiled-coil peptide tethered to E6 linker, only to find contact angle to be even smaller than that of E6 films. These results suggest that SpyTag plays a crucial role in increasing the hydrophobicity of bacterial film's surface, but the fundamental molecular mechanism of such reduced wettability of the surface is not well understood. One hypothesis is that SpyTag, a beta-sheet peptide¹⁵, can form a hydrophobic peptide surface.¹⁶ Evidence for this hypothesis is provided by Congo Red staining on SpyTagE6 films, which indicates beta sheet amyloid formation.¹⁷ However, more detailed investigations are needed to prove this hypothesis. Once the mechanism is well understood, routes to design artificial hydrophobin might be possible.

We also explored if surface wettability can be changed upon environmental stimuli using SpyTagE6-SpyCatcher double plasmids system described in chapter 2. In the left image of **Fig 6.3b**, an advancing contact angle experiment was performed on a SpyTagE6 expressing film. The rate of water addition is 1 μ l/s and after 1 minute, a 60 μ l water droplet can stand on the surface with contact angle greater than 90°, showing the surface is relative hydrophobic and not easily wettable. We then transferred the

film on an LB agar plate containing 0.1 % l-arabinose for one day to induce the expression of SpyCatcher at the surface. The advancing contact angle experiment was repeated on the induced film and the contact angle was shown to be smaller than 45° as shown in the right image of **Fig 6.3b**, indicating reduced hydrophobicity of the bacterial film surface, likely caused by reduced SpyTag concentration at the surface due to reaction with SpyCatcher. This is a demonstration of controlling surface wettability of bacterial films through environmental stimuli.

3. References

1. Sun, J.-Y. *et al.* Highly stretchable and tough hydrogels. *Nature* **489**, 133–136 (2012).
2. Sun, F., Zhang, W.-B., Mahdavi, A., Arnold, F. H. & Tirrell, D. A. Synthesis of bioactive protein hydrogels by genetically encoded SpyTag-SpyCatcher chemistry. *Proc. Natl. Acad. Sci.* **111**, 11269–11274 (2014).
3. Hassan, S., Kim, J. & suo, Z. Polyacrylamide hydrogels. IV. Near-perfect elasticity and rate-dependent toughness. *J. Mech. Phys. Solids* **158**, 104675 (2022).
4. Qiao, Z., Parks, J., Choi, P. & Ji, H.-F. Applications of Highly Stretchable and Tough Hydrogels. *Polymers* **11**, 1773 (2019).
5. Ohtsu, I. *et al.* The l-Cysteine/l-Cystine Shuttle System Provides Reducing Equivalents to the Periplasm in Escherichia coli. *J. Biol. Chem.* **285**, 17479–17487 (2010).
6. Chen, X., Zaro, J. & Shen, W.-C. Fusion Protein Linkers: Property, Design and Functionality. *Adv. Drug Deliv. Rev.* **65**, 1357–1369 (2013).
7. Argos, P. An investigation of oligopeptides linking domains in protein tertiary structures and possible candidates for general gene fusion. *J. Mol. Biol.* **211**, 943–958 (1990).
8. Hogley, L. *et al.* BslA is a self-assembling bacterial hydrophobin that coats the Bacillus subtilis biofilm. *Proc. Natl. Acad. Sci. U. S. A.* **110**, 13600–13605 (2013).
9. Morris, R. J. *et al.* Natural variations in the biofilm-associated protein BslA from the genus Bacillus. *Sci. Rep.* **7**, 6730 (2017).
10. Kalamara, M., Abbott, J. C., MacPhee, C. E. & Stanley-Wall, N. R. Biofilm hydrophobicity in environmental isolates of Bacillus subtilis. *Microbiol. Read. Engl.* **167**, (2021).

11. Liu, W., Li, S., Wang, Z., Yan, E. C. Y. & Leblanc, R. M. Characterization of Surface-Active Biofilm Protein BslA in Self-Assembling Langmuir Monolayer at the Air–Water Interface. *Langmuir* **33**, 7548–7555 (2017).
12. Feltman, R. This protein may be the key to slow-melting ice cream. *Washington Post* (2021).
13. Löblein, S. M., Merz, R., Müller, D. W., Kopnarski, M. & Mücklich, F. An in-depth evaluation of sample and measurement induced influences on static contact angle measurements. *Sci. Rep.* **12**, 19389 (2022).
14. Haeckel, A., Appler, F., Ariza de Schellenberger, A. & Schellenberger, E. XTEN as Biological Alternative to PEGylation Allows Complete Expression of a Protease-Activatable Killin-Based Cytostatic. *PLoS ONE* **11**, e0157193 (2016).
15. Li, L., Fierer, J. O., Rapoport, T. A. & Howarth, M. Structural Analysis and Optimization of the Covalent Association between SpyCatcher and a Peptide Tag. *J. Mol. Biol.* **426**, 309–317 (2014).
16. Elsayy, M. A. *et al.* Modification of β -Sheet Forming Peptide Hydrophobic Face: Effect on Self-Assembly and Gelation. *Langmuir* **32**, 4917–4923 (2016).
17. Yakupova, E. I., Bobyleva, L. G., Vikhlyantsev, I. M. & Bobylev, A. G. Congo Red and amyloids: history and relationship. *Biosci. Rep.* **39**, BSR20181415 (2019).